Development of TMD-based Solid Lubrication Coatings using Magnetron Sputtering for Aerospace Applications

M.Tech. Thesis

by
ADITYA DATTU GIRGE

**DEPARTMENT OF METALLURGICAL ENGINEERING AND MATERIALS SCIENCE (MEMS)
INDIAN INSTITUTE OF TECHNOLOGY INDORE
MAY 2025**

Development of TMD-based Solid Lubrication Coatings using Magnetron Sputtering for Aerospace Applications

A THESIS

Submitted in partial fulfilment of the requirements for the award of the degree
of
Master of Technology

by
ADITYA DATTU GIRGE

**DEPARTMENT OF METALLURGICAL ENGINEERING AND MATERIALS SCIENCE (MEMS)
INDIAN INSTITUTE OF TECHNOLOGY INDORE
MAY 2025**

INDIAN INSTITUTE OF TECHNOLOGY INDORE

CANDIDATE'S DECLARATION

I hereby certify that the work which is being presented in the thesis entitled **Development of TMD - based Solid Lubrication Coatings using indigenous methods for Aerospace Applications** in the partial fulfillment of the requirements for the award of the degree of **MASTER OF TECHNOLOGY** and submitted in the **DEPARTMENT OF METALLURGICAL ENGINEERING AND MATERIALS SCIENCE (MEMS), Indian Institute of Technology Indore**, is an authentic record of my work carried out during the period from August 2023 to May 2025 under the supervision of Dr. K. Eswara Prasad, Associate Professor, MEMS, Indian Institute of Technology Indore and mentorship of Shri. Ch. V. Satyanarayana Raju, Scientist F, Research Centre Imarat (RCI), DRDO, Hyderabad.

I have not submitted the matter presented in this thesis for the award of any other degree of this or any other institute.

Signature of the student with date
ADITYA DATTU GIRGE

This is to certify that the above statement made by the candidate is correct to the best of my knowledge.

Signature of the Supervisor of
M.Tech. Thesis (with date)
Dr. K. Eswara Prasad

ADITYA DATTU GIRGE has successfully given his M.Tech. Oral Examination held on **26th May 2025**.

Signature of the Supervisor of M.Tech. Thesis
Date: 28/05/2025

Acting
Convener, DPGC
Date: 27/05/2025

ACKNOWLEDGEMENTS

To

Rev. Daaji,

whose divine grace and inner guidance

through Heartfulness meditation

inspired every step of this journey.

Abstract

This thesis presents the development and comprehensive characterisation of molybdenum disulfide-titanium (MoS_2-Ti) multilayer solid lubricant coatings deposited via PVD - magnetron sputtering, specifically engineered for precision components in missile guidance actuators. Addressing the critical need for reliable solid lubrication in extreme operational environments, the research systematically optimised deposition parameters (argon pressure: 4 bar, flow rate: 10 sccm, substrate-to-target distance: 45 mm) and implemented a custom substrate rotation mechanism to resolve coating non-uniformity. The optimised process yielded near-stoichiometric MoS_2 coatings ($N_s/N_{mo} = 1.72$) with Ti interlayers, achieving controlled thickness (8–13 μm) and columnar microstructures consistent with literature.

Tribological evaluation via pin-on-disc testing demonstrated a 25% reduction in friction coefficient (CoF $\leq$ 0.02) compared to uncoated 17- 4PH steel, with a 45% improvement during the critical initial 60 seconds of operation, aligning precisely with missile actuator duty cycles. Structural characterisation using XRD and Raman spectroscopy revealed that Ti incorporation promotes amorphous phase formation, enhancing environmental stability while retaining MoS_2's solid lubrication properties. Wear debris analysis identified self-lubricating transfer layers of compacted MoS_2 particles, explaining periodic friction fluctuations during testing.

The study bridges laboratory-scale optimisation to real-world application, validating the coating's suitability for missile guidance systems. Future work directions include nanoscale microstructure analysis via TEM, humidity resistance studies, and performance validation on actual actuator components. This research establishes a robust framework for deploying advanced solid lubricants in defence applications, offering a viable alternative to conventional lubricants under extreme mechanical and environmental stresses.

TABLE OF CONTENTS

LIST OF FIGURES

LIST OF TABLES

Chapter 1

Introduction

Solid lubrication represents a critical technology for extreme operating environments where conventional liquid lubricants fail to perform effectively. Solid lubricants can be defined as materials that provide lubrication under essentially dry conditions to two surfaces moving relative to each other. Graphite, polytetrafluoroethylene (PTFE), tungsten disulfide (WS_2), and molybdenum disulfide (MoS_2) are the most widely used solid lubricants. These materials create a low shear strength interfacial film between contacting surfaces, reducing friction and wear while maintaining structural integrity under load. Unlike liquid lubricants that form hydrodynamic films, solid lubricants work through direct surface interactions, making them uniquely suited for challenging operating conditions. Traditional grease-based lubricants like Molykote 33 degrade rapidly under these conditions, with operational lifespans limited to 1-2 years compared to the required 10-15-year service life of defence systems. The vacuum environment of high-altitude operation further compromises liquid lubricants through rapid evaporation and phase instability.

In missile systems, lubrication requirements present extraordinary challenges due to the extreme operating environments. Missiles experience high-speed operation, extreme temperature fluctuations (from cryogenic to several hundred degrees Celsius), high contact pressures, vacuum conditions, and radiation exposure. Conventional liquid lubricants decompose or evaporate under these conditions, leading to system failure. Solid lubricants are therefore essential in missile applications, including guidance systems, control surfaces, bearings, gears, fasteners in high-temperature environments, and hydraulic motors. The performance and lifespan of missile mechanical systems are significantly increased by lowering friction and wear, which are the primary causes of mechanical failure, through efficient solid lubrication.

Transition Metal Dichalcogenides (TMDs), particularly WS_2 and MoS_2, have emerged as premier solid lubricants for high-performance applications like missile systems. These materials achieve low friction and wear in sliding contacts and low torque in rolling contacts. These are intrinsic solid lubricants

whose crystal structure promotes interfacial sliding and shear. MoS_2 provides acceptable lubrication up to approximately 1000°C in vacuum environments, making it ideal for missile applications. The effectiveness of these materials stems from their laminar structure, where simple shearing is made possible by weak van der Waals interactions between layers. In contrast, strong covalent bonds within layers resist wear and asperity penetration. Their thermal stability in vacuum or inert environments makes TMDs particularly valuable for missile systems operating in space or at extreme altitudes.

The benefits of solid lubricants for missile applications extend beyond mere performance enhancements to fundamental design advantages. From an engineering perspective, solid lubrication eliminates complex oil circulation systems, reducing component weight by 30-40% in rotary mechanisms – a critical advantage for flight dynamics. They offer enhanced mechanical stability, enabling the positioning of bearings nearer heat sources and relieving problems with shaft critical speed. Furthermore, solid lubricants can be used where an accumulation of dust or dirt cannot be tolerated and are often not impact-sensitive in liquid oxygen environments, making them ideal for missile propulsion systems. For mission-critical applications like missiles, where repair is impossible after deployment, solid lubricants provide reliable operation throughout the entire mission lifetime, preventing catastrophic failures that could otherwise jeopardise multi-million-dollar systems.

1.1 Layered TMDs:

A wide variety of chemical compounds created by the bonding of transition metals like molybdenum, tungsten, and niobium with chalcogenides like sulfur, selenium, and tellurium comprise a class of materials with exceptional and unusual properties based on the extreme degree of anisotropy in their layered crystal structure. They are some of the most widely utilised solid lubricants in space applications [1] It is like an ice cream sandwich: the molybdenum (Mo) layer is the ice cream centre, and the sulfur (S) layers are the soft cookie shells holding it together. MoS_2 can be exfoliated into atomically thin sheets, like a sandwich can be peeled into layers. In MoS_2, each layer consists of a sheet of molybdenum atoms "sandwiched" between two sheets of sulfur atoms, just as the filling of a sandwich is held between two slices of bread. LTMDs are formed by

stacking "sandwiches" consisting of a transition metal layer between two chalcogen layers. There is strong covalent bonding within the sandwiches but weak (van der Waals') bonding between them.
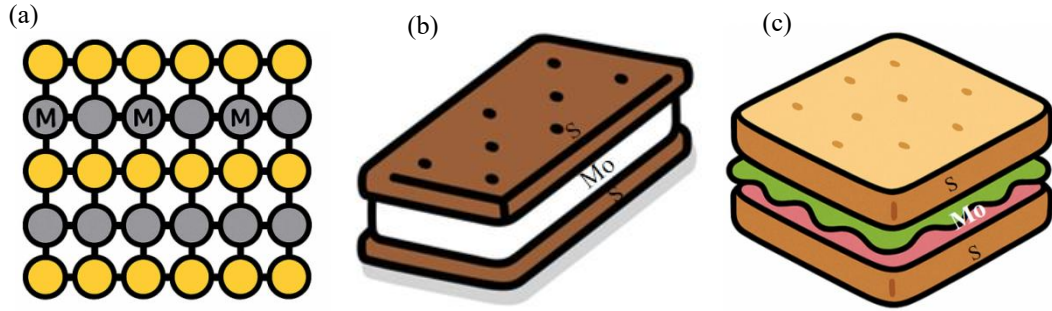
Figure 1.1: Analogy of the layered structure of transition metal dichalcogenide (MoS_2) with real-life sandwiches. (a) Atomic structure of MoS_2 showing molybdenum (Mo) atoms sandwiched between sulfur (S) layers. (b) An ice cream sandwich represents the Mo layer (ice cream) between two S layers (chocolate wafers). (c) In the traditional sandwich model, Mo (veggies) is enclosed between S layers (bread), emphasising the 2D layered architecture.

Their structure is planar or hexagonal stacked, with atoms in the layers or planes having a strong connection with one another. On the other hand, weaker Vander Wall forces indicate the connection between the various layers or planes. Shearing along the basal planes is easy and isotropic due to the mild interlayer forces. [2]. This group includes well-known materials such as graphene, graphite, TMDs, hexagonal boron nitride (hBN), and especially MoS_2 and WS_2.
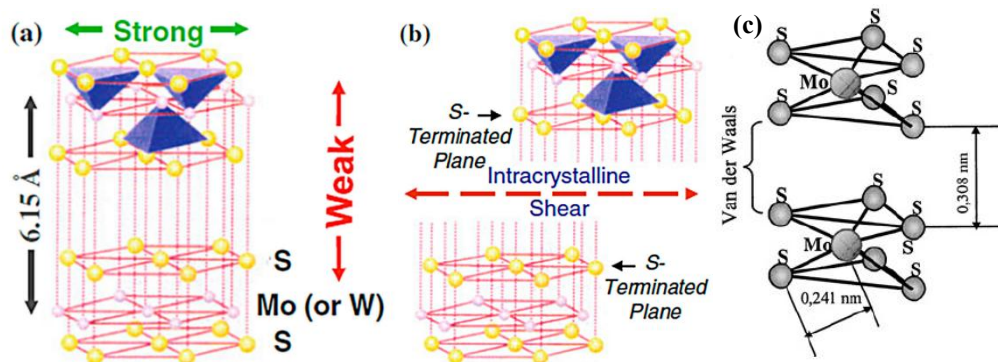
Figure 1.2: (a) Lamellar crystal structure of Mo (or W) disulfide. (b) The weak van der Waals forces give rise to interlamellar mechanical weakness and hence easy shear (slip) between the planes [3]. c) Layered structure of MoS_2 [4].

In contrast to the weak van der Waals adhesion forces between sulfur-like atoms, which result in the formation of easy-to-shear lamellas, some TMDs, such as Mo- and W-disulfides and diselenides, have a closely packed lamellar structure with strong bonding between the metal and chalcogenide ligands. This

microstructure is the primary lubrication mechanism for this class of solid lubricants (see Figure 1.2). Additionally, TMDs can align in sliding direction, which reduces friction throughout the entire tribosystem [3] and functions as a solid lubricant. However, the ability of the lamellas to slide against one another can be significantly impacted by the adsorption of chemical compounds from the environment, such as H_2O. As seen for similarly layered TMDs like NbS_2 or TiS_2, it is also important to note that a layered microstructure alone is insufficient to achieve self-lubrication; instead, the strength of the interlayer bonding plays a crucial role [5] . Because of its advantageous tribological characteristics and cheaper price compared to other TMDs like WS_2, MoS_2 is by far the most popular TMD. It has been a solid lubricant since the 1940s [6], [7] and is well suited for space applications. It is also highly effective in dry air and a vacuum.

1.2 MoS$_2$

The bonding of MoS_2, which describes the crystal structure, must be considered to understand the lubricating mechanism better. Molybdenum, a metal with a strong polarising effect, joins with sulfur, a non-metal readily polarised, to form MoS_2 through a covalent link. The molybdenum disulfide compound's metallic lustre and black colour suggest the presence of a strong covalent bond, in contrast to ionic compounds, where the ion radius ratio determines the maximal coordination number; such elements in a compound no longer aim for this. Unlike cadmium iodide, which has a preponderance of covalent bonds and a significant degree of ionic bonding, molybdenum is surrounded by six sulfur atoms in the form of a triangular prism rather than an octahedron. Unlike ionic bonding, which necessitates a maximum distance between equal atoms and excellent charge screening (protection), MoS is based on covalent bonding. Just 3.15 A is the smallest Mo-Mo distance. A big atom's electron cloud is deformed by polarisation when an electropositive neighbour pulls a piece of the cloud toward the metal. [8]

Molybdenum disulfide crystallises in a layer lattice where the MoS2 layers are placed one above the other due to electrostatic balancing as the sulfur atoms are polarised to dipoles (Fig. 1.3). A very weak bonding force between the layers is indicated by the very long S-S distance of 3.49 A between two layers, which the significant deformation of the sulfur atoms can partially explain. Because each

4

sulfur atom in the crystal structure has three Mo neighbours, it receives three mass centres of electropositive charges in direct opposition to the MO atoms. Where Mo atoms draw in portions of the sulfur atoms' electron clouds, there are electronegative charges. A molybdenum disulfide layer's surface is therefore made up of a distribution of weak positive and negative charges (Fig. 1.3). As a result, the sulfur atoms of one molybdenum disulfide layer fit straight into the other layer, where the concentration of electronegative charges is present, due to the arrangement of the single crystal MoS_2 layers. Weak attraction forces are produced between the layers as a result. [9].
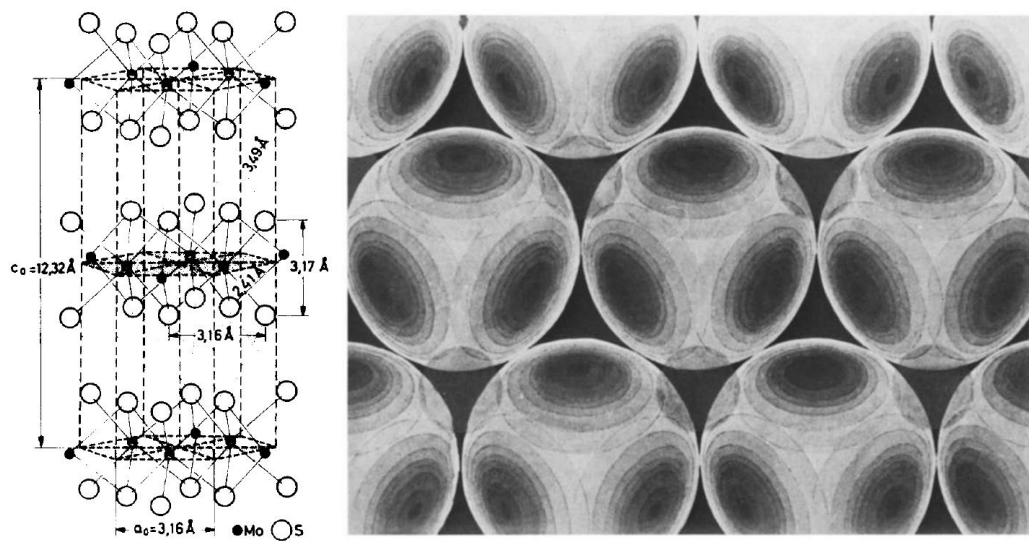
Figure 1.3: Crystal structure of MoS_2 (Left); Basal layer of MoS, consisting of sulfur atoms with their three electric charge centres originating from the polarisation of the Mo-atoms underneath the layer (Right) [8]

It can be inferred that MoS_2's strong covalent bonding, which causes the sulfur atoms to become strongly polarised, gives it its good lubricating qualities, rather than the layer structure. The significant polarisation leads to the layer structure. It should be mentioned that good lubricating attributes are not always associated with a layer structure. Similar to MoS_2, clays and micas show a noticeable anisotropy of cleavage but lack lubricating qualities. Because of the two atoms' high polarisation, molybdenum disulfide has a unique place among layer lattice materials [8].

In summary, this significant polarisation results in the qualities mentioned, which explain the outstanding film-forming properties, the orientation of MoS_2 crystals, and the good metal adhesion.

Two factors are responsible for MoS_2 coatings' good lubricating qualities. These are the film's crystallographic orientation and adherence to the substrate. Depending on the deposition settings, MoS_2 films formed by sputtering are known to exhibit two forms of orientation, designated as Type I and Type II. As seen in Fig. 1.4, Type I's basal plane orientation permits ambient components to penetrate perpendicular to the substrate surface. In Type II, the basal plane is immune to environmental threats and runs parallel to the substrate. The basal plane of MoS_2 needs to be parallel to the substrate surface to have the best friction properties. It is suggested that the strength of the chemical interaction between the MoS_2 edge-plane [e.g., (100)] atoms and the substrate atoms causes a zone of crystallites at the film-substrate interface to fail to properly orient continually. Additionally, a Ṅzone of failure during use is shown by the plane that represents the interface between crystallites of different orientations. [10].
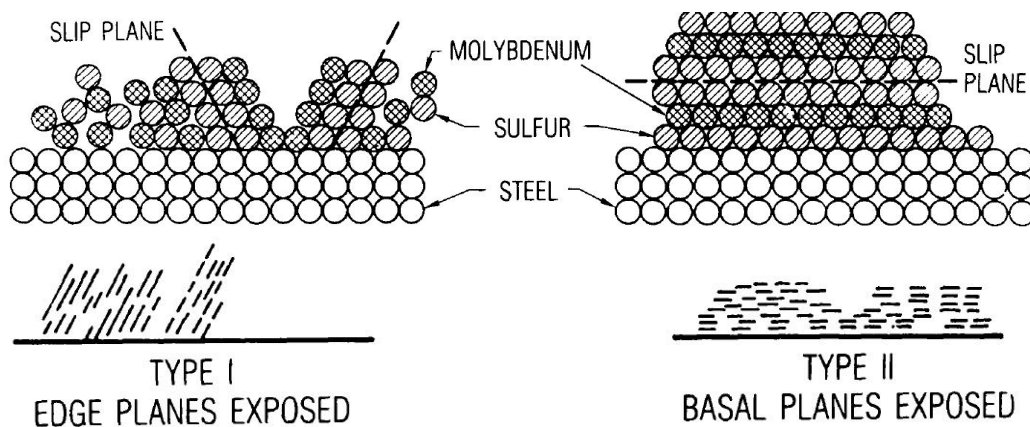
Figure 1.4: Schematic drawings of type I and II sputter-deposited MoS_2 films[11]

Most available publications describe bulk materials sintered by powder metallurgy and thin films deposited by PVD. At the same time, a much smaller number of references deal with thicker hardfacings prepared either by laser cladding or thermal spray techniques. Figure 1.5 plots the deposition techniques most frequently cited in the literature for preparing TMD-containing composites used at High Temperatures. The weaker thermal stability of TMDs may be the reason for the slightly higher number of references about PVD in this instance than about silver. Low-temperature deposition methods like PVD may therefore become more beneficial because thermal degradation of TMDs during sample preparation is a significant problem for self-lubricating materials, as it will

influence their properties at HT [12]
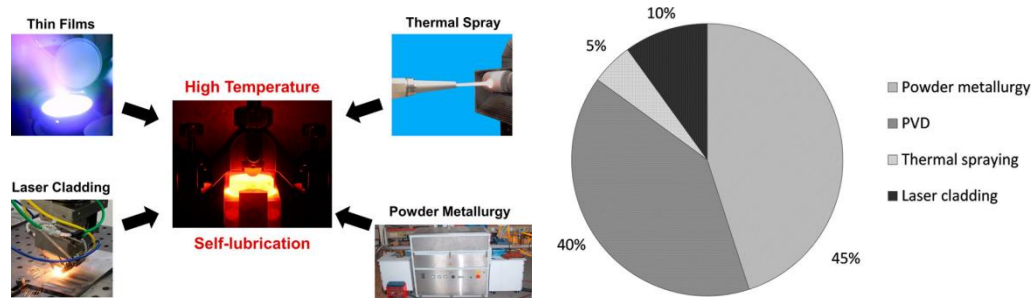
Figure 1.5: An overview of the most widely reported techniques used for the preparation of self-lubricating materials (right), Share of deposition techniques for HT self-lubricating materials with TMD content (left) [1]

A practical technique for creating lubricating films is sputter deposition. The resultant films are thin (typically on the order of 1 μm thickness) and generally stick well to most surfaces, making them ideal for applications requiring acceptable tolerances in mechanical devices. However, slight differences in the crystallite shapes and chemical compositions of these films determine their actual lubricating performance (friction coefficients and durabilities) [11].

1.3 Thin films (Coating)

The world we know today would be a different place without thin films. They are the backbone of every electronic component and the cornerstone of a myriad of products of everyday use in the world. These films find applications in various disciplines, given our ability to engineer their intrinsic properties to match those required in practice. Examples are numerous. The lifetime of equipment such as drill bits, gears and bearings can be extended by depositing a thin protective coating that can withstand more friction and wear without significant structural damage; nanocrystalline silver is used as an antimicrobial barrier in dressings for the treatment of burns and wounds that otherwise may readily infect with catastrophic consequences; SiO_2 and Al_2O_3 films are used as moisture and light barriers in the food packaging industry; and finally, the entire semiconductors industry is based on our ability as engineers to deposit a great variety of films with distinctive properties.

Over the last century, these engineered films evolved from a scientific curiosity to a well-developed technology. The term thin lm eludes a formal definition; thin does not convey the scale it refers to. A more formal definition is that a thin film

is a coating of a material placed or deposited on top of another (the substrate), and the thickness of this film is less than a few micrometres. A practical limit is usually taken at 1 μm, but we may find that films are labelled thin even when their thickness is about 2-5 μm. Once in thin film form, the material's properties substantially differ from those that are palpable and measurable to our senses. In practice, real-life applications of thin films require a good understanding of the fundamentals of thin film growth and how the material is brought in contact with the substrate. This knowledge is essential for the development of novel materials with tailored properties. With these thin films, we are fulfilling one of the dreams of ancient alchemists: changing the looks and properties of an unattractive and easy-to-find material to those that please our demands.

One of the methods to tailor the material's properties is to carefully control how it is deposited. These thin films' properties are dictated by the way they are deposited and their physical dimensions. For instance, for films of a few microns in thickness, the material's properties are close to those of the bulk, but once the film is fragile (a few nanometres), the fundamental physical properties of the material change. Additionally, by controlling the morphology of the film, we can modify the material's intrinsic properties according to our technological needs.

One of the most popular methods to deposit these thin films is known as physical vapour deposition (PVD). In PVD methods, the material to deposit is first vaporised in a controlled environment. Then, the vapour is in contact with the substrate upon which it condenses. The condensation of these vapours is a natural phenomenon easily observed in daily life; we are all familiar with the condensation of water vapour on surfaces. The physical mechanisms that drive the formation of foggy windows on a cold winter day are essentially the same as those put forward during a typical PVD process.

1.4 Sputtering

Among PVD techniques, sputtering is one of the most widely used processes in academia and industry due to its unique characteristics. There are three that stand out for their industrial impact: versatility, controllability and repeatability. The first one is all about size. Sputtering is a malleable technology since it is simple to scale up or down according to the needs of the process. The second characteristic refers to control. In an industrial setup, complete control over the

process is essential for successfully implementing the technology. Lastly, repeatability alludes to producing films with the same properties consistently. These distinct attributes of sputtering turn it into one of the preferred methods for industrial applications. Sputtering has permeated industrial environments, and it is nowadays widely used all over the world. According to BCC Research, the total area coated by sputtering techniques in 2011 is expected to be more than 1.2 billion m^2, and this number may reach 1.8 billion by 2016, representing almost 1/5th of the total global market for thin films worldwide [13]
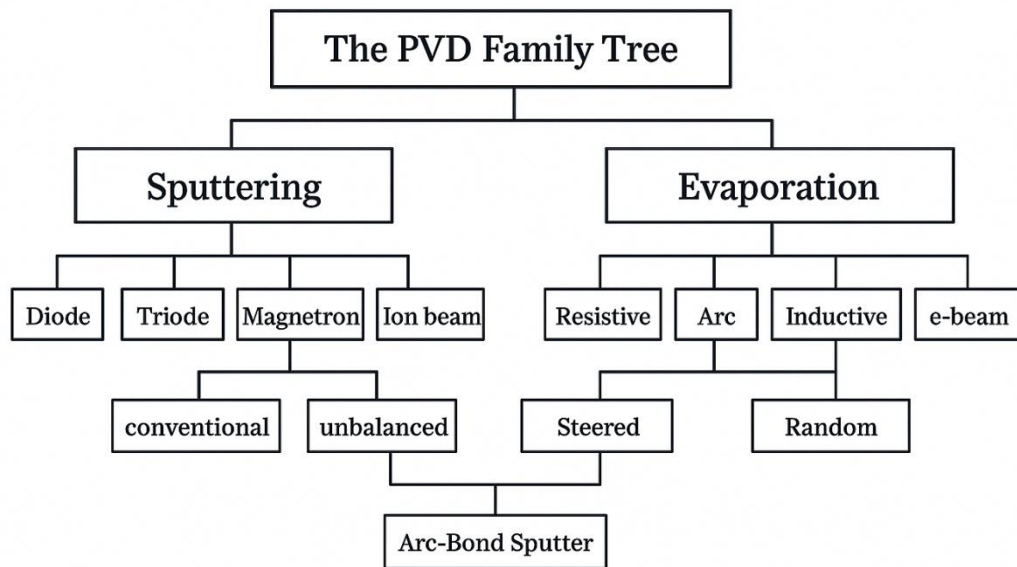
Figure 1.6: The PVD family tree [14]

One of the first methods for forming thin films is vacuum evaporation, which is often used to deposit metals and metal alloys. There are essentially three key processes in the evaporation process.

a) Boiling or sublimating a source material produces a vapour.

b) The vapour is then transferred from the source to the substrate.

c) The thin film is created when the vapour condenses on the substrate.

Since the vapour must be moved from its source to the substrate, a high vacuum is necessary to guarantee that it does so without being hampered by other species that might react with it. Sputtering physically removes the thin layer of species from the source by subjecting a source (also referred to as a target) to a barrage of atomic or molecular particles. Ions from a gas discharge are utilised in the most basic and popular sputtering procedures to bombard the target at a specific energy. A portion of the target atoms are dislodged and "sputtered" from the

target surface if the bombardment energy is high enough. The target acts as the discharge's cathode and is often negatively biased. The discharge ions are accelerated toward the target surface by the cathode sheath that forms in front of the target.
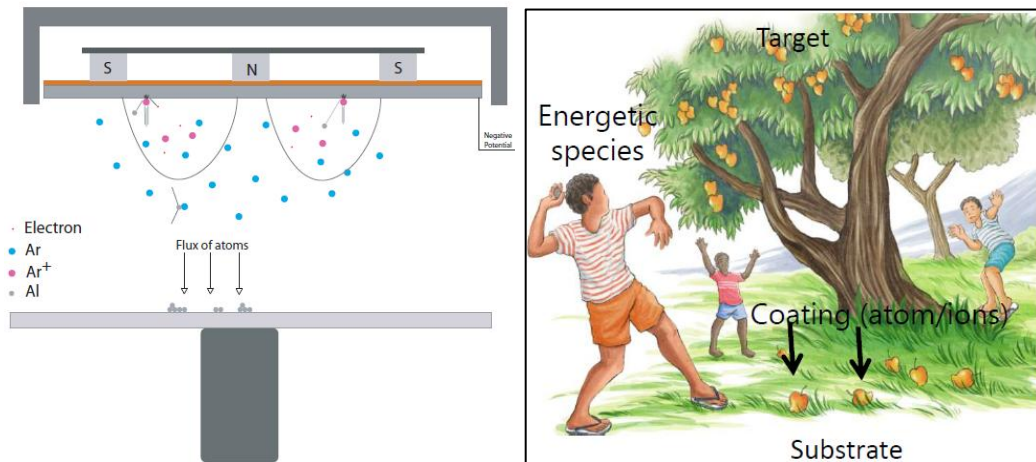
Figure 1.7: Schematic and analogy illustrating the sputter deposition process: (left) magnetron sputtering setup showing atom/ion flux from the target to the substrate; (right) real-life analogy where energetic species (children) knock coating atoms (fruit) from the target (tree) onto the substrate (ground), visualising the transfer of material during thin film deposition.

A standard magnetron sputtering process bombards a surface (the target) with high-energy particles. We can picture the surface of a material, a metallic surface, for instance, as made of a myriad of atoms arranged in structured arrays, forming crystals. The impact of a fast particle with a highly ordered ensemble of atoms is similar to the breaking of the rack during a typical game of pool: the physics behind the cue ball dispersing the ordered colored balls during the opening shot is, in essence, the same that describes the fundamental principles of sputtering. The aftermath of these collisions is the eventual release of atomic particles from the surface. These particles then travel through a gaseous medium to finally reach the substrate, where they condense. Another example would be the total heat flux bombarding the substrate. Depending on the process, we may be required to decrease the heat load at the substrate without significantly reducing the deposition rate. A third example pertains to one of the main drawbacks of sputtering as a deposition process: the nonuniform erosion of the target. This nonuniformity restrains the continuous operation of the process since targets need to be replaced constantly. This necessary cycle significantly reduces the time the deposition system is up and running. A deep understanding of the

mechanisms that drive the modifications in the process would allow scientists and engineers to fine-tune and optimise the process.

1.4.1 The DC Glow Discharge

Applying a voltage between two electrodes in a gas produces a glow discharge. Since every gaseous atom is neutral at first, there is no current flow. The electric field between the electrodes will accelerate the entry of an electron (or other charged particle) into the gas, which usually occurs when a cosmic ray, radioactive contaminants, a charge multiplication process, or background radiation ionise a gas atom. An inelastic collision with a gas atom may cause the gas atom to be excited or ionised if the electron's kinetic energy is high enough. A second electron is emitted into the gas if ionisation occurs. Gas breakdown will then arise due to both electrons being accelerated once more.
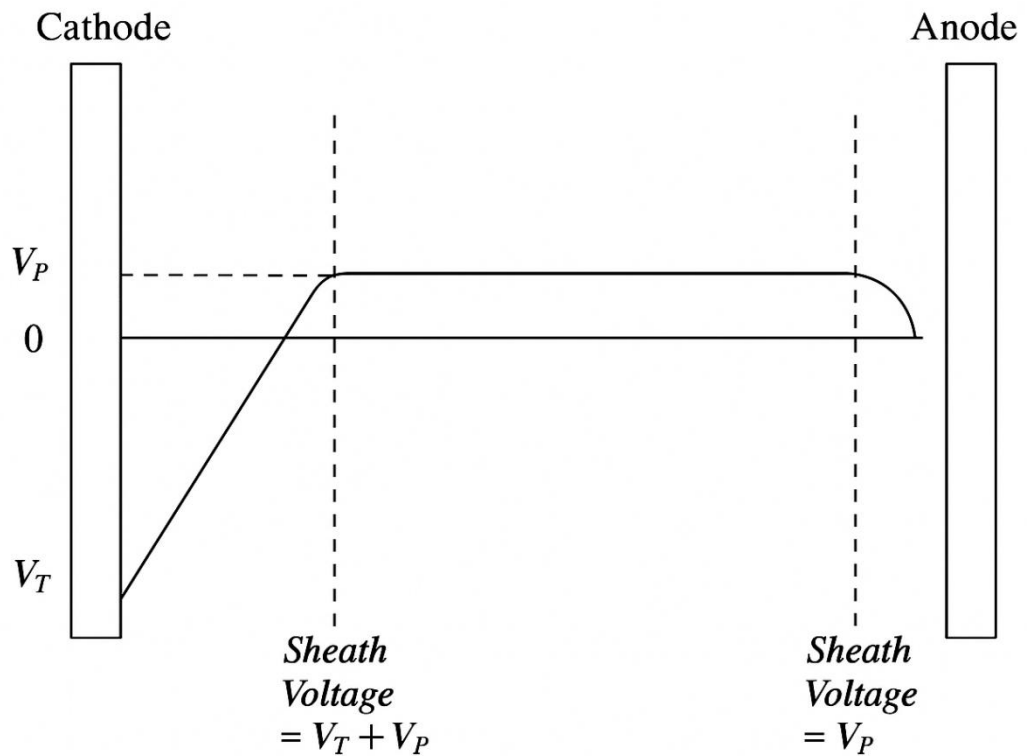
Figure 1.8: Voltage distribution in a DC glow discharge [15]

The breakdown voltage depends on the electrode spacing, gas pressure, and the electrode potential difference needed to start a discharge. This relationship between pressure, spacing and breakdown voltage is known as Paschens' relationship. [16] The DC discharges of interest in film deposition are typically low-density plasmas with neutral to ion ratios 10^4. The electrons and ions in the plasma eventually become lost to the discharge through collisions with surfaces,

electron-ion recombination, etc For the plasma to maintain itself, there needs to be a balancing amount of ionising processes occurring in the discharge.

An external DC or RF power source can apply a bias voltage to the substrate. The external power supply now controls the voltage on the substrate, Vb, while the plasma potential remains constant. This substrate bias can significantly influence the characteristics of the growing film. The net deposition rate may be decreased or even turned negative in specific situations (sputter etching).

The voltage distribution of a DC glow discharge appears in Figure 1.8. The system's electric fields are contained within the sheaths in a DC discharge. At each electrode, the sheaths work to repel electrons. [15]. In addition to having a sheath, a floating substrate submerged in the discharge will be negatively inclined toward the plasma. This is due to the difference in the mobility of the electrons and the ions in the plasma. When a substrate is first immersed in the discharge, it is subject to bombardment from electrons, ions and neutrals. [17]

1.4.2 RF Discharges
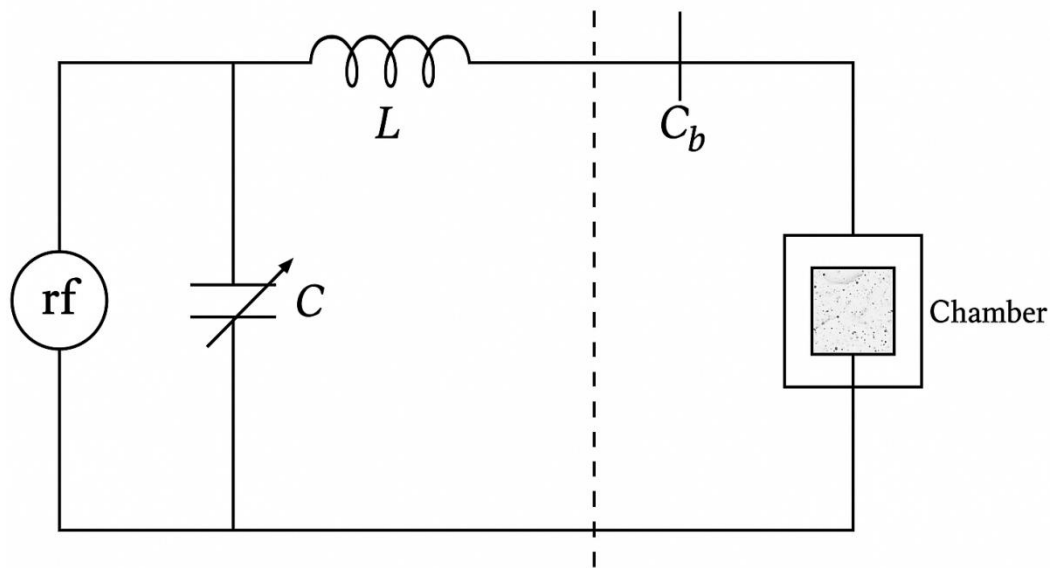
Figure 1.9: RF sputtering configuration [17]

Sputtering non-conductive materials is required in some circumstances. SiC2 sputter etching before metal deposition is a typical example. Unfortunately, a plasma cannot be ignited by delivering a DC voltage to an insulating cathode because the accumulation of a positive ion surface charge on the front side will cause the effective voltage on the cathode surface to approach zero. This restriction can be overcome by substituting an RF source for the DC supply. A

typical RF sputtering setup is shown in Figure 1.9. A blocking capacitor separates the matching network and the target. The target region is usually substantially smaller than the anode of the system (chamber walls, etc.). This asymmetrical design creates a negative DC bias on the target, resulting in sputtering [17]

1.4.3 Magnetron Sputtering

A magnetron discharge is a variant of the glow discharge that includes utilising magnets, usually situated at the back of the cathode, to reduce the electron mean free path and confine electrons in the vicinity of the cathode. The magnetic field effect can dramatically improve the deposition rate while lowering the minimum operating pressure. Constricting the electrons in the cathode region has the added advantage of decreasing the substrate's electron bombardment. This impact is particularly relevant when working with temperature-sensitive substrates. This reduced electron loss in the target region leads to an increase in electron density in the discharge. Higher electron density makes it feasible to lower the voltage supplied to the plasma. A typical diode sputtering system operates between 1000VDC and 10,000VDC, while a magnetron plasma may normally operate between 200VDC and 800VDC. The magnetron can function at lower pressures because the electrons' mean free path in the magnetic field is lowered.

Magnetrons are built so that the magnetic field traps electrons near the target surface, increasing their ionising power. The magnetic field immediately affects the electron after it is expelled from the surface. The magnetic lines loop between the inner and outer magnetic poles, creating a closed magnetic field. The magnetron configuration has the disadvantage of etching away the target surface in an irregular pattern. The electric and magnetic fields limit electrons to specific locations before the target surface, known as the racetrack region. Magnetrons come in a variety of forms and sizes. For large substrates, the magnets are sometimes turned toward the back of the magnetron to maximise target utilisation.

This kind of magnetron design aims to confine the electrons in the target area. Because the magnetic fields limit the plasma to the target region, this design minimises the electron and ion bombardment of the substrate. Ion bombardment of the substrate is preferable in some circumstances. The depositing film may

resputter due to ion bombardment, which may aid in filling in gaps. Additionally, it can be utilised to change the stoichiometry of the depositing film. Ion bombardment is used to densify and harden films in mechanical engineering applications requiring wear resistance. By altering the magnetic field design to enhance the magnetic field intensity of the inner or outer set of magnets compared to the other set, more ions will be accessible to bombard a substrate. This kind of magnetron, called an unbalanced magnetron, was initially proposed by Window and Sawides. [18].
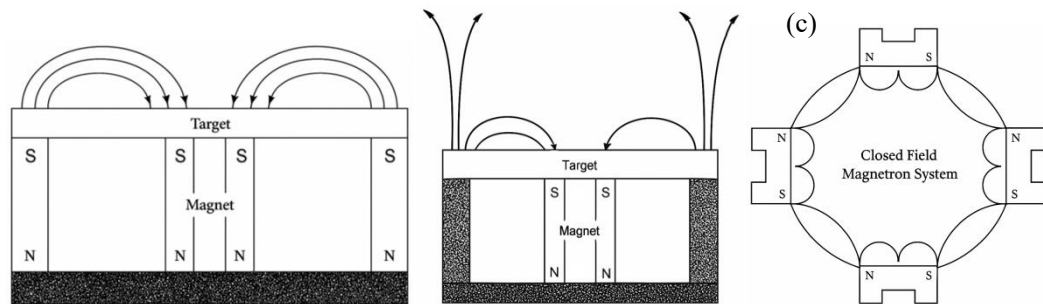
Figure 1.10: (a) Balanced Magnetron; (b) Unbalanced Magnetron; (c) Closed Field Magnetron System [17]

1.4.4 Closed Field Magnetron Sputtering

Ion bombardment of the substrate during film formation is crucial for some applications. This is especially true for *wear-resistant applications* requiring robust, dense films. Earlier in this chapter, the idea of the unbalanced magnetron was covered, along with an explanation of how it can expand the plasma zone. To create an effective magnet trap for the electrons, closed field magnetron sputtering entails symmetrically arranging several unbalanced magnetrons around the substrate so that the magnetic field lines join. This type of magnetic field closure raises the plasma density in the substrate region, allowing for much greater ion currents to reach the substrate.

1.5 Actuators

An actuator is a device that transforms energy into motion. This energy can originate from a variety of sources, including electricity, hydraulic fluid, or atmospheric pressure. The primary function of an actuator is to generate motion or operate a system. This motion might be linear (in a straight line) or circular.

The nomenclature of missile actuators and their mating parts is typically based on their function, configuration, and the type of actuation mechanism used.

Missile actuators are critical for moving control surfaces such as fins or canards to steer the missile during flight. They are commonly classified by their actuation method: hydraulic, pneumatic, electromechanical, or pyrotechnic.
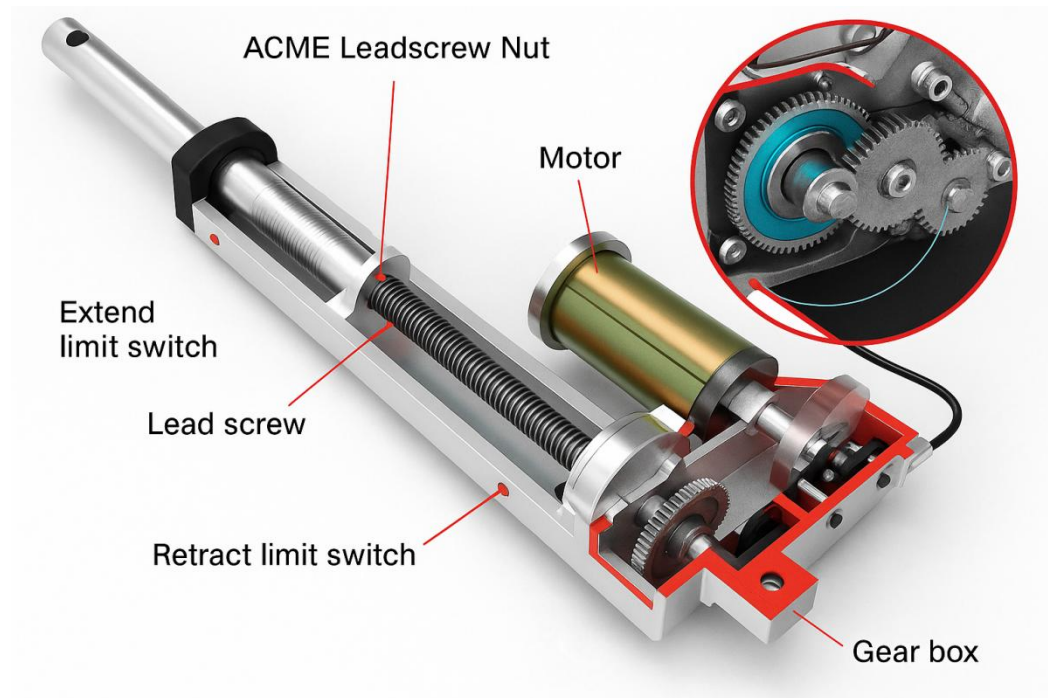
Figure 1.11: Cutaway view of an electric linear actuator showing key components: ACME leadscrew nut, lead screw, extend and retract limit switches, motor, gear box, and detailed gear arrangement (inset), illustrating the conversion of rotary motion from the motor to precise linear motion for actuation [19].

For example, a pneumatic actuator system includes parts such as a high-pressure gas source, a manifold, a regulator, fill and vent lines, fill and vent valves, an actuator housing, actuator vanes, an actuator shaft, and the control surface (fin). The actuator housing contains vanes attached to a shaft, which rotates to move the missile fin. Mating parts include locking pins, yokes, and spring housings that secure the fin in position and ensure proper deployment and retraction. In electro-mechanical systems, nomenclature comprises components such as electric drive motors, cam members, solenoids, moment arm assemblies, ball joint assemblies, and biasing springs, each named according to its mechanical function and position in the assembly4. Additionally, specialised actuators like the TiNi™ Frangibolt® are designated by size (e.g., FC3, FC4, FC6, FC8) and are mated with correspondingly sized titanium fasteners, which are custom-manufactured for specific preload requirements. The precise naming convention ensures clarity in design, manufacturing, and maintenance, with each

part's name reflecting its role and compatibility within the actuator system.

1.6 Summary and dissertation outline

This thesis investigates the development and characterization of molybdenum disulfide-titanium (MoS_2-Ti) multilayer solid lubricant coatings deposited via magnetron sputtering for applications in missile actuator systems. The research addresses a critical engineering challenge in defense technology: providing effective lubrication in extreme operating environments where conventional liquid lubricants fail due to thermal degradation, evaporation, and inability to maintain performance under high-stress conditions. The unique lamellar structure of transition metal dichalcogenides, particularly MoS_2, with its strong in-plane covalent bonds and weak interlayer van der Waals forces, offers an ideal solid lubrication mechanism capable of functioning in vacuum, high temperature, and high-pressure environments typical of missile operation.

By systematically optimizing deposition parameters and developing a bilayer architecture incorporating a titanium interlayer, this work aims to enhance coating adhesion, mechanical durability, and tribological performance specifically for 17-4 PH stainless steel components used in precision missile actuators. The incorporation of titanium addresses key limitations of pure MoS_2 coatings, including poor adhesion to metallic substrates, susceptibility to humidity degradation, and inadequate load-bearing capacity. Through rigorous parameter optimization and detailed microstructural and tribological characterization, this research establishes a robust methodology for indigenous development of high-performance solid lubricant coatings that meet the demanding requirements of aerospace and defense applications.

Chapter 1 presents the fundamentals of solid lubrication, transition metal dichalcogenides, and their relevance to missile actuator systems. Introduces the concept of PVD sputtering for thin film deposition and outlines the research motivation.

Chapter 2 provides a comprehensive literature review of MoS_2 and Ti-doped MoS_2 coatings, their tribological performance, and applications in mechanical systems. Identifies research gaps and formulates specific objectives for the current work.

Chapter 3 details the experimental apparatus, materials selection, sample preparation techniques, coating deposition procedures, and characterization methods employed in this study.

Chapter 4 documents the systematic approach to optimizing sputtering parameters for both Ti and MoS_2 layers, substrate effects, and multilayer architecture development.

Chapter 5 presents comprehensive characterization of coating microstructure, composition, and morphology using SEM, XRD, and Raman spectroscopy. Analyzes tribological performance through pin-on-disc testing, evaluating friction, wear, and durability.

Chapter 6 summarizes key findings, highlights the scientific and technological contributions, and suggests directions for further research and development.

Chapter 2

Literature survey and Problem Formulation

Transition metal dichalcogenides (TMDs), such as molybdenum disulfide (MoS_2), have been extensively studied for solid lubrication due to their layered structure, low shear strength, and adaptability to extreme environments. This chapter synthesises key findings from recent research on TMD-based coatings, focusing on compositional modifications, deposition techniques, and performance in tribological applications.

In tribology and solid lubrication, especially with molybdenum disulfide (MoS_2) coatings, extensive research has focused on understanding and optimising their structural, mechanical, and tribological properties for advanced engineering applications. The unique lamellar crystal structure of MoS_2, characterised by strong in-plane covalent bonds and weak interlayer van der Waals forces, underpins its excellent lubricating performance in extreme environments such as vacuum, aerospace, and high-load mechanical systems. Over the decades, developments in deposition techniques such as sputtering and magnetron sputtering have enabled precise control over film morphology, orientation, and composition, which are critical for achieving low friction, high wear resistance, and environmental stability. Researchers have demonstrated that doping MoS_2 with metals (e.g., Ti, Ta, Cr, W) or designing multilayer and composite structures can further enhance hardness, adhesion, and oxidation resistance, thus extending the operational lifetime of coatings under harsh conditions. The literature also highlights the importance of substrate preparation, film thickness, and deposition parameters in tailoring microstructure and tribological behaviour for specific applications.

2.1 Literature survey

The classic study by Holinski and Gänsheimer (1972) [8] explores the lubricating mechanism of a surface coated with MoS_2 powder (-50 μm) by sponge. The authors attribute the displacement of large MoS_2 planes to requiring greater shearing forces than those needed to replace small basal planes. Their experiments show that MoS_2 forms a homogeneous, continuous film on metal surfaces during

the running-in process, with the basal planes aligning parallel to the substrate. The study found that the sliding of MoS$_2$ layers is only feasible on the basal plane. The study shows that crystal planes pushed over each other stick to the new MoS$_2$ plane and contribute to film formation. The paper provides foundational insights into the structural and mechanistic origins of MoS$_2$'s solid lubrication performance.
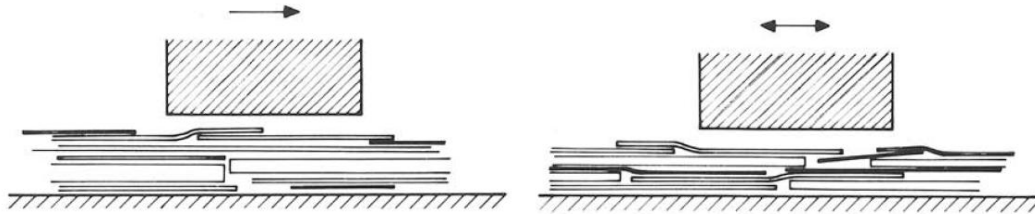
Figure 2.1: Arrangement of the layers during rotational (left) and oscillational (right) movement [8]

E. Buck (1983) [2] Systematically investigates the morphological properties of sputtered MoS$_2$ films, emphasising how deposition parameters influence the orientation, size, and distribution of lamellae, which are critical for tribological performance. The study demonstrates that sputtered MoS$_2$ films are typically microcrystalline, with lamellae often oriented perpendicular to the substrate. Still, their size and orientation can be tailored by adjusting sputtering conditions such as argon pressure, water vapour partial pressure, and substrate-target distance. Notably, the research shows that the substrate's macroscopic geometry and the sample holder's design can induce a preferred parallel orientation of lamellae, which is favourable for achieving low friction in applications like bearings. The findings highlight that random or misoriented lamellae increase surface area and oxidation susceptibility. The paper also cautions that results from flat specimens may not directly translate to curved surfaces unless coating morphology is carefully controlled.

19
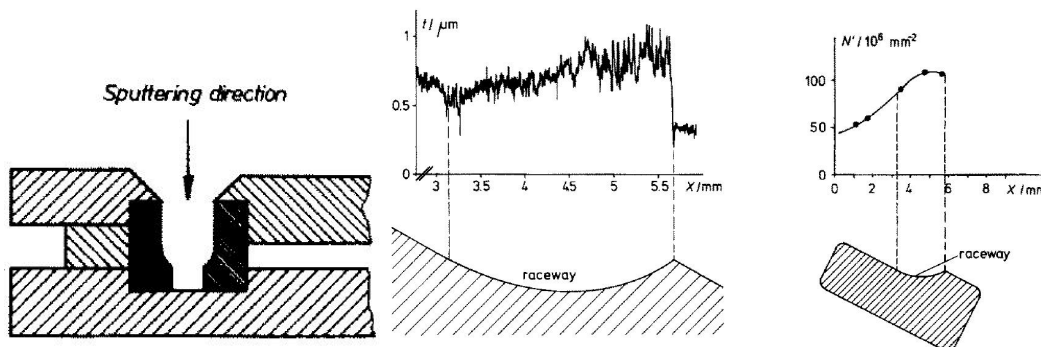
Figure 2.2: Cross section of the sample and mounting assembly (detail). Thickness t of a sputtered MoS$_2$ film across a bearing raceway. The size of the lamellae, expressed in terms of N', is across the bearing surface. [2]

Renevier et al. (1999) [20]   Presents a comprehensive study targeting dry machining and forming tool applications. Industrial evaluations show that MoST coatings, especially when applied over hard coatings like TiN or TiCN, dramatically extend tool life and productivity in cutting and forming operations, outperforming conventional hard coatings in dry and lubricated conditions. Applications include drilling, end milling, punching, fine blanking, and drawing, where coated tools consistently produce more parts and maintain better surface finish with reduced wear. The study underscores the potential of MoS$_2$/titanium composite coatings as robust, self-lubricating solutions for demanding industrial environments where traditional lubricants are impractical or undesirable.

	Uncoated	TiCN	TiCN + MoST
Number of parts	5,000	6,000	27,000

	Uncoated	TiCN	TiCN + MoST
Number of parts	15,000	50,000	200,000
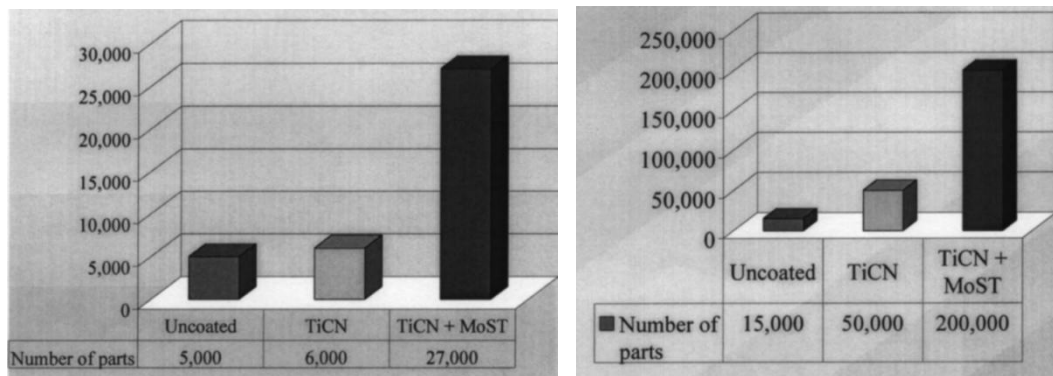
Figure 2.3: Results of MoST piercing application on AISI D2 steel without lubricant in lubricated conditions (water-soluble 20%) [20]

D. G. Teer (2001) [21]   introduces innovative coatings based on molybdenum disulfide (MoS$_2$) and graphite, designed to combine low friction with high hardness, wear resistance, and load-bearing capacity. These coatings, termed MoST™ and Graphit-iC™, are developed using magnetron sputter ion plating methods, which enhance adhesion and structural density compared to conventional techniques. The study highlights the tribological superiority of these coatings, including remarkably low wear rates and friction coefficients under various conditions, such as humid atmospheres and water immersion. Structural investigations reveal amorphous or fine-crystalline forms; when metal is added to the Graphit-iC, the hardness decreases, whereas the MoST's hardness increases.

The high hardness mixed with low friction results in very low wear rates, while the mechanical qualities of the coatings combined with exceptional adhesion result in very high load-bearing capacity. More research is needed to elucidate the mechanisms underlying the low friction and wear rate. They have been demonstrated to offer significant potential in many heavily loaded applications, including gears and engine parts, where coatings have hitherto had little or no effect.
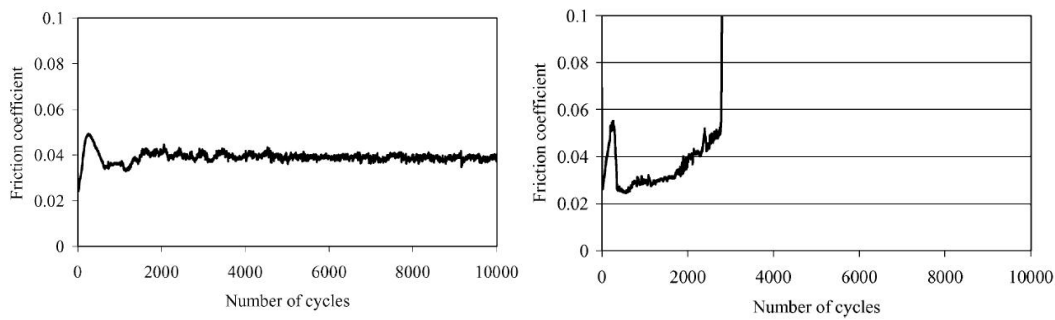
Figure 2.4: The 100N reciprocating wear test of MoST coating at 41% humidity (Left) and under water (Right) [21]
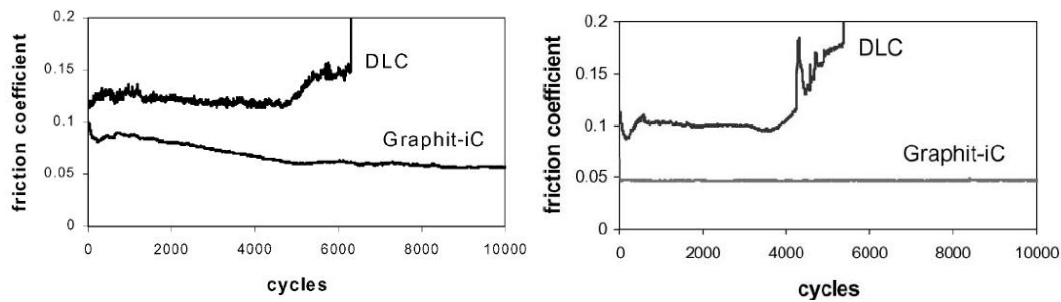
Figure 2.5: 100N reciprocating wear test of Graphit-iC and DLC in ambient conditions (left) & de-ionised water (right).[21]

N. M. Renevier et al. (2000) [22] Investigate sputter-deposited MoS_2/metal composite coatings, such as MoST™, enhanced with Ti, Cr, W, or Zr. These coatings exhibit superior hardness (10–15 GPa), adhesion (critical load >120 N), and wear resistance (wear rates ~10^{17} m³ m³/Nm) compared to pure MoS_2, while maintaining low friction coefficients (0.02–0.04) even under humid conditions. Structural analyses reveal amorphous or fine-crystalline matrices, with metal additions distorting the MoS_2 lattice and inhibiting crystallinity, contributing to enhanced mechanical properties. TEM failed to detect multilayers within the bulk of the MoS_2/Ti composite coatings, which showed an almost amorphous coating.

21

The coatings demonstrate exceptional performance in industrial applications, including cutting tools and automotive components, outperforming traditional coatings like TiN and DLC in load-bearing capacity and environmental stability.

Metal	Parameters	2 N	10 N	40 N	80 N
No metal	Friction coefficient	0.058	0.055	0.026	0.019
	Wear (m^3/mN)	2.40×10^{-15}	2.59×10^{-15}	5.48×10^{-16}	3.00×10^{-16}
	Track width (μm)	156	176	250	318
Titanium	Friction coefficient	0.105	0.082	0.059	0.042
	Wear (m^3/mN)	4.21×10^{-16}	1.76×10^{-16}	5.95×10^{-17}	1.01×10^{-17}
	Track width (μm)	68	98	165	210
Zirconium	Friction coefficient	0.115	0.082	0.054	0.031
	Wear (m^3/mN)	1.47×10^{-16}	3.16×10^{-17}	9.15×10^{-18}	3.42×10^{-17}
	Track width (μm)	62	104	167	235
Chromium	Friction coefficient	0.152	0.078	0.049	0.027
	Wear (m^3/mN)	4.41×10^{-16}	7.81×10^{-17}	1.31×10^{-16}	3.08×10^{-17}
	Track width (μm)	72	78	172	208
Tungsten	Friction coefficient	0.044	0.032	0.020	0.018
	Wear (m^3/mN)	2.74×10^{-17}	6.32×10^{-17}	2.74×10^{-17}	2.59×10^{-17}
	Track width (μm)	96	144	177	217

Table 2.1: Pin on disc test performed for 3600 s, except for pure MoS$_2$, which failed after 842 s at 80 N, failed after 850 s at 40 N, and failed after 2426 s at 10 N [22]

Run	1	2	3	4	5	6	7	8	9
Mo (at.%)	36.40	39.44	45.88	35.04	41.84	36.04	37.68	28.01	39.08
S (at.%)	51.82	48.09	43.46	51.19	53.89	39.13	60.02	41.25	55.65
Ti (at. %)	11.78	12.46	10.66	13.77	4.27	24.83	2.30	30.74	5.26
N_S/N_{Mo}	1.42	1.21	0.94	1.46	1.28	1.08	1.59	1.47	1.42
N_{Ti}/N_{Mo}	0.32	0.31	0.23	0.39	0.10	0.68	0.06	1.09	0.13

Table 2.2: Quantitative results of Elemental Analysis of MoS$_2$- Ti Films determined by EDS [4]

Arslan et al. (2004) [4] Reveals that Ti incorporation disrupts MoS$_2$'s crystallinity, forming quasi-amorphous structures with (002) basal plane orientations, while enhancing hardness and wear resistance under atmospheric conditions (wear rates ~1.02–5.51 ×10^{-6} mm³/Nm). This aligns with broader research showing that metal-doped MoS$_2$ coatings (e.g., Ti, Cr, W) exhibit superior tribological performance due to denser microstructures and oxidation resistance than pure MoS$_2$. The work complements studies on MoS$_2$/metal multilayers (e.g., MoS$_2$/Ti– MoS$_2$/Si), where modulated architectures and dopants inhibit columnar growth, reduce friction ($\mu \approx 0.02$–0.08), and improve load-bearing capacity. The highest NS/NMo (1.59) ratio was reached with the lowest bias (−30 V) and the highest working pressure (0.40 Pa). However, contrasting findings highlight oxygen's dual

role: while traditionally deemed detrimental, oxygen-rich Mo–S–O coatings demonstrate ultra-low friction ($\mu \approx 0.02$) via trioactivated crystalline MoS_2 formation. These collective advances position Ti-alloyed MoS_2 as a robust solid lubricant for industrial applications requiring environmental stability and mechanical durability.

Wang et al. (2007) [23] Reveals that pure MoS_2 coatings are predominantly amorphous, while MoST coatings with Ti (15.3–19.5 at.%) exhibit a composite structure of amorphous and nanocrystalline phases, with crystallinity increasing alongside Ti content. As confirmed by scratch testing, the incorporation of titanium leads to significant improvements in hardness (from ~500 HV to over 1000 HV), elastic modulus, and adhesion. Total failure of the MoS_2 and low-Ti MoST coatings occurs at a load of 36 N and 84 N, respectively; however, for the high-Ti MoST coatings, no failure occurs even up to 100 N. Tribological tests show that MoST coatings possess much lower friction coefficients (0.1–0.15) and drastically enhanced wear resistance than pure MoS_2, especially in humid air, where pure MoS_2 degrades rapidly. The study attributes these enhancements to the microstructural evolution induced by Ti addition, which promotes denser and more robust composite phases. These findings underscore the potential of MoST coatings for demanding industrial applications, particularly in cutting and forming tools where mechanical durability and low friction are essential.
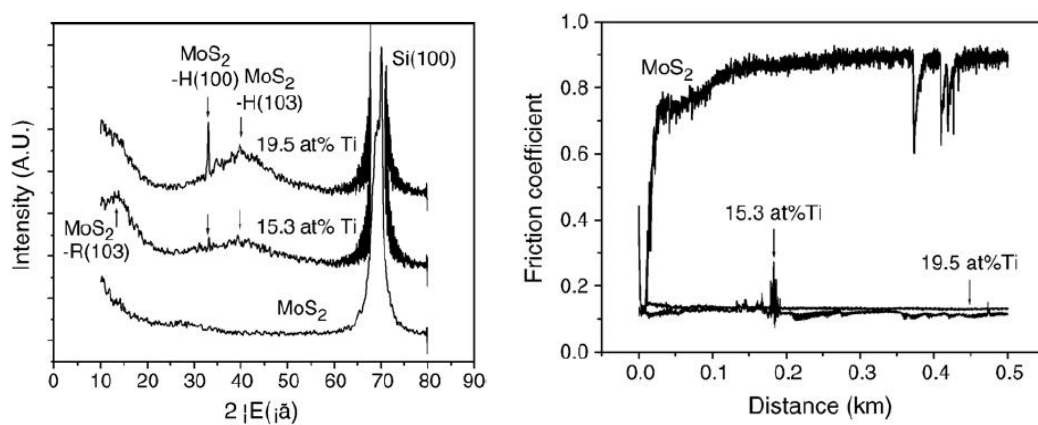
Figure 2.6: X-ray diffraction patterns of MoST coatings with different titanium content (left); Tribological results for the MoST coatings with different titanium content at 10 N load, 25 °C and 38% humidity (right) [23]

Singh et al. (2015) [24]   Investigating Ti-doped MoS_2 coatings containing approximately 16 at% Ti and exhibiting an amorphous structure. Characterisation revealed excellent adhesion, high hardness (7.9 GPa), and a dense, nonporous morphology. Tribological tests showed that the coatings maintained low and stable friction coefficients (as low as 0.06) and low wear rates, with performance influenced by humidity and temperature; friction and wear decreased at higher temperatures and lower humidity. Notably, the study was the first to assess the rolling contact performance of Ti-MoS_2 films, demonstrating that their effectiveness as solid lubricants in bearings depends on coating retention, with exceptional results in vacuum environments. Microstructural analysis indicated that sliding induces partial re-crystallisation of MoS_2 within the wear track, enhancing tribofilm formation and durability. These findings highlight the potential of Ti-doped MoS_2 coatings for advanced bearing and sliding applications, particularly where low friction and robust wear resistance are required in challenging environments.
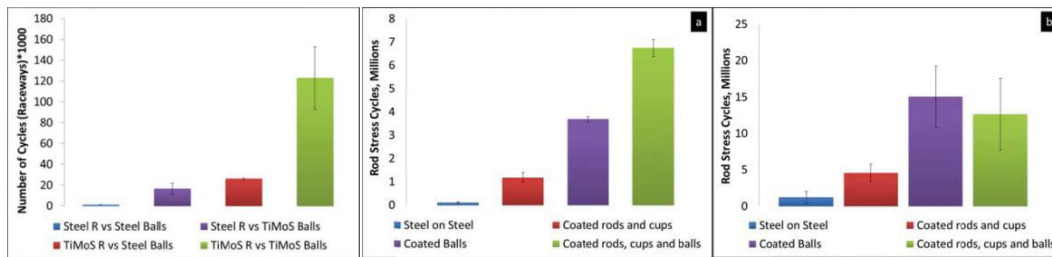
Figure 2.7: Comparison of rolling contact behaviour of thrust ball bearings(left); Rolling contact behaviour of different material pairs tested in ball-on-rod tribometers in (a) humid air (40–45% RH) and (b)vacuum (2×10^{-6} Torr) [24]

Kong et al. (2020) [25] demonstrate that introducing Ti and Si into the multilayer structure significantly enhances hardness, reduces internal stress, and inhibits the formation of detrimental columnar structures compared to pure MoS_2 coatings. XRD and HRTEM analyses reveal that the coatings predominantly exhibit a (002) orientation and a denser microstructure, with Ti and Si present in amorphous or nanocrystalline forms. Tribological tests show that the optimised multilayer coating achieves a notably low friction coefficient (~0.0432) and wear rate ($3.22 \times 10 - 73.22 \times 10 - 7$ mm³ $N^1 m^1$) under heavy load, attributed to improved compactness and the formation of robust transfer films. The multilayer interfaces effectively hinder dislocation motion and crack propagation, resulting in superior

wear resistance and mechanical durability. This study provides specific instructions for improving the mechanical and tribological properties of MoS$_2$ coatings.
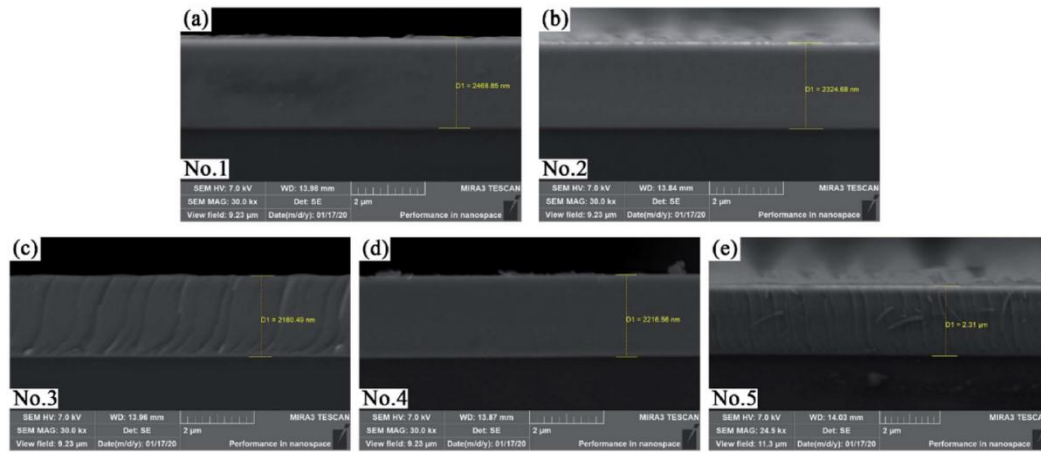
Figure 2.8: The cross-section morphology of MoS$_2$/Ti–MoS$_2$/Si multilayer nanocomposite coatings by SEM. [25]
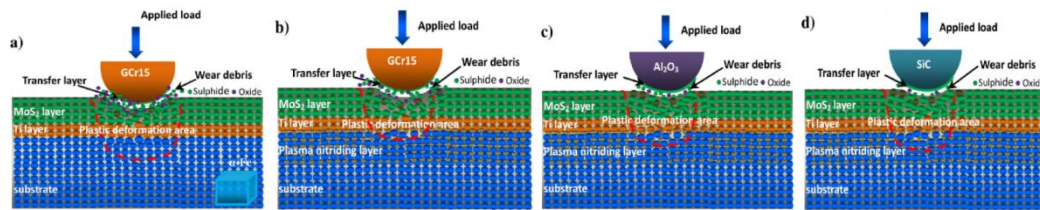
Figure 2.9: Schematic diagrams of wear mechanism of the samples under air: a) (Ti/MoS$_2$)/GCr15; b) (PN + Ti/MoS$_2$)/GCr15; c) (PN + Ti/MoS$_2$)/Al$_2$O$_3$, and d) (PN + Ti/MoS$_2$)/SiC [25]

Xingguo Feng et al. (2021) [23] investigate Ti/MoS$_2$ films deposited on plasma-nitrided CF170 steel, focusing on their performance against different mating materials. The study demonstrates that duplex treatment—combining plasma nitriding with Ti/MoS$_2$ film deposition—significantly enhances the substrate's load-bearing capacity, film adhesion, and hardness compared to single-layer Ti/MoS$_2$ films. Structural analyses reveal a dense, columnar Ti/MoS$_2$ film with strong (002) orientation. At the same time, tribological tests show that the duplex-treated samples exhibit lower friction coefficients and wear rates, especially when sliding against SiC and Al$_2$O$_3$ balls under air, compared to GCr15 steel balls. The improved wear resistance is attributed to the formation of effective MoS$_2$ transfer films, higher contact pressure, and reduced oxidation, with wear rates decreasing up to sevenfold for ceramic counterparts. The research highlights that plasma

nitriding improves mechanical support and optimises tribological performance, making the duplex system promising for high-load, long-lifetime applications in demanding environments.
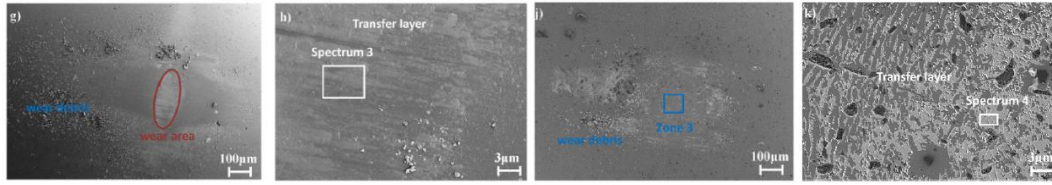
Figure 2.10: The wear scars for the films with various friction pairs: g) & h) for (PN + Ti/MoS$_2$)/Al$_2$O$_3$; j) & k) for (PN + Ti/MoS$_2$)/SiC [26]
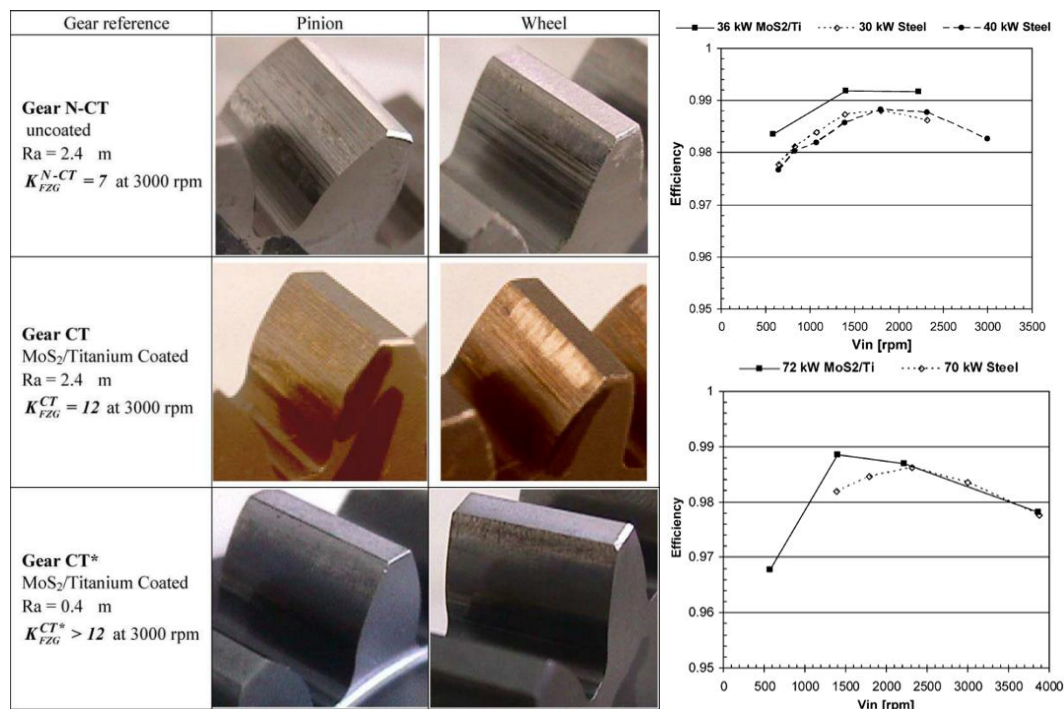
Figure 2.11: Images of the teeth flanks at the end of the tests performed at 3000 rpm (left); Efficiency of the transfer gearbox at constant input power 36 kW & 72 kW (right) [27]

Amaro et al. (2005) [27] found that twin-disc tests under high contact pressures and severe sliding conditions show that the coating undergoes only mild, progressive wear without catastrophic failure, indicating strong suitability for gears. FZG gear scuffing tests reveal that MoS$_2$/Ti-coated gears achieve significantly higher scuffing resistance, improving by 2 to 5 FZG load stages and enabling up to 77% more transmitted power than uncoated gears. Gearbox efficiency tests further indicate that coated gears reduce friction losses, resulting in about 0.5% higher efficiency at high torque and low speed. These results highlight

the MoS₂/Ti coating's potential to enhance gear durability, load capacity, and efficiency, making it especially valuable for demanding and environmentally conscious applications.

Martins et al. (2006) [28] Examines the application of a multilayer MoS₂/Ti composite coating to gears to improve efficiency and scuffing resistance under demanding conditions. The study reveals that the MoS₂/Ti coating exhibits high hardness (~1200 kg/mm²), excellent adhesion, and a low friction coefficient (0.04–0.045 at high load), with moderate wear rates. Gear efficiency tests using an FZG test rig and biodegradable ester lubricant show that coated gears operate at lower stabilised temperatures and experience less frictional power losses than uncoated gears. Although the coated gears display slightly higher total wear volume, the MoS₂/Ti coating significantly increases scuffing load capacity, by up to five FZG load stages at high speed, translating to a 190% increase in transmitted power. The results demonstrate that MoS₂/Ti coatings not only lower friction and operating temperature but also greatly enhance the anti-scuffing performance of gears, making them promising for high-load, environmentally conscious gear applications.
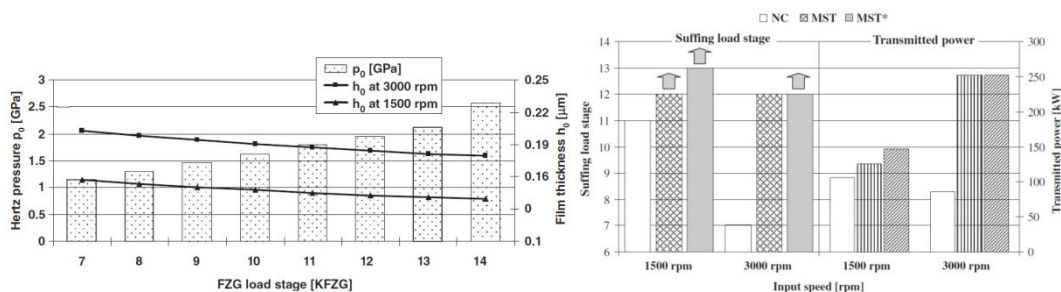
Figure. 2.12: Hertzian contact pressure and film thickness at wheel tip/pinion root contact point (left); FZG scuffing load stage and corresponding transmitted power in gear scuffing tests (right) [28]

He et al. (2010) [26] examine the tribological behaviour and efficiency of SCM420 gears coated with MoS₂-based Ti composite films. Ball-on-disc tribometry demonstrates that these composite coatings exhibit lower and more stable friction coefficients (decreasing from 0.08 to 0.047 as load increases from 2 N to 8 N) and improved lubricating performance at higher speeds, with lifetimes decreasing slightly under higher loads. Scratch tests confirm significantly improved adhesion for the composite coatings compared to pure MoS₂. Gear

efficiency tests under oil-absorption conditions show that MoS$_2$-based Ti-coated gears achieve 2.7–3.1% higher efficiency than uncoated gears across various speeds. This is attributed to reduced friction losses due to the solid lubrication effect. The study concludes that MoS$_2$-based Ti composite coatings are highly effective under conditions of frequent start-up or limited lubrication.
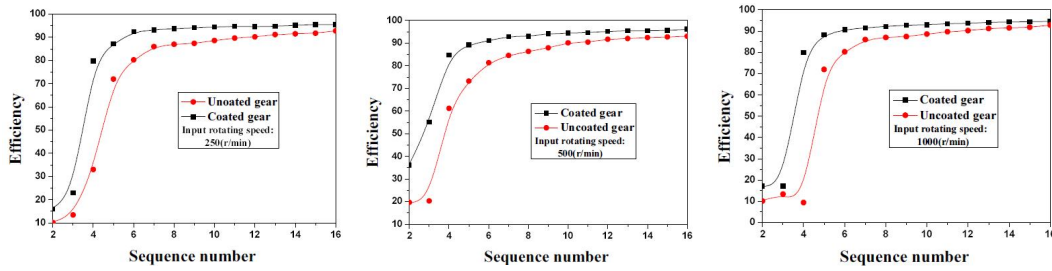
Figure. 2.13: Comparison of gear efficiency of coated and uncoated gears at an input rotating speed of 250, 500, 1000 rpm [29]
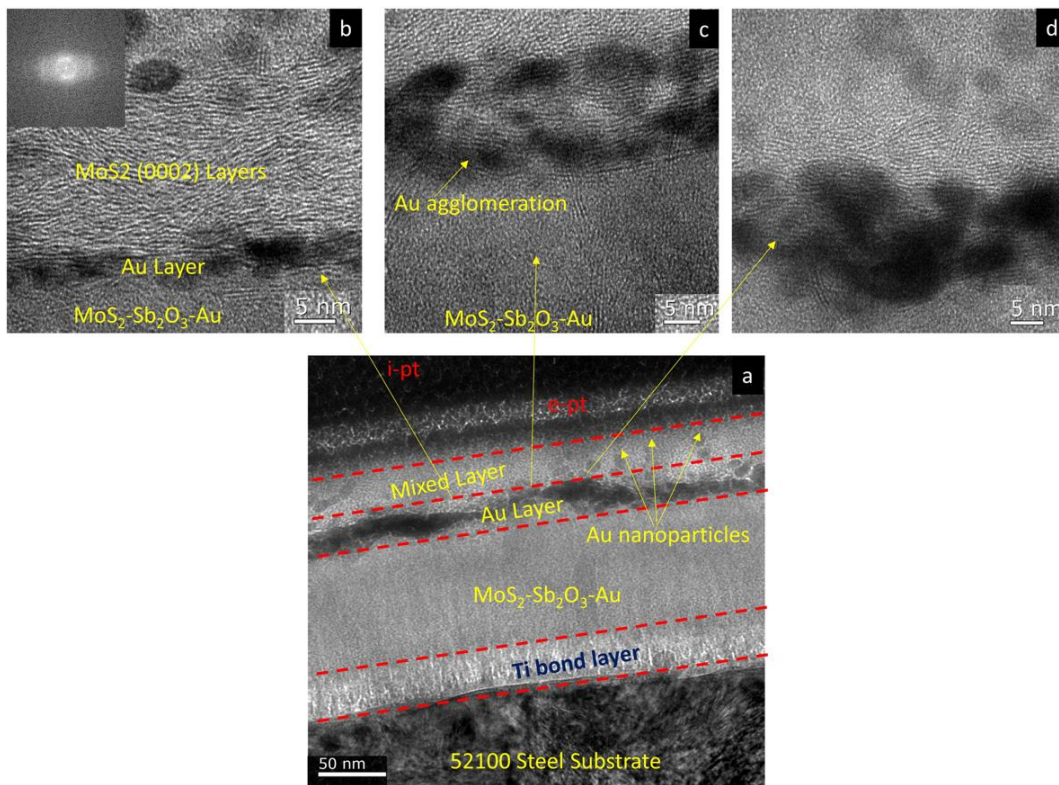
Figure. 2.14: HRTEM image of HFRR tested wear track of Au/Sb$_2$O$_3$-doped MoS$_2$ at 0.8 GPa and 15%–20 % RH; (b), (c), (d) higher-magnification images of the top surface showing the Au agglomeration and 2H-MoS$_2$ basal layers [30].

Singh et al. (2015) [30] investigate Sb$_2$O$_3$/Au-doped MoS$_2$ solid lubricant films focusing on their performance under sliding and rolling contact in various

environments. The study finds that doping enhances coating hardness, density, oxidation resistance, and adhesion compared to pure MoS_2, achieves low friction coefficients (as low as ~0.04 in vacuum) and maintains good wear resistance, though friction increases in humid air due to tribo-oxidation. Under sliding, shear-induced crystallisation and basal plane orientation of MoS_2 are observed, contributing to reduced friction, while Au nanoparticles agglomerate near the surface, supporting the reorientation process. Rolling contact tests in thrust ball bearings show that the coating's longevity is directly related to load and coating thickness, but also indicate that sliding test results do not directly predict rolling contact performance.

Table 2.3: Summary of Literature Survey

Author	Coating Material	Substrate Specification	CoF Obtained	Wear Rate	Key Findings
Holinski & Gänsheimer (1972) [8]	MoS_2 powder	Steel	0.05–0.1	N/A	Basal planes align parallel to the substrate during run-in, forming a protective film; slip occurs on the basal plane only.
Buck (1983) [2], [20]	MoS_2	Bearing raceway, various	N/A	N/A	Lamellae orientation and size are controlled by sputtering parameters; parallel orientation lowers friction.

Renevier et al. (1999) [20]	MoST (MoS$_2$/Ti composite)	Industrial tools (e.g., AISI D2)	0.02–0.04	~10^{-17} m³/Nm	Outperforms TiN in dry machining, extends tool life and productivity in cutting/forming operations.
Renevier et al. (2000) [22]	MoS$_2$/metal composite (Ti, Cr, W, Zr) (MoST)	Cutting tools, automotive	0.02–0.04	~10^{-17} m³/Nm	Metal additions increase hardness, adhesion, wear resistance, and amorphous/ fine-crystalline structure.
Teer (2001) [21]	MoST™, Graphit-iC™ (MoS$_2$/graphite)	Engine components, gears	0.02–0.07	N/A	Metal addition causes a decrease and an increase in the hardness of the Graphit-iC and MoST, respectively.
Arslan et al. (2004)[4]	Ti-doped MoS$_2$ (16.6 at%)	AISI D2 tool steel	0.06	1.02–5.51×10^{-6} mm³/Nm	The highest N$_S$/N$_{Mo}$ (1.59) ratio was reached with the lowest bias (−30 V) and highest working pressure (0.40 Pa).
Amaro	MoS$_2$/Ti	M42	N/A	Mild	Coating increases

et al. (2005) [27]		polished 1200 SiC steel		progressive wear	scuffing resistance (2–5 FZG stages), enables higher transmitted power, and improves efficiency.
Martins et al. (2006) [28]	MoS$_2$/Ti multilayer composite	M42 polished 1200 SiC steel	0.04– 0.045	Produce more wear volume than uncoated gears.	Reduced coefficient of friction between gear teeth supports a significant reduction in operating temperature and increased scuffing load capacity.
Wang et al. (2007) [23]	MoST (MoS$_2$/Ti, 15–19.5 at% Ti)	AISI M42 tool steel, Silicon substrates	0.1–0.15	4.7×10^{-18} m^{3}N^{-1}m^{-1}	Ti increases hardness and adhesion, produces amorphous/nanocrystalline composite, and improves wear resistance.
He et al. (2010) [29]	MoS$_2$-based Ti composite	SCM420 steel gears	0.047– 0.08	N/A	Friction coefficients are higher in air than vacuum, which could be attributed

					to oxidation of component coatings evaluated in ambient air.
Singh et al. (2015) [24]	Ti-doped MoS$_2$ (~16 at%)	AISI 52100 and M50 bearings	0.06	1.14 x 10^6 mm^3/Nm	Ti-MoS$_2$ films should be used on raceways and rolling elements to delay the start of adhesive wear.
Singh et al. (2015) [30]	Sb$_2$O$_3$/Au-doped MoS$_2$ and Ti	AISI 52100 steel ball bearings	0.04 (vacuum), 0.062 (Nitrogen),0.14 (air)	N/A	The coating's capacity to act as a solid lubricant in bearings scales inversely with load and depends on the amount of coating on the raceway. Bearing torque also increases with load.
Kong et al. (2020) [25]	MoS$_2$/Ti–MoS$_2$/Si multilayer	Polished stainless steel (304), Silicon wafer (100)	~0.043	3.22×10^{-7} mm^3/Nm	Doped elements mainly exist in amorphous and nanocrystalline phases in the composite coatings, reducing wear by 50%, and

					robust transfer films.
Feng et al. (2021) [26]	Ti, MoS$_2$	Plasma-nitrided CF170 steel	0.005–0.10	1.5×10^{-7} mm³/Nm	Increased hardness after plasma nitriding can enhance the resilience to deformation of the film, adhesive and abrasive wear.

Despite these advances, challenges remain in translating laboratory findings to complex, real-world surfaces and ensuring coating durability under varying environmental and mechanical stresses. Recent studies continue to address these issues by exploring novel composite architectures, duplex treatments, and optimised deposition strategies to achieve robust, uniform, and application-specific solid lubricant films. Collectively, the reviewed literature establishes a comprehensive foundation for ongoing research into MoS$_2$-based coatings, justifying the need for further investigation into their morphological optimisation and tribological performance for next-generation engineering systems.

2.2 Literature Gap

Despite extensive research on MoS$_2$-based solid lubricant coatings and various approaches to improve their tribological performance, several key gaps remain. Most existing studies focus on either pure MoS$_2$ or simple doped systems, with limited exploration of multilayer architectures like MoS$_2$-Ti designed for complex, high-stress applications like missile actuators.

● There is a scarcity of direct comparisons between MoS$_2$ and other transition metal dichalcogenides (TMDs) like WS$_2$ for similar applications.

- Few investigations on coating uniformity, adhesion, and performance on different substrate materials and complex geometries relevant to actuator components.

- Inadequate correlation between microstructure, phase composition, and tribological properties under practical load and environment.

2.3 Objectives of the Present Work

- Optimise sputtering parameters for MoS_2-Ti coatings on steels used in missile applications (e.g., Custom 465, 17-4 PH).

- Achieve and maintain optimum stoichiometry throughout the coating.

- Determine and control the optimum coating thickness for enhanced performance.

- Obtain uniform coating thickness and strong adhesion on flat and curved substrates.

- Achieve a low coefficient of friction and high wear resistance suitable for actuator duty cycles.

- Compare the tribological performance of the same coating on different substrate materials.

- Provide a comprehensive understanding of the relationship between processing, structure, and functional properties for advanced solid lubricant coatings.

Chapter 3

Methodology

3.1 Material Selection

17-4PH stainless steel, also known as Type 630, is a martensitic precipitation-hardening alloy renowned for its exceptional high strength, corrosion resistance, and thermal stability, making it ideal for missile applications. Emerging in the 1940s, 17-4 stainless steel was engineered to address industrial demands for materials capable of enduring extreme mechanical stress without compromising corrosion resistance. As aerospace, defence, and marine industries advanced, the need intensified for alloys that merged exceptional strength with fracture toughness. Precipitation-hardening stainless steels, exemplified by 17-4PH, bridged this critical need by offering a novel solution: heat-treatable hardening for enhanced strength paired with retained corrosion resistance, even in aggressive environments like chemical processing or marine systems.
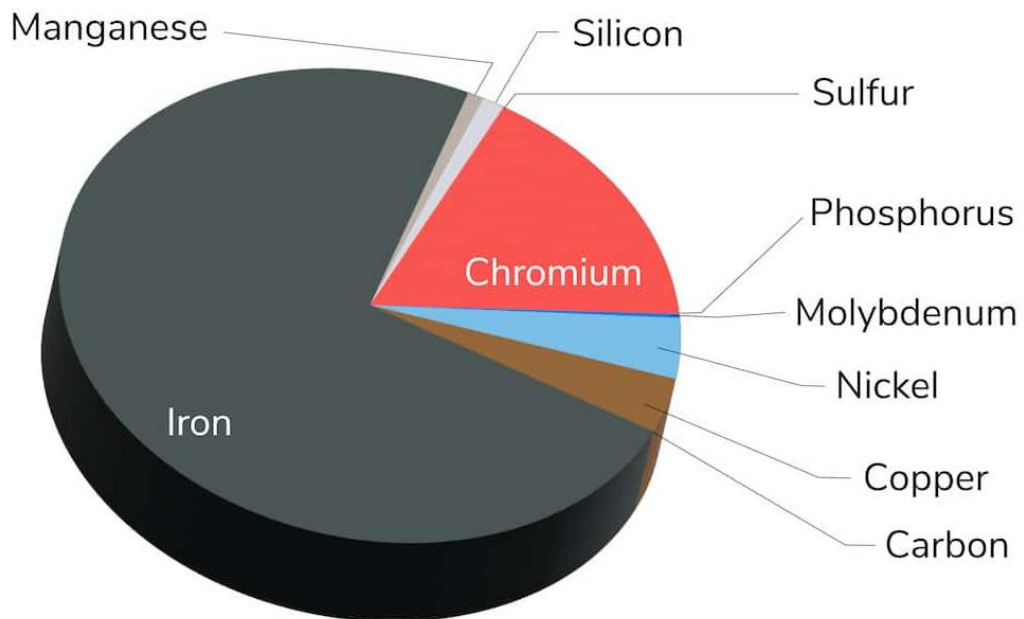
Figure 3.1: Metals used to produce 17-4 PH stainless steel [31]

Over the decades, 17- 4PH has solidified its status as an industry standard for high-stress applications. Composed of 15–17.5% chromium, 3–5% nickel, and 3–5% copper, its versatility stems from the ability to fine-tune mechanical properties, such as tensile strength (up to 1,300 MPa) and hardness (up to 44 HRC), through tailored ageing treatments. The alloy exhibits excellent corrosion

resistance, surpassing standard hardenable stainless steels, particularly in aggressive environments involving chemicals or moisture. This is vital for missile systems exposed to harsh operational conditions, including seawater or atmospheric corrosion. Thermally, 17- 4PH maintains mechanical stability up to 316°C (600°F), with a low thermal expansion coefficient (10.8–11.2 μm/m·°C) and moderate thermal conductivity (17.9–22.6 W/m·K), ensuring dimensional integrity during rapid temperature fluctuations16. Its 7.75 g/cm³ density offers a favourable strength-to-weight ratio for aerospace applications.

This base material's adaptability, combined with weldability and machinability, has made it indispensable in aircraft components, turbine blades, and missile guidance systems, and its ability to retain coatings under dynamic loads makes it a robust substrate for tribological applications in actuator mechanisms and other precision missile components. Its precipitation-hardening process allows precise tuning of mechanical characteristics through ageing treatments, providing flexibility for tailored performance in critical components. The alloy's enduring relevance underscores its unique balance of performance attributes, cementing its role as a cornerstone material in modern engineering.

Table 3.1: Advantages and limitations of using 17-4 PH stainless steel

Advantages	Limitations
Exceptional Mechanical Strength Achieves tensile strengths up to 1,300 MPa and yield strengths of 1,100–1,300 MPa through precipitation hardening, ideal for high-stress applications like aerospace components.	**Limited Corrosion Resistance in Harsh Environments** Susceptible to crevice corrosion, pitting, and chloride stress cracking in seawater or acidic conditions, it is outperformed by 316 stainless steel in such environments.
Balanced Corrosion Resistance Compared to 304 stainless steel in freshwater, mild chemicals, and atmospheric conditions, it is suitable	**Brittleness at Peak Strength** Higher strength conditions (e.g., H900) reduce ductility, increasing fracture risk under impact loads.

for food processing and industrial applications.	
Tailorable Properties via Heat Treatment Mechanical properties (e.g., hardness, toughness) can be optimised through ageing treatments (480–760°C), enabling customisation for specific operational demands.	**Higher Cost** More expensive than standard grades (304/316) due to alloying elements (Cr, Ni, Cu) and specialised heat treatments.
High Toughness Retention It maintains good impact resistance in H900 conditions and is critical for structural components like turbine blades and fasteners.	**Welding Sensitivity** Overheating during welding risks forming brittle phases, requiring precise temperature control and post-weld ageing.
Fabrication Flexibility Easily machined, welded (GTAW/SMAW), and cold-formed in solution-annealed state, simplifying pre-hardening manufacturing.	

3.2 Sample Preparation

The sample preparation process for tribological testing of 17- 4PH steel substrates began with a 160 mm diameter × 100 mm length ingot. Using in-house wire-cut electrical discharge machining (EDM), cylindrical discs of 50 mm diameter × 5 mm thickness were initially sectioned. However, challenges arose in accurately measuring coating thickness uniformity across the disc surface due to curvature-induced measurement errors. The discs were further subdivided into 30° sectors via wire EDM to address this, providing flat, geometrically consistent specimens. Despite this adjustment, polishing the curved edges of the sectors to a mirror finish for microstructural characterisation proved problematic,

prompting a final redesign into 1 mm × 1 mm × 1 mm cubes. With its ±0.01 mm precision and minimal thermal distortion, the wire EDM process ensured dimensional accuracy while preserving the material's inherent properties.

Figure 3.2: Wire EDM setup and operation: (top) CNC wire EDM machine used for precision machining; (bottom left) close-up of wire cutting multiple cylindrical samples; (bottom right) control panel and real-time display of the circular cutting path during machining.

Complementary "bullet-shaped" pins were machined from the same 17-4PH steel stock for pin-on-disc experiments. These pins, measuring 30 mm long with a 6 mm radius hemispherical tip, were produced using CNC machining to achieve the required curvature and surface finish (Ra ≤ 0.4 μm). The hemispherical geometry ensures consistent contact pressure during wear testing, simulating

point-contact conditions prevalent in missile guidance systems and actuation mechanisms. Post-machining, all specimens underwent ultrasonic cleaning in acetone and isopropyl alcohol to remove residual lubricants or debris from fabrication.

This multi-stage approach balances manufacturing practicality with analytical requirements, ensuring reliable data acquisition for coating performance validation in missile-relevant operational scenarios.

3.3 PVD Magnetron Sputtering

3.3.1 Sputtering machine

The PVD magnetron sputter coating system manufactured by Mansha Vacuum Equipments, Bangalore, represents an indigenous solution for thin-film deposition of transition metal dichalcogenide (TMD) solid lubricants. The system features a dual magnetron configuration with 2-inch target holders, though it is designed for single-target operation at any given time. This versatile system accommodates multiple deposition modes, including DC, RF, and Pulsed DC sputtering, enabling precise control over coating morphology and composition.
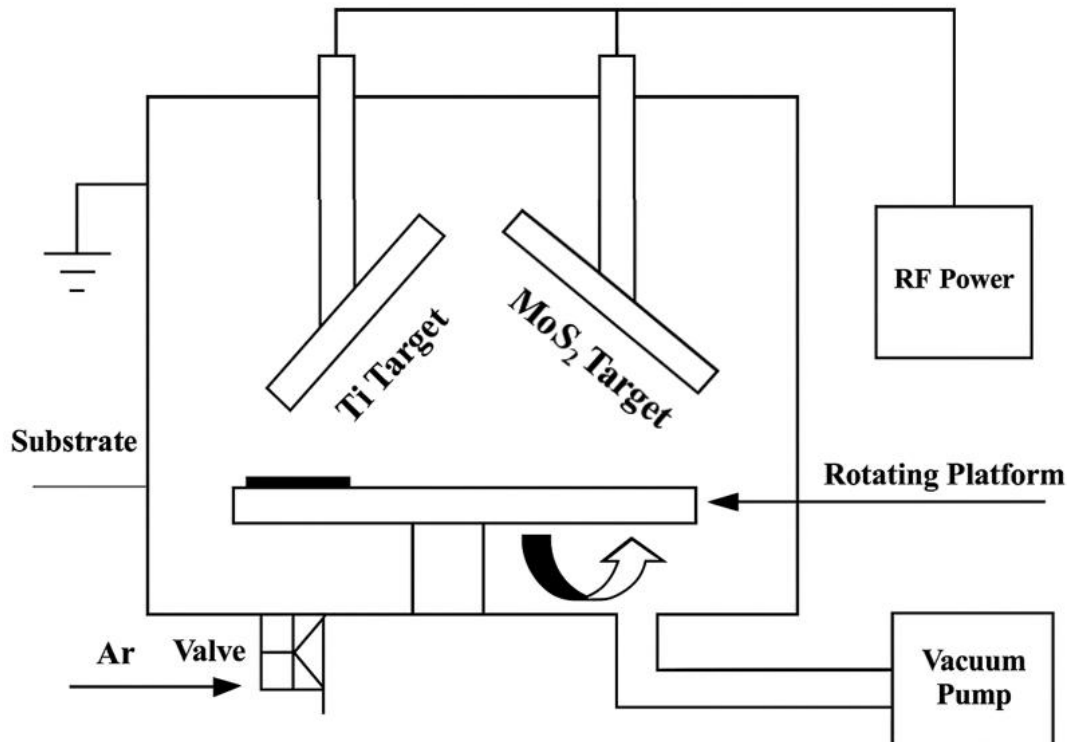
Figure 3.3: Schematic of magnetron sputtering system used in this study for co-deposition: Ti and

MoS$_2$ targets are tilted at certain angles toward the substrate.

The vacuum chamber achieves base pressures of 10^{-6} mbar through the sequential operation of a rotary backing pump and a turbomolecular pump, essential for minimising contaminants that compromise coating integrity. The system's pneumatic valves operate using N$_2$ gas, while high-purity argon (99.999%) is the primary sputtering medium with flow rates precisely regulated between 5-100 sccm via mass flow controllers.

The sputtering process relies on momentum transfer, where energetic argon ions bombard the target material, ejecting atoms that subsequently deposit onto the substrate. This physical vapour deposition technique produces exceptionally adherent coatings with precisely controlled thickness and composition. For optimal process stability, the system implements real-time parameter control, with the pulsed DC mode typically operating at frequencies between 20-350 kHz and duty cycles of 0.5-0.9 to prevent microarcs that would otherwise compromise coating quality. Power delivery ranges from 50- 1000W, allowing deposition rates between 0.1-2.0 μm/min depending on target material and process parameters.

Figure 3.4: PVD sputter coating system used for thin film deposition, showing the main vacuum

chamber, control panel with power and process controls.

Critical to successful deposition is the integrated water cooling system that maintains magnetron temperature below 30°C during extended operation, preventing thermal damage to the targets and ensuring consistent deposition rates. The closed-loop chiller circulates deionised water through the magnetron assembly, stabilising process conditions even during prolonged high-power operation. For tribological applications, the system accommodates various target materials, including transition metals (Mo, Cr, W, Ti) and their compounds, with target purity typically exceeding 99.95% to ensure optimal coating performance in missile components subject to extreme mechanical stresses.

The sputter chamber features multiple ports for in-situ process monitoring, including a quartz crystal microbalance for real-time thickness measurement and viewports for plasma observation. For TMD coatings specifically, the system achieves optimal results using an argon working pressure of 3-5 mbar, with substrate temperatures maintained at ambient to control coating crystallinity and adherence to the 17- 4PH steel substrates. This indigenous system delivers coating performance comparable to imported alternatives while offering flexibility for process development and optimisation tailored to specific missile tribological applications

3.3.2 Sputtering Targets

The research employed high-purity sputtering targets sourced from PhotonExport (Barcelona, Spain) to develop TMD-based solid lubrication coatings. A molybdenum disulfide (MoS_2) target with 99.99% purity and a titanium (Ti) target were selected, featuring identical dimensions of 50.8 mm diameter × 3 mm thickness, compatible with Mansha Vacuum Equipment's magnetron configuration. These circular targets were chosen for their exceptional uniformity in grain structure and minimal impurity content, which are critical factors for achieving homogeneous coating deposition with consistent tribological properties. The MoS_2 target with copper back plate, appearing black with a matte finish, was specifically selected for its lamellar crystal structure that facilitates the formation of low-friction coatings. In contrast, the metallic titanium target exhibited a silvery finish with concentric machining patterns typical of high-quality PVD-grade targets.

Before deposition, comprehensive target characterisation was conducted to verify material composition and purity. X-ray fluorescence (XRF) spectroscopy and SEM-EDS (Scanning Electron Microscopy with Energy Dispersive X-ray

Figure 3.5: Front and back views of a MoS$_2$ sputtering target bonded to a copper backing plate (left and centre), and a pure titanium (Ti) sputtering target (right), both used for thin film deposition in PVD processes.

Spectroscopy) confirmed the elemental composition of both targets, with the MoS$_2$ target demonstrating the stoichiometric 1:2 ratio of molybdenum to sulfur. Further validated the targets' surface morphology and microstructural characteristics, while the MoS$_2$ target displayed the characteristic layered microstructure essential for its solid lubricant properties. The analysis confirmed that both targets met the high-performance thin film deposition specifications.

The targets were maintained in vacuum-sealed packaging until immediately before installation in the sputtering system to prevent surface oxidation or contamination. Both targets demonstrated excellent plasma stability and consistent deposition rates during preliminary testing. This careful selection and characterisation of the sputtering targets ensured reproducible coating quality and adherence to the 17- 4PH steel substrates, laying a strong foundation for subsequent tribological performance testing in simulated missile application environments.

3.3.3 Fishbone (Ishikawa) diagram of sputtering parameters involved

The fishbone diagram presents a comprehensive framework for optimising the complex interdependencies of sputtering parameters in TMD-based solid lubrication coating development. This systematic classification organises critical

variables that determine coating adhesion, homogeneity, and tribological performance into four major categories: target material characteristics, substrate properties, sputtering gas attributes, and deposition process parameters. The challenge in developing indigenous TMD coatings lies in identifying the optimal combination of these parameters, as they collectively influence film microstructure, crystallinity, and ultimately, the mechanical and tribological properties. Each parameter operates within a complex interrelationship where modification of one variable necessitates compensatory adjustments across multiple others to maintain coating integrity.

Target material parameters fundamentally determine coating composition and deposition efficiency. Target purity (>99.9% for MoS_2 and Ti) directly influences coating contamination levels, while target shape and size affect plasma distribution and deposition uniformity. Concurrently, substrate properties significantly impact coating adhesion and growth morphology. Surface roughness modulates nucleation site density and mechanical interlocking, while pre-cleaning procedures remove surface contaminants that would otherwise compromise coating adhesion. The substrate's thermal conductivity influences heat dissipation during deposition, affecting the coating's crystallisation behaviour and residual stress development.
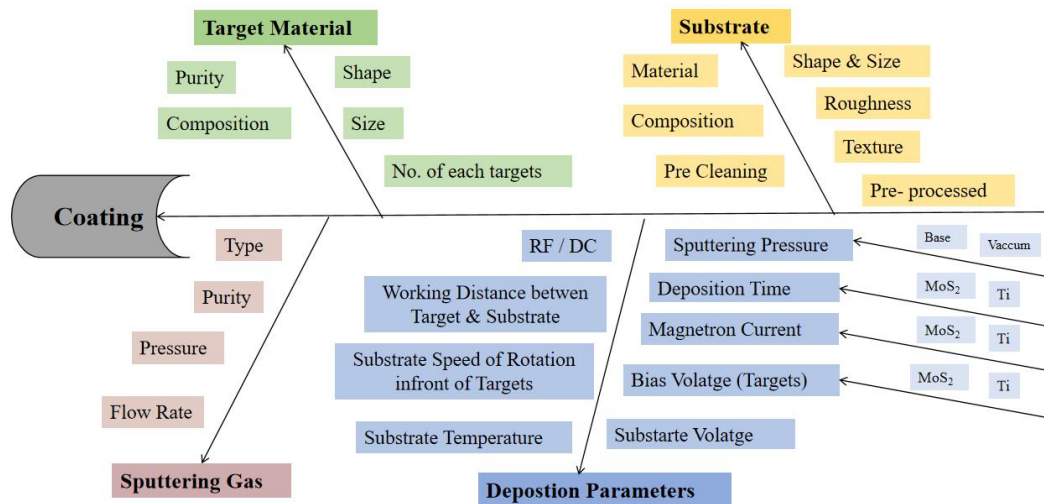
Figure 3.6: Fishbone (Ishikawa) diagram illustrating the key parameters influencing the sputtering process for thin film coatings.

Sputtering gas parameters control plasma characteristics and momentum transfer efficiency during deposition. Gas purity prevents the incorporation of contaminants, while flow rate and pressure regulate the mean free path of

43

sputtered atoms. Higher pressures increase collision frequency, resulting in thermalised deposition with improved step coverage but potentially reduced adhesion. Conversely, lower pressures promote ballistic transport of high-energy atoms, enhancing film density and adhesion but potentially creating shadowing effects. For MoS_2 deposition, optimising argon pressure is particularly critical as it affects the stoichiometry and crystal orientation of the resultant film.

The deposition process parameters provide precise control over coating microstructure and properties. The working distance between target and substrate affects deposition rate and uniformity, with shorter distances increasing the rate but potentially reducing uniformity. Substrate temperature critically influences adatom mobility and crystallisation; for MoS_2 coatings, temperatures between ambient and 200°C determine whether the film forms with edge-oriented or basal-oriented crystal planes, directly affecting friction coefficients. Magnetron current and bias voltage control ion bombardment energy and deposition rate, with increased power generally improving film density but potentially inducing higher residual stresses that compromise coating durability.

The systematic optimisation of these interdependent parameters through controlled experimentation enables the development of indigenous TMD coatings with performance characteristics tailored specifically for missile tribological applications.

3.3.4 Process Flow of Sputtering Experiments

Sputtering begins with meticulous substrate preparation to ensure optimal coating adhesion and performance. As shown in the process flow images, the 17-4PH steel substrates (polished discs and cube samples) undergo surface preparation starting with mechanical polishing to achieve the required surface finish and roughness parameters. This critical first step establishes the foundation for coating adhesion by providing a uniform surface with controlled topography.

1. Polish   2. Ultrasonic Cleaning   3. Chamber Cleaning   4. Taping & Loading

Figure 3.7: Stepwise substrate preparation for sputter coating: (1) mechanical polishing of discs and cubes, (2) ultrasonic cleaning to remove surface contaminants, (3) chamber cleaning before deposition, and (4) taping and loading of samples for coating.

Following polishing, the samples are subjected to ultrasonic cleaning in a bath containing solvents like acetone and isopropyl alcohol to remove organic contaminants, machining oils, and particulate matter that would otherwise compromise coating integrity. These preparatory steps are essential for establishing the optimal substrate surface condition before introducing the samples into the vacuum environment.

The second phase involves systematic vacuum system preparation following a precise protocol to achieve the ultra-high vacuum conditions necessary for high-quality film deposition. The process begins by activating the rough vacuum valve to initiate preliminary evacuation of the chamber until reaching a pressure below 5×10^{-2} mbar, as indicated on the system's digital pressure display. Once this initial vacuum level is achieved, the rough valve is closed and the backing valve opened to establish a proper backing line for the turbomolecular pump, which is then activated. The system continues evacuation until the turbo pump reaches its normal operating parameters, significantly reducing the chamber pressure to the 10^{-4} mbar range. Finally, the high vacuum valve is opened to achieve the ultimate base pressure below 5×10^{-5} mbar, creating an environment with minimal contaminants for high-purity coating deposition.

Figure 3.8: Sequential display of vacuum chamber evacuation steps for sputtering: (left) achieving sub-5×10^{-2} mbar with roughing pump; (center) switching to turbo pump and reaching 1.8×10^{-4} mbar; (right) opening high vacuum valve to attain base pressure of 4.8×10^{-5} mbar, with corresponding valve positions and control panel readings at each stage.

The system transitions to the process gas introduction and peripheral system activation phase with the ultra-high vacuum established. The operator closes all

valves momentarily before reopening the rough valve and activating the mass flow controller (MFC) to regulate argon gas into the chamber precisely. High-purity argon (99.999%) is supplied at a pressure of 4-5 bar through the gas inlet system, with flow rates carefully controlled to establish the optimal working pressure for sputtering. Concurrently, the water chiller system is activated to verify the cooling circuit necessary for thermal management of the magnetron assembly during the high-power deposition process. This temperature regulation is critical for maintaining target integrity and preventing thermal damage during extended operation.

The final phase involves power system activation and plasma generation for the deposition process. The RF power supply and matching network (shown in the AIT-600 RF Auto Tuner) are energised to deliver precisely controlled power to the magnetron containing either the MoS_2 or Ti target. The matching network automatically optimises the circuit impedance to minimise reflected power, ensuring efficient energy transfer to the plasma. This creates a stable glow discharge that ionises the argon gas, producing high-energy ions that bombard the target surface and eject target atoms through momentum transfer. These sputtered atoms traverse the vacuum space to condense on the prepared 17- 4PH steel substrates, forming the TMD-based solid lubrication coating with controlled thickness and composition. Throughout this process, multiple system parameters, including pressure, power, and gas flow, are continuously monitored and adjusted to maintain optimal deposition conditions for the desired coating properties.

Figure 3.9: Sputtering system operation sequence: (left) Valve and gas flow control panel,

vacuum gauge, and turbo pump display showing chamber pressure at 1.4×10^{-1} mbar after evacuation and argon gas introduction; (right) RF power supply and auto tuner interface used to initiate plasma generation for thin film deposition, following system preparation steps.

To achieve an optimised PVD multilayer coating of Ti and MoS_2, we initially focused on individually optimising the deposition parameters for each layer. This involved carefully adjusting variables such as target power, substrate to target distance, and deposition time to achieve desired film properties. Subsequently, we employed a sequential deposition process, where the optimised parameters for each layer were applied in succession. This approach allowed us to create a well-defined and robust multilayer coating, combining the beneficial properties of both Ti and MoS_2.

3.4 SEM-EDS

Scanning Electron Microscopy (SEM) combined with Energy Dispersive X-ray Spectroscopy (EDS) was extensively employed in this study to characterise the TMD-based coatings' surface morphology and elemental composition. Two SEM systems were utilised: a Zeiss EVO 10 instrument, primarily for EDS analysis, and a JEOL system, optimised for high-resolution imaging. The Zeiss SEM, equipped with advanced EDS capabilities, enabled rapid and spatially resolved elemental mapping, area scans, and line scans, which are essential for verifying the presence and stoichiometry of the deposited coatings. After each sputtering run, EDS analysis was performed on the substrate's coated and uncoated (taped) regions. By comparing these regions using area and line scans, the uniformity and elemental composition of the coatings were systematically evaluated, ensuring that the desired stoichiometry, such as the Mo:S ratio in MoS_2-was consistently achieved.

The JEOL SEM was primarily used for detailed imaging of the coating's surface and cross-sectional morphology. High-resolution SEM imaging allowed for assessing coating thickness, grain structure, and surface features at magnifications far exceeding those of conventional optical microscopy. Silicon wafers were coated alongside the 17- 4PH substrates in each sputtering run to accurately measure the coating thickness. After deposition, these wafers were fractured to expose a clean cross-section, which was imaged in the SEM. This approach provided precise measurements of the coating thickness. It enabled

examination of the interface quality between the coating and the substrate, which is critical for understanding adhesion and wear performance.
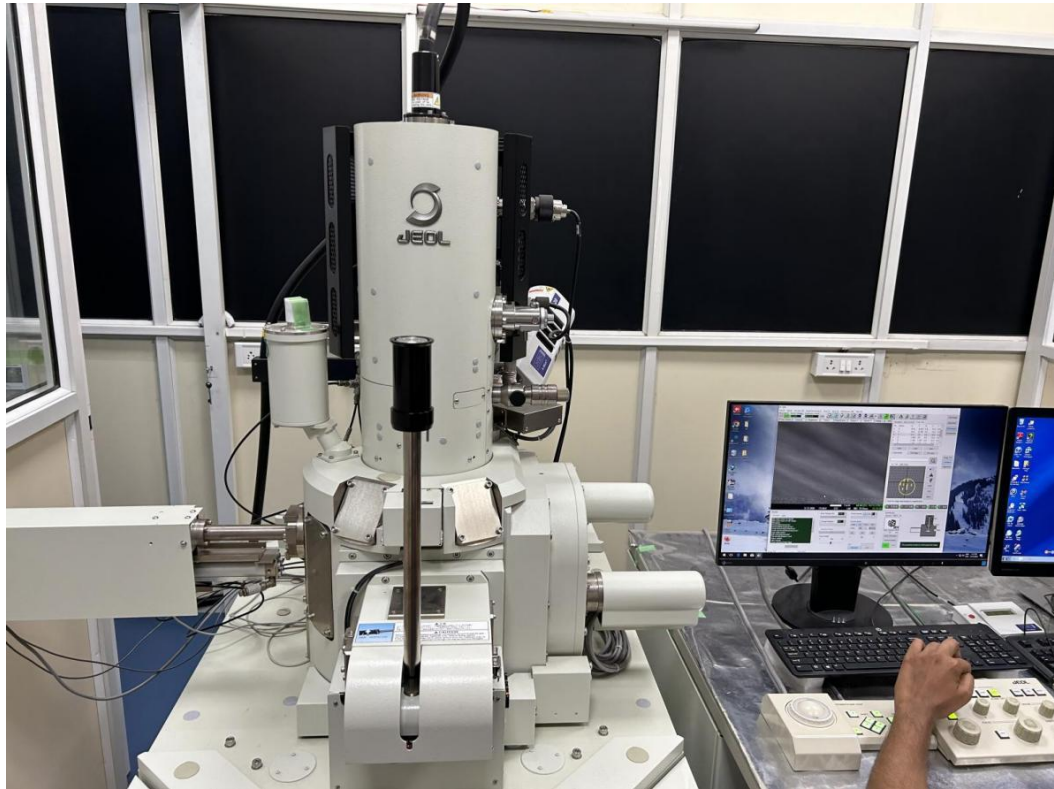
Figure 3.10: Laboratory scanning electron microscopes used for coating characterisation: (top) ZEISS EVO 10 SEM with integrated control workstation; (bottom) JEOL SEM system with high-resolution imaging capabilities, both employed for detailed surface and cross-sectional analysis of thin film coatings.

The combined use of SEM and EDS provided a comprehensive characterisation protocol for the coatings. SEM-EDS analysis confirmed the presence and uniformity of the TMD coatings and enabled quantitative assessment of elemental composition and detection of any contaminants or compositional gradients across the film. This dual-instrument strategy ensured that both the microstructural and compositional requirements for high-performance solid lubrication coatings were rigorously validated, supporting the reliability and reproducibility of the developed coating process for missile application environments.

3.5 X-ray Diffraction analysis

X-ray diffraction (XRD) analysis was performed to determine the crystalline phases in the coated samples. The XRD measurements were carried out using a PANalytical Empyrean diffractometer (Figure 3.11), operating at 45 kV, with a 2θ scan range from 5° to 90°. Initial scans were conducted on the MoS$_2$ target and the uncoated 17- 4PH steel substrate to establish baseline diffraction patterns and facilitate comparison with the coated samples.
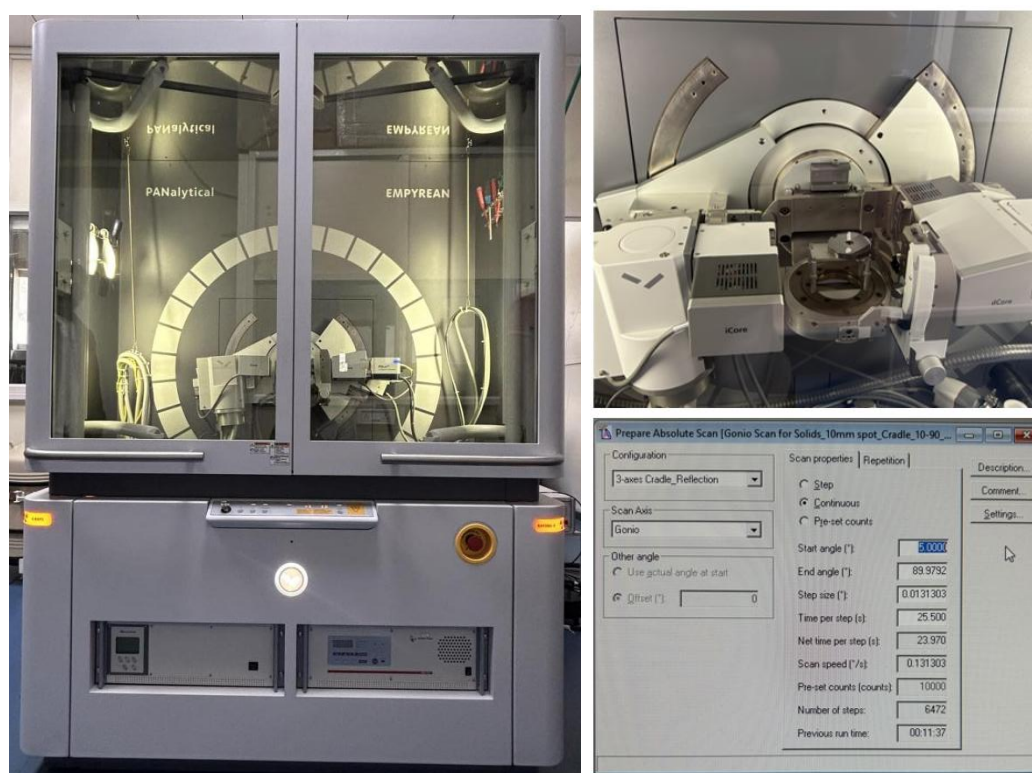
Figure 3.11: X-ray diffraction (XRD) instrument setup for phase analysis: (left) PANalytical Empyrean diffractometer system; (top right) close-up of sample stage and goniometer assembly inside the chamber; (bottom right) software interface displaying scan parameters for automated

XRD measurement.

For coated samples, regular XRD scans were performed on both MoS_2 and MoS_2+Ti coatings deposited on steel and glass substrates, using identical parameters (2θ range: 5–90°, voltage: 45 kV). To further investigate phase formation and crystallinity, additional scans were carried out on MoS_2+Ti coatings at different tube voltages (35, 40, and 45 kV) to assess the effect of X-ray energy on peak intensity and resolution. In cases where characteristic MoS_2 peaks, especially the (002) reflection, were weak or absent in regular incidence scans, Grazing Incidence X-ray Diffraction (GI-XRD) was employed. GI-XRD scans were performed at various incident angles ($\omega = 0.5°$, 1°, 1.5°, and 2°) to enhance surface sensitivity and selectively probe the thin film region, minimising substrate interference and enabling the detection of weakly oriented or low-intensity surface phases. This approach is efficient for thin or nanocrystalline films, where conventional XRD may not provide sufficient signal due to limited diffracting volume.

All XRD data were analysed using the X'Pert HighScore software suite, facilitating automated peak identification, baseline correction, and phase matching against standard JCPDS reference cards. The analysis enabled precise determination of phase purity, crystallite orientation, and the presence of secondary phases or impurities. For the MoS_2-coated samples, the presence and intensity of the (002) peak were rigorously evaluated, as this reflection is indicative of basal-plane alignment parallel to the substrate, a key requirement for achieving low friction and adequate solid lubrication. The comparison of XRD patterns from coated and uncoated regions and between steel and glass substrates provided insights into the influence of substrate type and deposition parameters on film crystallinity and orientation.

This rigorous XRD characterisation and EDS and SEM analyses ensured that the structural requirements for high-performance solid lubrication coatings were met, supporting the reliability and reproducibility of the developed coating process for advanced tribological applications.

3.6 Raman Spectroscopy

Raman spectroscopy is a non-destructive analytical technique used to probe the vibrational, rotational, and other low-frequency modes of molecules, providing a

unique molecular fingerprint for material identification and characterization. In this study, Raman spectroscopy was employed to analyze the structural and phase composition of Ti-MoS$_2$ coatings. The technique relies on the inelastic scattering of monochromatic laser light (Raman scattering), where incident photons interact with the sample and are shifted in energy according to the vibrational modes of the constituent molecules. These energy shifts are detected and plotted as a Raman spectrum, with each peak corresponding to specific molecular bonds or lattice vibrations, enabling detailed insight into crystallinity, chemical structure, and the presence of secondary phases.

A Horiba Lab-Ram Micro-Raman spectrometer equipped with a 632 nm excitation wavelength was used for all Raman analyses of Ti-MoS$_2$ specimens (Figure 3.12). The system allows for high spatial resolution and sensitive detection of weak Raman signals, making it suitable for studying thin films and nanostructured materials. The obtained spectra were compared with reference liertature data to identify characteristic peaks of MoS$_2$, Ti-based compounds, and any oxide or amorphous phases, thus supporting conclusions drawn from XRD and complementing the overall microstructural characterization.

Figure 3.12. A Horiba Lab-Ram Micro-Raman spectrometer with an excitation wavelength of 632 nm was used for analyses of Ti-MoS$_2$ specimens

3.7 Tribological analysis

3.7.1 Ball/Pin-On-Disc Wear Testing

The pin-on-disc tribological experiments were conducted using a Ducom Instruments Pin on Disc Tribometer, a precision system widely adopted for benchmarking the friction and wear performance of advanced coatings and materials. The instrument features a rotary drive for disc rotation and a rigidly mounted loading arm to hold the pin specimen. This enables accurate application

of normal loads and consistent measurement of frictional forces throughout the test duration. The system is fully computer-controlled, allowing for precise input and real-time monitoring of all test parameters, including load, speed, track diameter, and test duration. The Ducom tribometer is compliant with ASTM G99 standards. It can accommodate a variety of pin and disc geometries, making it highly suitable for evaluating uncoated and coated 17-4PH steel substrates.
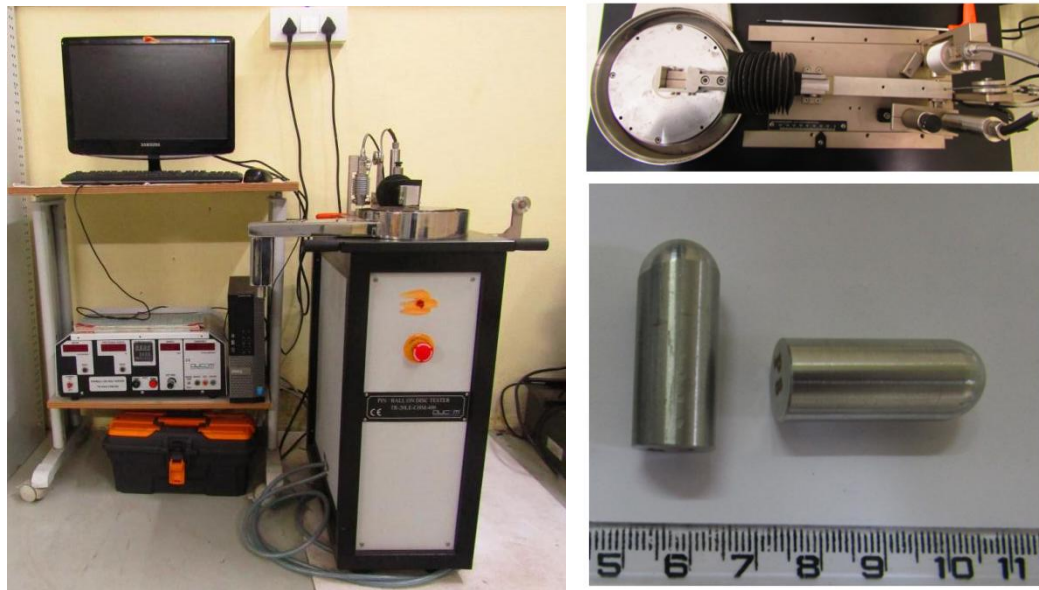
Figure 3.13: Ball/Pin-on-Disc wear tester setup: (left) complete tribometer system with control unit and computer interface; (top right) close-up of pin loaded against rotating disc for wear testing; (bottom right) cylindrical pin specimens used in the tests.

Table 3.2: Technical Specifications of Pin on Disc Tester

Pin Size	Φ 6,8,10,12
Specimen Holder	Split Jaws for Clamping
Wear Disc	Size : Φ165 mm x 8 mm thick, Material - EN31 (58-62 HRC)
Wear Track Dia	Min - 10 mm & Max - 135 mm
Disc Speed	Min - 200 rpm & Max - 2000 rpm
Normal Load	Min - 0.5 kg (5N) & Max - 20 kg (200N)
Frictional Force	0-200 N
Wear	0 - 2000 μm
Temperature	Ambient to 400 $^{\circ}$C

Table 3.3: Sensor Specifications of Pin on Disc Tester

Speed	Range: 200-2000 rpm
	Sensor - Proximity Sensor
	Least Count - 1 rpm
	Accuracy - 1 ± (1% of measured speed) in rpm
Frictional Force	Range - 200 N
	Sensor - Load Cell
	Least Count - 0.1 N
	Accuracy - 1 ± (1% of measured Frictional Force) in N
Wear	Range: 0 - 2000 rpm
	Sensor - Proximity Sensor
	Least Count - 1 rpm
	Accuracy - 1 ± (1% of measured wear) in μm
Normal Load	0.5 kg to 20 kg in steps of 0.5 kilograms, dead weights are provided to apply a normal load

For the experimental procedure, uncoated and TMD-coated samples were tested under identical conditions to ensure direct comparison of tribological performance. The tests were performed at a constant normal load of 5 N and a rotational speed of 60 rpm, with each test running for 120 seconds. The wear track diameters were systematically varied to ensure optimal utilisation of the entire EN31 wear disc and to provide a fresh wear track for each test. This approach allowed for consistent wear measurements while preventing overlap with previously worn regions, thereby minimising the influence of prior surface damage on subsequent experiments. These parameters were carefully selected to simulate realistic contact pressures encountered in actuator applications, supported by Hertzian contact stress calculations. The pin, machined from the same 17-4PH steel, was positioned perpendicularly to the disc surface, and the system's integrated sensors continuously recorded frictional force data. All tests were conducted in ambient laboratory conditions, and the system's automated data acquisition ensured high reproducibility and accuracy in measuring the coefficient of friction (CoF).

3.7.2 Hertzian Contact Stress Analysis for Tribological Testing

In pin-on-disc tribological testing, Hertzian contact mechanics [32] Provides the fundamental framework for determining stress distribution at the contact interface between two non-conforming bodies. The image presents the classical Hertzian equations. [33] That establishes the relationship between applied normal load (F) and resulting contact parameters for curved surfaces in elastic contact. These equations are crucial for experimental design as they precisely calculate the contact radius (a) and maximum compressive stress (σ_{max}) at the interface between the hemisphere-tipped pin and flat disc specimen. By incorporating material properties, including Young's modulus (E) and Poisson's ratio (v) for both contacting bodies, along with the pin tip radius, these formulations provide a comprehensive assessment of the stress field that directly influences wear mechanisms, friction behaviour, and coating durability in tribological systems.

From Herzberg's Contact theory [34],

Contact radius a, under force F:

$a = [3FR / 4E^*]^{1/3}$

where $E^* = E / 2(1 - v^2)$

Max^m compressive stress:

$\sigma_{max} = 3F / 2\pi a^2$

Stress at the contact area:

$\sigma = 0.6 [FE^2 / D^2]^{1/3}$
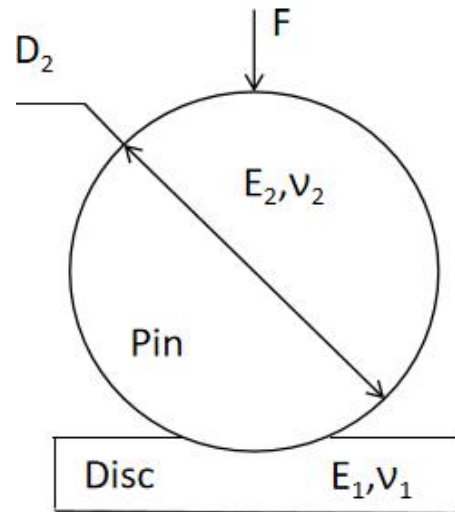
Figure 3.14: Schematic of pin-on-disc tribological testing

Table 3.4: Material and geometric properties of the pin and disc used in pin-on-disc testing.

	Disc	Pin
Nomenclature	1	2
Shape	Flat	Sphere
Poisson's ratio (v)	0.272	0.272
Young's modulus (E) (GPa)	200	197
Diameter (D) (mm)	-	12

The pin-on-disc configuration illustrated in the diagram incorporates precise geometric and material parameters that directly influence the contact mechanics. According to Hertzian theory, the hemisphere-tipped pin (with radius $D_2/2$) creates a point contact against the flat disc surface, which transforms into a circular contact patch under load. This contact geometry is particularly advantageous for evaluating solid lubrication coatings like TMD-based films, as it concentrates stress within a well-defined area while maintaining consistent contact conditions throughout extended sliding tests. The elastic properties of both bodies (E_1, v_1 for the disc; E_2, v_2 for the pin) contribute to the effective elastic modulus (E^*) used in the contact radius calculation, highlighting how material selection influences the resulting stress distribution even under identical loading conditions.

Table 3.5: Calculate contact stress at the pin-disc interface under varying applied loads during tribological testing.

Load (N)	Stress at contact area (MPa)
2.5	526
5	663
7.5	760
10	836

The tabulated calculations demonstrate the non-linear relationship between applied load and resulting contact stress, following the Hertzian prediction that stress increases proportionally to $F^{1/3}$. This mathematical relationship explains why doubling the load from 5N to 10N increases the contact stress by only 26% (from 663 MPa to 836 MPa). This non-linear behaviour is critical when designing tribological experiments, as it allows researchers to select appropriate test loads that generate stress conditions representative of actual mechanical components without requiring excessively high forces that might compromise test equipment or specimen integrity. The calculated stresses spanning 526-836 MPa across the 2.5- 10N load range strategically overlap with the typical contact pressure range (600-1000 MPa) experienced by actuator components in missile systems, validating the experimental approach and ensuring test relevance to real-world applications.

By methodically calculating the contact stresses across multiple load conditions, one can establish direct correlations between applied load, resulting contact stress, and observed tribological performance of the TMD-based solid lubrication coatings. This approach enables quantitative assessment of coating durability and friction characteristics under precisely controlled stress states that mirror operational conditions in missile actuator components. The progressive increase in contact stress with increasing load also facilitates the determination of critical threshold values where coating failure mechanisms transition from mild to severe wear, providing essential design parameters for optimising coating thickness and composition for specific mechanical applications. This scientific approach to load selection, grounded in Hertzian contact mechanics, ensures that laboratory tribological evaluations generate results directly relevant to field performance prediction.

Chapter 4

Parameter Optimisation for Coating

Developing high-performance transition metal dichalcogenide (TMD) coatings through magnetron sputtering necessitates precise control of numerous interdependent process parameters that collectively determine coating quality, adhesion, and tribological performance. Despite extensive literature on TMD coatings, researchers often encounter a significant challenge: the absence of comprehensive parameter sets that can be directly transferred between different sputtering systems. As shown in the "Literature Survey of Sputtering Parameters" Table 4.1, substantial variation in parameter selection exists across published studies, with some reporting only partial information. In contrast, others employ vastly different parameter combinations to achieve similar tribological outcomes. This inconsistency highlights the equipment-specific nature of optimal sputtering parameters and underscores the necessity for systematic parameter optimisation for any indigenous coating development initiative.

The parameter optimisation approach adopted in this study begins with a comprehensive literature analysis to establish parameter boundaries and relationships. The compiled database, cataloguing 38 studies spanning nearly five decades of research, reveals the evolution of sputtering parameters for MoS_2 and Ti-doped MoS_2 coatings. This meta-analysis identifies critical parameters including working pressure (0.26-7.5 Pa), substrate voltage (36-500 V), target bias voltage (-40 to -70 V), deposition time (20-180 minutes), substrate temperature (ambient to 200°C), and target-to-substrate distance (41-150 mm). The resulting tribological performance metrics- coefficient of friction (0.04-0.14) and wear rates (10^{17} to 10^6 mm³/Nm)-demonstrate the sensitivity of coating performance to parameter selection.

While these studies provide valuable reference points, the indigenous development of TMD coatings requires tailored parameter optimisation specific to the available equipment configuration. Building upon this literature foundation, this chapter presents a systematic approach to parameter optimisation for the Mansha Vacuum Equipment sputtering system.

Table 4.1: Literature Survey of Sputtering Parameters

Sputtering Technique	DC-magnetron sputtering	DC magnetron sputtering	Unbalanced magnetron	DC magnetron sputtering	DC magnetron sputtering
Coating Thickness (µm)	1 - 4 (1 for all lowest)		2.18 - 2.47 (Ti + Si)	1.2	1
Composition of Substrate	AISI D2 steel & Si Wafer	AISI M42 tool steel & Si wafer	304 SS and silicon wafer	M42 1200 SiC steel	
Targets	MoS_2, Ti	MoS_2, Ti	MoS_2, Ti, Si	MoS_2, Ti	MoS_2, Ti
Shape and Size of Substrate (mm)			SS: 30 x 30 x 2 , Si: Φ50 x 1		
Shape and Size of Targets					
Roughness,Texture, Pre-processing	$Ra \leq 0.12$ µm				
Working Pressure (Pa)	0.26-0.40 (Pa)				
Base/Vaccum Pressure			$< 1 \times 10^{-3}$ (Pa)		
Substrate Voltage (-V)	30-70 (-V)		500 (-V) (Initial 10 min)		
Bias Voltage - Ti Target			- 70 (V)		
Bias Voltage - MoS_2 Target					
Magnetron Current (A) - Ti Target	0.3-0.9 (A)		3 to 0.8 A(after Ti layer)		
Magnetron Current (A) - MoS_2 Target	0.5-1.5 (A)				
Deposition Time - Ti	4 min		100 s		
Deposition Time - MoS_2					
Deposition Time - Overall	80 min		120 min		
Substrate Temperature					<100 ºC
Substrate to Source/Target Distance					
Substrate speed of rotation infront of Targets					
Inert Gas	Ar		Ar		
Inert Gas Pressure					
Inert Gas Flow (sccm)					
Purity of Targets			> 99.9 %		
Number of each targets		2 MoS_2, 1 Ti, 1 Metal	2 MoS_2, 1 Ti, 1 Si	3 MoS_2, 1 Ti	2 MoS_2, 1 Ti, 1 Metal
Sputtering Thickness - Ti		100 nm		70 nm	
Sputtering Thickness - MoS_2 + Ti		M - 200 nm, NM - 800 nm		M - 200 nm . NM - 900 nm	
Sputtering Thickness - MoS_2		50 nm		50 nm	
Wear Rate	$0.639-1.8 \times 10^{-6}$ mm³/Nm	4×10^{-17} m³/mN	3.22×10^{-7} m³/Nm	3.1×10^{-17} m³ /mN	4×10^{-17} m³ /mN
CoF	0.05-0.06	0.04 - 0.1	0.0432	0.04–0.045	0.043
Roughness			0.62 - 1.67 µm	Ra = 1 µm	
Ti %	2- 30	10-20			5-15 %
	[4]	[21]	[22]	[25]	[31]

Sputtering Technique	Non-equilibrium magnetron	RFMS with cylindrical chamber	CFUBMS	RF magnetron sputtering	RF & DC magnetron
Coating Thickness (µm)		1	1	1	
Composition of Substrate		SCM420 steel	AISI 52100 and M50	440C steel	
Targets	MoS_2, Ti	MoS_2, Ti	MoS_2, Ti	MoS_2, Ni/Au-Pd	MoS_2-Sb_2O_3- Au, Ti
Shape and Size of Substrate (mm)	SS discs (Φ35 mm × 5 mm)	Φ 45 × 8 mm, Φ 30 × 3 mm	Ball		
Shape and Size of Targets					
Roughness,Texture, Pre-processing	Precipitation hardened	Carburizing & Quenching			
Working Pressure (Pa)	0.5 Pa	$< 6.7 \times 10^{-3}$ Pa		0.266 Pa	
Base/Vaccum Pressure	2×10^{-3} Pa	7×10^{-4} Pa	1×10^{-6} Torr	1×10^{-5} Pa	7.5×10^{-5} Pa
Substrate Voltage (-V)	100 {1000 (-V) (Initial 15 min)}		- 500 V		-400 V
Bias Voltage - Ti Target					
Bias Voltage - MoS_2 Target					60 V
Magnetron Current (A) - Ti Target	1		0.6 A		
Magnetron Current (A) - MoS_2 Target	2.5		1.3 A		
Deposition Time - Ti					
Deposition Time - MoS_2					
Deposition Time - Overall	50 min	20 min			
Substrate Temperature			<80 ºC	<100 ºC	100 ºC
Substrate to Source/Target Distance					
Substrate speed of rotation infront of Targets					
Inert Gas	Ar	Ar	Ar		Ar
Inert Gas Pressure			1.6×10^{-3} Torr		0.63 Pa (4.7×10^{-3} Torr).
Inert Gas Flow (sccm)			50 sccm		0.83 N-m³/s (50 sccm)
Purity of Targets		> 99.9 %			82% MoS_2, 11% Sb_2O_3 & 7% Au
Number of each targets		1 MoS_2, 1 Ti	2 MoS_2,2 Ti	2 MoS_2, 2 Ni/Au-Pb	
Sputtering Thickness - Ti			200 nm		100 nm
Sputtering Thickness - MoS_2 + Ti					800 nm
Sputtering Thickness - MoS_2					
Wear Rate	1.5 - 2.8 $\times 10^{-6}$ mm²/ Nm				
CoF	0.004 -> 0.010 - 0.020	0.045 - 0.08	0.06 - 0.14	0.04 - 0.08	0.04 (Vaccum) - 0.14 (Air)
Roughness	Ra = 98 nm (NITRIDED)				Ra = 0.337 µm
Ti %	9.5 %				
	[21]	[23]	[26]	[27]	[32]

Sputtering Technique		CFUMS	RF & DC magnetron	RF sputtering	CFUMS	CFUBMSIP
Coating Thickness (µm)		1			0.78 +/- 0.11	
Composition of Substrate		AISI 52100 steel	AISI 52100 steel	304 stainless steel (SS)	AISI 52100 steel	
Targets		MoS_2, Ti	MoS_2-Sb_2O_3- Au, Ti	MoS_2, Cr_3Si_2		MoS_2/Ti , MoS_2/Au
Shape and Size of Substrate (mm)		Steel substrate coupons		SS discs	Φ12.7mm balls, Φ50 mm discs, Φ10 mm discs	
Shape and Size of Targets					5 × 15 × 0.375 in3	
Roughness,Texture, Pre-processing					Ra :0.01–0.02 µm,0.2 µm,0.01 µm	
Working Pressure (Pa)					213 $\times 10^{-5}$ Pa	
Base/Vaccum Pressure		6.6×10^{-4} Pa		1.3×10^{-4} Pa	1.33×10^{-4} Pa	Au-1.33×10^{-7} Pa, Ti - $5-6 \times 10^{-6}$ Torr
Substrate Voltage (-V)			60 VDC	- 80 V	-500 V	Ti : -30V (-350V for 1st 15min)
Bias Voltage - Ti Target				input power- 500 J/s		
Bias Voltage - MoS_2 Target				2 kV d.c.		
Magnetron Current (A) - Ti Target			Power - 190 W	Power - 80 W	Au Power density - 0.25 W/cm²,	
Magnetron Current (A) - MoS_2 Target		Power density-2 W/cm³	Power - 600 W	Power - 120 W	Power density - 3 W/cm²,	
Deposition Time - Ti						
Deposition Time - MoS_2						
Deposition Time - Overall						
Substrate Temperature		190 ºC		30ºC & 200 ºC	120 ºC	200 ºC
Substrate to Source/Target Distance		57 mm		41 mm		Ti - 150 mm
Substrate speed of rotation infront of Targets						Ti - 4.0 rpm
Inert Gas			Ar (purity 99.9%)		Ar (purity 99.6%)	Ar (purity 99.9%)
Inert Gas Pressure				1 - 1.7 Pa		Au-4 Pa, Ti-3.0 x 10^{-3} Torr
Inert Gas Flow (sccm)		90 ml/min	50 sccm		8.33×10^{-7} m³/s (50 sccm)	
Purity of Targets		(82% MoS_2, 11% Sb_2O_3 and 7% Au), 99.99% Ti			99.60%	Ti - 3.8 %, Au - 11.2%
Number of each targets		2 MoS_2,2 Ti				
Sputtering Thickness - Ti			200 nm	100 nm	Cr_3Si_2 - 50 nm (@ 0.4 nm/s)	
Sputtering Thickness - MoS_2 + Ti				800 nm		
Sputtering Thickness - MoS_2					300 - 500 nm (@ 0.4 - 0.8 nm/s)	
Wear Rate						
CoF				0.07 - 0.34	0.10 +/- 0.02	M-0.14, Au-0.10, Ti-0.11
Roughness					Ra = 0.008 µm	Ra :M-4.9nm, Au-5.2nm, Ti-3.3nm
Ti %					16%	
	[33]	[34]		[35]	[36]	[37]

58

The chapter progresses from parameter identification and boundary establishment to experimental design, coating characterisation, and statistical analysis of results, culminating in an optimised parameter set for indigenous production of high-performance TMD-based solid lubrication coatings for missile applications.

4.1 Substrate and Target Material Characterisation Before Coating

The initial characterisation of substrate and target materials is critical in establishing baseline parameters for subsequent coating development. The XRF analysis of the uncoated 17-4PH steel substrate confirmed its chemical composition aligns with standard specifications, showing iron as the predominant element (76.83 ± 0.16%) followed by chromium (15.07 ± 0.13%), nickel (3.41 ± 0.09%), and copper (2.91 ± 0.08%). These values are consistent with the expected.

XRF

Fe:	76.83 ± 0.16%
Cr:	15.07 ± 0.13%
Ni:	3.41 ± 0.09%
Cu:	2.91 ± 0.08%
Mn:	0.79 ± 0.12%
Si:	0.41 ± 0.07%
Mo:	0.24 ± 0.01%
Nb:	0.21 ± 0.01%
P:	0.06 ± 0.03%
V:	0.05 ± 0.06%
S:	0.02 ± 0.06%

Element	Weight %	MDL	Atomic %	Error %
New Project | New Sample | Area 311 | Selected Area 1				
S K	0.0	0.00	0.0	100.0
Ti K	0.2	0.50	0.2	70.3
Cr K	15.9	0.59	17.0	5.7
Mn K	1.2	1.42	1.2	37.8
Fe K	74.1	0.95	73.8	3.3
Co K	0.9	1.23	0.8	64.7
Ni K	4.2	1.36	4.0	7.4
Cu K	3.1	1.38	2.7	32.3
Mo L	0.5	0.89	0.3	62.6
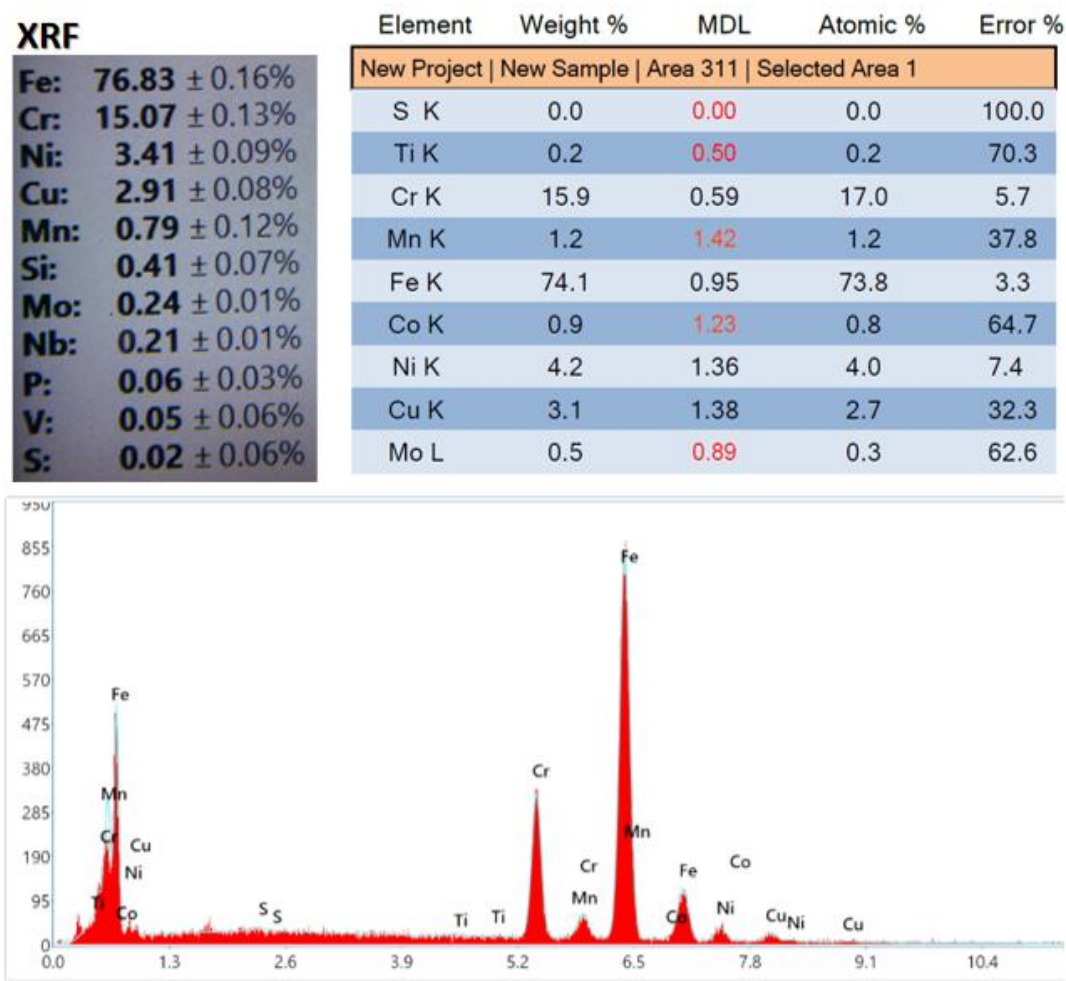
Figure 4.1: XRF and SEM-EDS analysis of uncoated 17- 4PH steel substrate showing elemental composition and corresponding spectrum, confirming compliance with standard alloy specifications.

Composition range for precipitation-hardening stainless steel grade 630, as established in ASTM standards. The presence of minor alloying elements, including manganese (0.79%), silicon (0.41%), molybdenum (0.24%), and niobium (0.21%), was also detected, essential for understanding the substrate's mechanical properties and potential interaction with the intended coating.

SEM-EDS analysis of the MoS_2 target revealed a near-ideal stoichiometric ratio with sulfur and molybdenum at 38.9 wt% (65.6 at%) and 61.1 wt% (34.4 at%). The calculated atomic ratio (N_S/N_{Mo} = 1.9) approaches the theoretical value of 2.0 for stoichiometric MoS_2, indicating high target quality suitable for achieving the desired coating composition. This analysis is particularly significant as previous studies have shown that sputtered MoS_2 coatings are often substoichiometric while maintaining the characteristic crystal structure. The SEM image further reveals the surface topography of the target, displaying characteristic machining marks that can influence the initial sputtering behaviour.

Element	Weight %	Atomic %
S K	38.9	65.6
Mo L	61.1	34.4
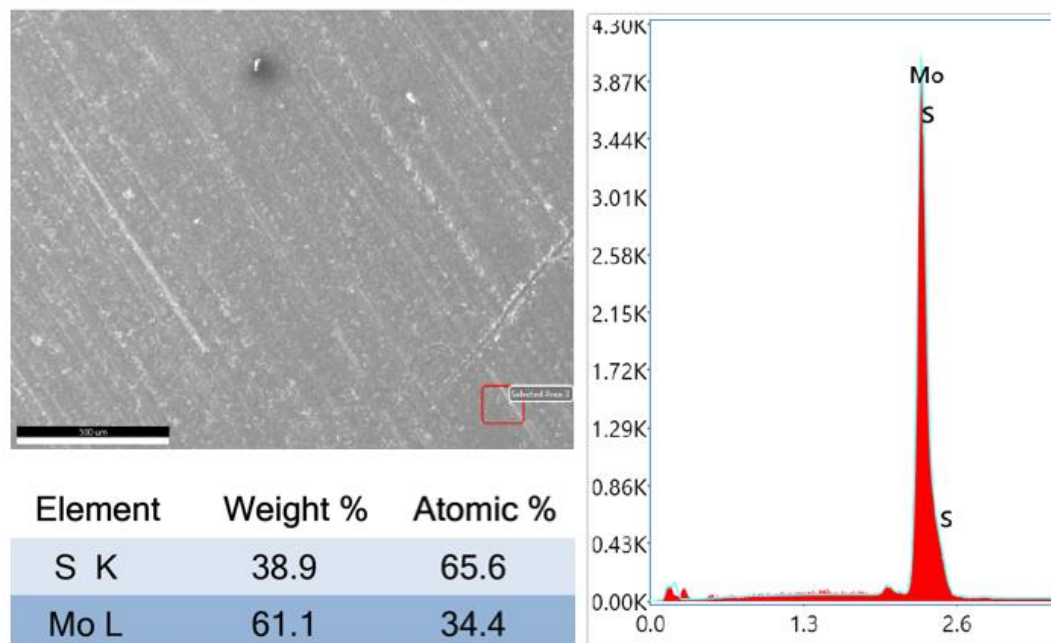
Figure 4.2: SEM-EDS analysis of the MoS_2 target showing surface morphology, elemental mapping, and quantitative stoichiometry confirming a near-ideal Mo:S atomic ratio close to 1:2.

The comprehensive characterisation performed through XRF and SEM-EDS techniques establishes critical reference points for subsequent coating development. This preliminary analysis serves multiple purposes: it verifies material composition before processing, provides baseline data for tracking compositional changes during deposition, and ensures that any observed variations in coating performance can be attributed to processing parameters rather than starting material inconsistencies. This initial benchmarking step is essential for developing reproducible coatings with optimal solid lubrication properties, particularly for MoS_2 coatings, where the stoichiometry significantly impacts tribological performance through its influence on crystallinity and orientation.

4.2 RF Sputtering Parameter Optimisation for MoS_2 Coating

The simultaneous deposition of MoS_2 coatings on both glass and 17- 4PH steel substrates provided critical insights into substrate-dependent growth behaviour during RF magnetron sputtering parameter optimisation. As shown in the Table, the visual characteristics of the coatings varied dramatically between substrate materials- glass surfaces exhibited colour variations from yellowish tints to deep black. In contrast, steel substrates showed different appearances from slight discolouration to uniform dense coatings. This dual-substrate approach enabled multi-faceted evaluation: glass substrates facilitated direct optical assessment and subsequent spectroscopic characterisation due to their transparency, while 17- 4PH steel substrates represented the actual target application material with its distinct surface energy, roughness, and thermal conductivity characteristics. The stark difference in coating appearance between experiments 1 and 4 across both substrate types confirms that parameter optimisation transcends substrate material, though adhesion mechanisms differ substantially.

The experimental matrix reveals that the simultaneous reduction of substrate-to-target distance (SOD) from 75 mm to 45 mm and increase in power parameters (0.78A/320V to 0.95A/390V) transformed coating morphology from non-uniform and grayish to dense and black regardless of substrate type. According to search results, these parameter adjustments fundamentally alter the growth mechanism of MoS_2 films. At shorter SOD values, sputtered atoms arrive at the substrate with higher kinetic energy before thermalisation, promoting enhanced surface mobility

and denser packing that minimises columnar void formation. The higher applied power simultaneously increases adatom energy and deposition rate, establishing conditions favouring the formation of well-crystallised films with preferred (002) orientation, where MoS_2 basal planes align parallel to the substrate surface. This orientation represents the ideal configuration for solid lubrication applications, as it facilitates easy shearing between adjacent MoS_2 layers under tribological loading.

Table 4.2: Sputtering parameters used in optimising MoS2 coating

Sr. No.	Ar Gas		SOD (mm)	Current (A)	Voltage (V)	Time (min)	Observations
	Pressure (bar)	Flow rate (sccm)					
1	4	10	75	0.78	320	150	Glass was yellowish, with slight discolouration on the steel.
2	4	10	75	0.95	390	150	Nonuniform Greyish coating
3	4	10	45	0.78	320	150	Uniform Greyish coating
4	4	10	45	0.95	390	150	Dense black coating

The optimised parameter set (4 bar pressure, 45 mm SOD, 0.95A/390V) produced consistent high-quality coatings across both substrate types, indicating robust processing conditions suitable for industrial implementation. The formation of dense black coatings, particularly evident in the rightmost sample image, suggests substantially reduced columnar structure, a critical achievement for mechanical

durability in high-stress applications. This finding aligns with literature observations that controlled deposition parameters can suppress the formation of columnar boundaries that typically act as pathways for oxygen diffusion and mechanical failure. While amorphous structures may form initially during room temperature deposition, the relatively high energy conditions of the optimised parameters likely promote localised crystallisation with the development of short-range order similar to the effects reported by Spalvins at moderate substrate temperatures. This systematic approach to parameter optimisation establishes a foundation for reproducible production of high-performance MoS_2 coatings on precision 17- 4PH steel components for missile applications.

Figure 4.3: Photographs of MoS_2 coatings deposited on glass and 17- 4PH steel substrates under varying sputtering parameters, illustrating changes in coating uniformity and colour with different substrate-to-target distances and process conditions.

Figure 4.4: RF sputtering setup showing power supply settings and plasma discharge during MoS$_2$ coating deposition, with real-time monitoring of RF power and tuning parameters.

The SEM-EDS area scan methodology provided a systematic approach for verifying MoS$_2$ coating deposition and evaluating compositional stoichiometry. As illustrated in Figure 4.5, a direct comparison between coated and taped areas on the same 17- 4PH substrate reveals distinct elemental signatures that confirm successful deposition. During the coating process, a portion of each substrate was masked with polyimide (Kapton) tape to create an intentional boundary between coated and uncoated regions. The tape was removed post-deposition to expose the pristine substrate surface, enabling a controlled internal reference for elemental analysis within each sample.
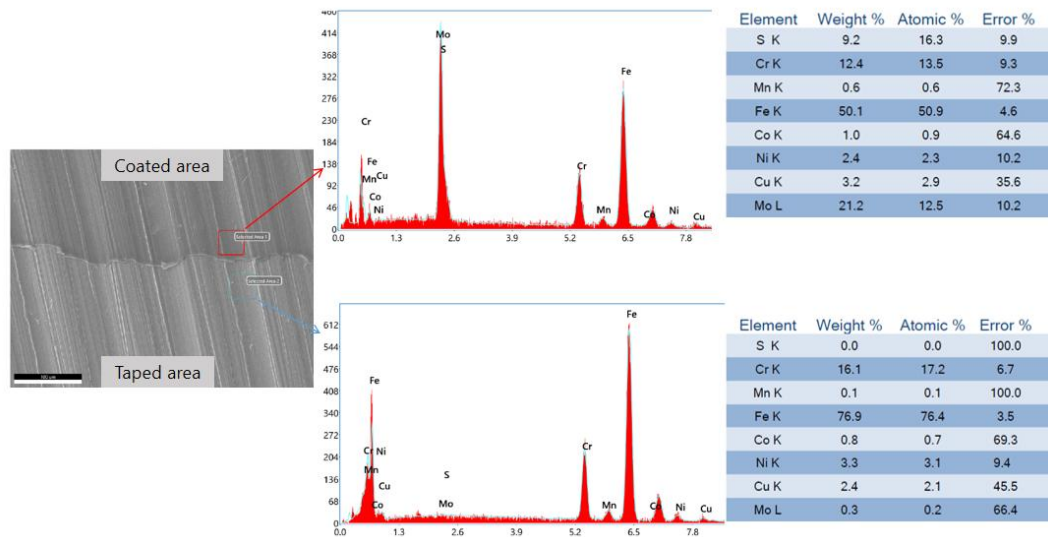
Figure 4.5: SEM-EDS area scans comparing the coated and taped regions on 17-4PH steel substrate, confirming successful MoS$_2$ deposition through distinct Mo and S peaks in the coated area and absence of these elements in the taped (uncoated) region.

The EDS area scan results demonstrate pronounced compositional differences between the two regions. The coated area spectrum displays prominent Mo peaks with significant S content (21.2 wt% Mo and 9.2 wt% S), translating to 12.5% and 16.3% atomic percentages, respectively. This yields an S/Mo atomic ratio of 1.3:1, indicating a slightly substoichiometric composition compared to the ideal 2:1 ratio for MoS$_2$. This finding aligns with established literature reporting that sputtered MoS$_2$ films typically exhibit substoichiometry while maintaining their tribological properties. In contrast, the taped area shows negligible Mo content (0.3 wt%, 0.2

at%) and essentially no detectable sulfur, confirming both the effectiveness of the masking technique and the absence of pre-existing molybdenum or sulfur compounds in the substrate.

The substrate elemental composition also shows distinctive patterns between regions, with the coated area revealing attenuated substrate peaks (Fe K at 50.1 wt% versus 76.9 wt% in the taped area) due to the overlying MoS_2 coating absorbing a portion of the electron beam energy. This attenuation effect serves as an indirect indicator of coating thickness and coverage uniformity. The optimisation process utilised these comparative EDS results across multiple parameter sets (voltage, current, time, pressure) to systematically identify conditions that yielded the desired S/Mo stoichiometry and substrate peak attenuation characteristics. The SEM-EDS methodology thus provided crucial feedback for iteratively refining the sputtering parameters to achieve optimal coating composition and coverage under the RF power settings of 320V and 0.78A utilised in this particular deposition run.
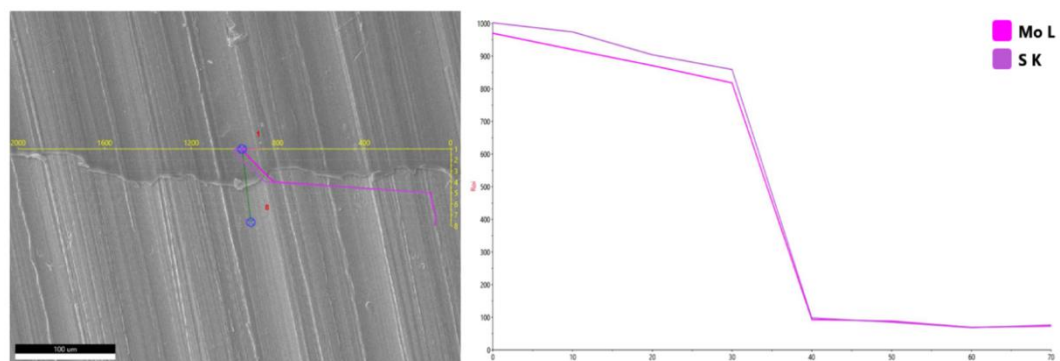
Figure 4.6: SEM-EDS line scan analysis across MoS_2 coating deposited at 320 V (0.78 A) for 150 minutes, showing uniform Mo L and S K signal intensities across the coated region, followed by a sharp decline at the coating boundary, confirming consistent elemental distribution within the deposited film.

The SEM-EDS line scan analysis in the Figure provides critical insight into the spatial distribution and interface characteristics of the MoS_2 coating deposited at 320 V (0.78 A) for 150 minutes. The left panel displays the SEM micrograph of the 17- 4PH steel substrate with visible polishing marks, overlaid with the scan trajectory (yellow line) crossing the boundary between coated and uncoated regions. The corresponding elemental intensity profiles on the right demonstrate

remarkably uniform Mo L and S K signal strengths throughout the first 30 μm of the scan path, indicating homogeneous elemental distribution within the coating. At approximately 35 μm, both signals drop abruptly, creating a sharp compositional gradient that defines the coating boundary with exceptional clarity. The parallel decline of both Mo and S signals confirms stoichiometric consistency throughout the coating thickness and lateral extent. This line scan analysis complements the area scan data by verifying coating uniformity and distinctly demarcating the transition between coated and uncoated regions. This is essential for accurately assessing deposition parameters and their effect on coating integrity.

4.3 Titanium Interlayer Parameter Optimisation

The optimisation of titanium interlayer deposition parameters represents a critical phase in developing high-performance TMD-based solid lubrication coatings. As shown in Table 5.2, a systematic approach was employed to identify optimal process conditions for titanium deposition while maintaining constant argon pressure (4 bar), flow rate (10 sccm), and substrate-to-target distance (SOD, 45 mm). The primary variable under investigation was power delivery, incrementally increased from 0.58A/230V to 0.73A/290V, with each parameter set producing distinct coating characteristics. This methodical power escalation strategy revealed a clear correlation between applied power and coating quality, transitioning from porous blue-tinted deposits at lower power settings to uniform greyish coatings with minimal porosity at higher power levels. The experimental results demonstrate that 0.73A/290V represents the optimal power configuration before the onset of target arcing observed at 330V, where plasma instability compromised coating integrity.

The visual assessment of Ti-coated glass and steel substrates (as seen in the accompanying images) provides immediate feedback regarding coating quality and uniformity. Sample 3, produced at 0.73A/290V, exhibits a uniform greyish appearance with no visible porosity, indicating dense film formation with good adhesion characteristics. This visual assessment was corroborated by subsequent SEM-EDS analysis of the coated steel substrate, confirming a continuous titanium layer with minimal oxygen contamination. The transition from the blue colouration in sample 1 to the metallic grey appearance in sample 3 signifies

progressive improvement in coating density and reduction in optical interference effects typically associated with thin, non-continuous films. Eliminating visible porosity in sample 3 is particularly significant, as pore-free titanium interlayers are essential for preventing localised coating failure when subjected to tribological loading.
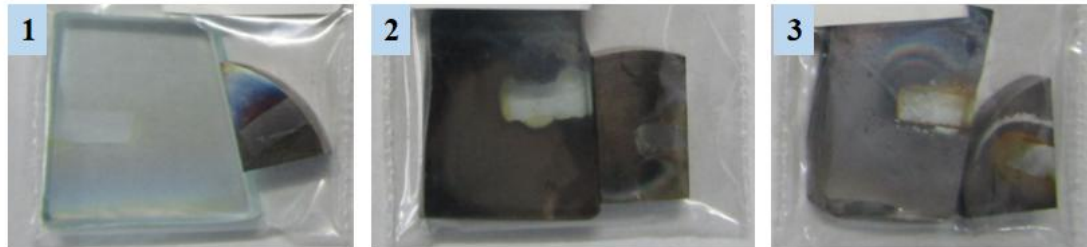
Figure 4.7: Visual comparison of Ti coatings on glass and 17- 4PH steel substrates deposited at increasing power settings (from left to right: 0.58A/230V, 0.65A/260V, 0.73A/290V), showing transition from thin blue-tinted films to dense, uniform grey coatings as power increases.

Table 4.3: Sputtering parameters used in optimising Ti coating

Sr. No.	Ar Gas		SOD (mm)	Current (A)	Voltage (V)	Time (min)	Observations
	Pressure (bar)	Flow rate (sccm)					
1	4	10	45	0.58	230	150	Blue colour coating with porosity on glass
2	4	10	45	0.65	250	150	Partial Greyish coating with porosity on glass
3	4	10	45	0.74	300	150	Uniform Greyish coating with no porosity on glass
4	4	10	45	0.55 - 0.83	320	150	Arcing of the target (Reserve

							Power issue)

The successful optimisation of titanium interlayer parameters establishes a foundation for subsequent MoS₂ deposition. The titanium interlayer serves multiple critical functions: it enhances adhesion between the 17- 4PH substrate and the MoS₂ top layer through strong interfacial bonding, improves load-bearing capacity through its higher hardness relative to pure MoS₂, and creates a chemical gradient that promotes coating integrity. While the experimental matrix revealed that excessive power (sample 4) leads to detrimental target arcing and potential contamination, the identified optimal parameters (0.74A/300V) successfully balance deposition rate and coating quality. This parameter set will be employed for interlayer deposition in the final bilayer coating architecture, where the titanium layer thickness will be controlled through precise timing to achieve the desired Ti: MoS₂ ratio for optimal tribological performance in missile applications.

Figure 4.8: RF sputtering setup during Ti deposition, showing power supply and auto tuner settings (left) alongside plasma discharge and substrate positioning inside the vacuum chamber (right).

The cross-sectional SEM-EDS analysis in Figure 4.9 provides critical insights into the titanium coating morphology, thickness, and interfacial characteristics of the 17- 4PH steel substrate. One of the 1 mm³ cube specimens was strategically polished on a single face to prepare this specialised sample to achieve a mirror finish suitable for coating adhesion analysis. In contrast, an adjacent face was

masked with polyimide tape before deposition. This configuration created a unique cross-sectional geometry after coating deposition at 300 V (0.73 A) for 60 minutes, enabling direct observation of the coating-substrate interface and precise coating thickness measurement.
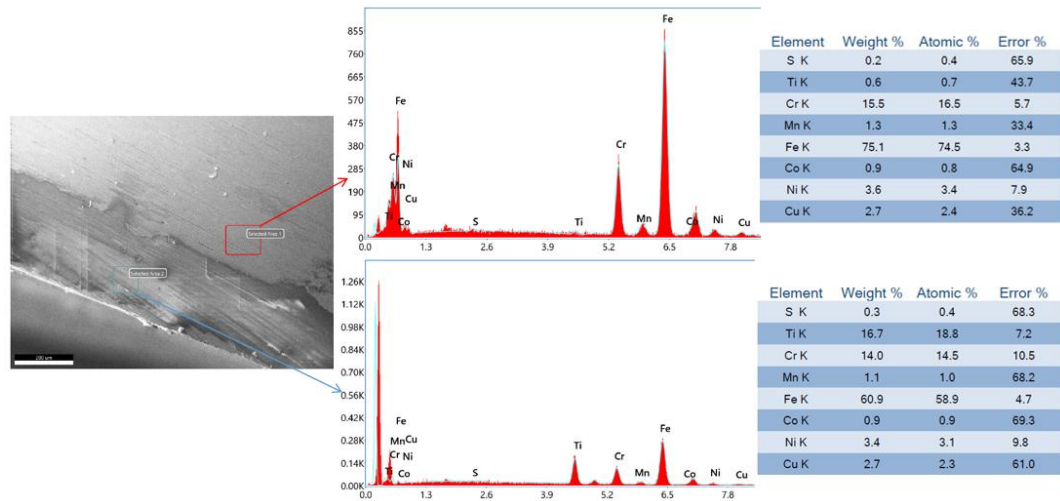
Figure 4.9: Cross-sectional SEM-EDS analysis of Ti-coated 17- 4PH steel substrate (deposited at 300 V, 0.74 A, 60 min), showing distinct Ti-rich coating layer and corresponding elemental spectra and quantification for both substrate and coated regions.

The SEM micrograph on the left reveals the titanium coating as a distinct layer along the polished edge of the cube sample, appearing as a brighter region against the darker steel substrate. The accompanying EDS analysis confirms substantial titanium enrichment in the coating region, with 16.7 wt% (18.8 at%) Ti detected in the analysed area compared to just 0.6 wt% (0.7 at%) in the substrate region. This dramatic difference in titanium concentration confirms successful deposition and provides quantitative compositional data for assessing coating stoichiometry. Additionally, the attenuated substrate element signals (Fe reduced from 75.1 wt% to 60.9 wt%) in the coated region further validate the presence of a continuous titanium layer of sufficient thickness to partially shield the substrate from the electron beam.

This cross-sectional analysis technique offers significant advantages over conventional top-down SEM-EDS examination, as it enables direct visualisation of coating continuity, interface quality, and thickness uniformity. The method reveals that the titanium deposition at the optimised parameters produces a well-

adhered coating with minimal interfacial defects or voids that could compromise mechanical integrity during tribological loading. This cross-sectional characterisation approach provides essential feedback for verifying coating microstructure and interfacial properties, enabling parameter refinement to achieve the desired coating characteristics for missile applications.

The SEM-EDS line scan analysis presented in Figure 4.10 provides critical insights into the spatial distribution of titanium across the coating-substrate interface. The line scan methodology complements the area analysis by precisely
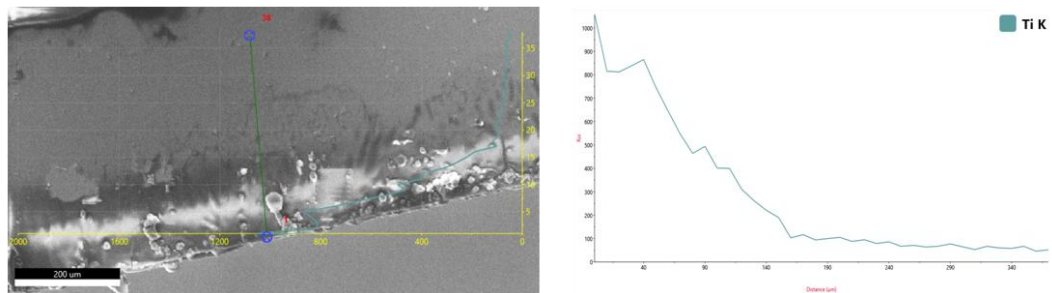
Figure 4.10: SEM-EDS line scan across the cross-section of Ti-coated 17-4PH steel (deposited at 300 V, 0.74 A, 60 min), showing the Ti K signal intensity profile decreasing from the coating surface into the substrate, confirming coating thickness and interface sharpness.

tracking elemental concentration changes along a defined trajectory, enabling quantitative assessment of coating thickness and interface characteristics. The left panel shows that the scan path (yellow line) traverses from the titanium-rich coating region into the 17- 4PH steel substrate. The corresponding titanium intensity profile on the right demonstrates a characteristic diffusion pattern with maximum Ti K signal intensity (~1000 counts) at the coating surface. This is followed by a steep gradient across approximately 140 μm. This gradient profile reveals essential information about the coating-substrate interaction, including limited titanium diffusion into the substrate and the absence of severe interfacial mixing despite the relatively high deposition energy (300 V). The profile gradually transitions to background levels (~50 counts) deeper into the substrate, confirming complete penetration through the coating thickness. This line scan analysis, conducted at the optimised deposition parameters (300 V, 0.74 A, 60 minutes), validates the formation of a well-defined titanium layer with appropriate thickness

for serving as an adhesion-promoting interlayer in the subsequent composite MoS_2/Ti coating architecture.

4.4 MoS₂-Ti Multi-layer Optimisation

4.4.1 Without Substrate rotation mechanism

Titanium (Ti) is initially sputtered as an adhesion layer under MoS_2 coatings to enhance the bonding between the substrate and the lubricating MoS_2 layer. Ti forms a strong, dense, uniform layer that improves coating durability and prevents delamination during high-stress applications. Ti's hardness and structural stability also provide a robust base, compensating for MoS_2's inherent softness. This combination ensures improved wear resistance, adhesion, and mechanical integrity, making it especially suitable for applications like missile components requiring low friction and high durability.

Target	Voltage (V)	Current (A)	Time (min)
Ti	300	0.74	60
MoS_2	390	0.95	240

Element	Weight %	Atomic %	Error %
S K	30.0	50.7	7.5
Ti K	17.1	19.4	12.9
Mo L	52.9	29.9	10.4
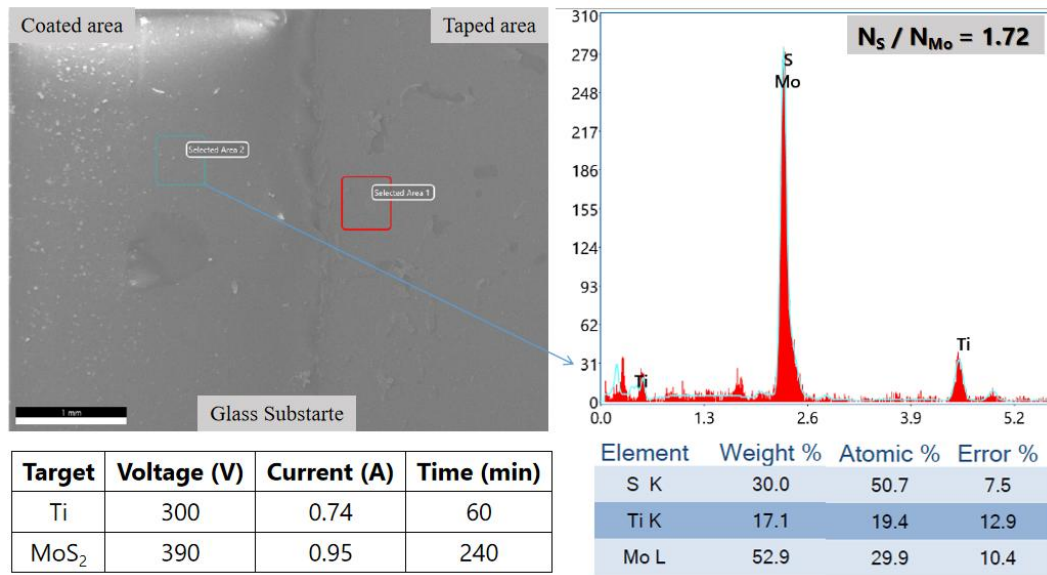
Figure 4.11: SEM-EDS area scan of MoS₂/Ti multilayer coating on glass substrate, showing selected coated and taped regions, corresponding elemental spectrum, and quantitative analysis confirming near-stoichiometric MoS_2 ($N_s/N_{mo} = 1.72$) with Ti interlayer, deposited under optimised sputtering parameters.

The SEM-EDS area scan analysis of the optimised MoS₂/Ti multilayer coating, as shown in Figure 4.11, reveals excellent compositional control achieved through the refined deposition parameters. The EDS spectrum displays prominent peaks for molybdenum, sulfur, and titanium, with quantitative analysis indicating weight

percentages of 52.9% Mo, 30.0% S, and 17.1% Ti, corresponding to atomic percentages of 29.9%, 50.7%, and 19.4%, respectively. Most notably, the calculated N_S/N_{Mo} nuclear ratio of 1.72 approaches the ideal stoichiometric value of 2.0 for MoS_2, indicating successful formation of near-stoichiometric MoS_2 in the coating matrix. This near-ideal stoichiometry is particularly significant as it aligns with published literature values for high-performance solid lubrication coatings, such as those reported by Wang et al. and Kong et al. [23], [25], where N_S/N_{Mo} ratios between 1.4-1.8 consistently demonstrated optimal tribological performance. The co-deposition using the optimised parameters (Ti: 300V/0.74A for 60min, MoS_2: 390V/0.95A for 240min) successfully achieves the target elemental composition required for adequate solid lubrication.

Ti - 60 min & MoS₂ - 240 min

100 µm
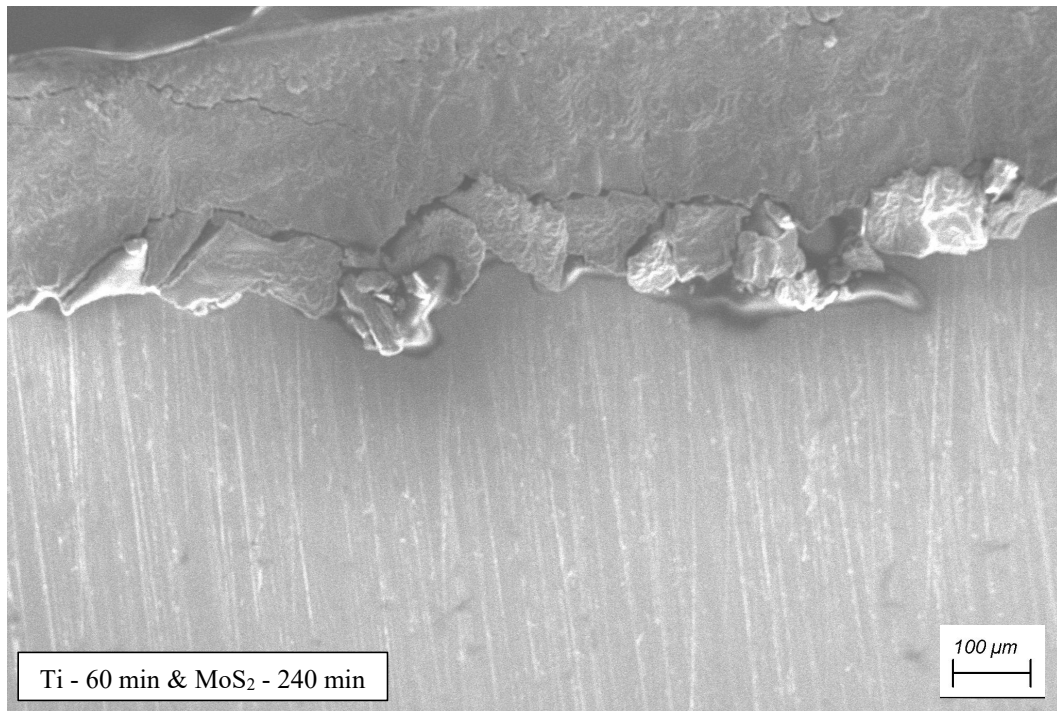
Figure 4.12: Cross-sectional SEM image of MoS₂/Ti multilayer coating on 17-4 PH steel cube substrate, showing the interface and coating adhesion with a clear boundary between the coating layers and substrate surface.

Cross-sectional SEM analysis of the coating, presented in Figure 4.12, confirms forming a well-defined bilayer structure with distinct Ti and MoS_2 layers. The titanium interlayer exhibits a uniform thickness of approximately 80-100 µm, while the MoS_2 top layer measures 280-300 µm, creating a total coating thickness of roughly 380 µm. This thickness ratio (approximately 1:3) correlates well with

the deposition time ratio (1:4), accounting for the different sputtering yields and deposition rates of the two materials under their respective optimised parameters. The presence of flaky structures is characteristic of MoS_2, which is known for its layered structure. The top MoS_2 layer exhibits some cracking and roughness, potentially due to residual stresses, coating growth mechanisms, or coating duration, as PVD coatings are meant for coating thickness less than 50 microns. The interface between the Ti and MoS_2 layers seems relatively sharp, indicating good adhesion between the two layers.

As demonstrated in the comparative study shown in Table 4.4, the compositional range achieved in this work (particularly run 4, with Mo at 35.04 at.%, S at 51.19 at.%, and Ti at 13.77 at.%) falls within the optimal range identified in the literature. Multiple research groups have reported that substoichiometric MoS_2 (N_S/N_{Mo} = 1.4-1.8) with moderate Ti doping (10-15 at.%) provides the best balance between coating hardness, adhesion, and lubricity.

Table 4.4: Quantitative results of elemental analysis of MoS2-Ti films determined by EDS [4]

Run	1	2	3	4	5	6	7	8	9
Mo (at.%)	36.40	39.44	45.88	35.04	41.84	36.04	37.68	28.01	39.08
S (at.%)	51.82	48.09	43.46	51.19	53.89	39.13	60.02	41.25	55.65
Ti (at. %)	11.78	12.46	10.66	13.77	4.27	24.83	2.30	30.74	5.26
N_S/N_{Mo}	1.42	1.21	0.94	1.46	1.28	1.08	1.59	1.47	1.42
N_{Ti}/N_{Mo}	0.32	0.31	0.23	0.39	0.10	0.68	0.06	1.09	0.13

Target	Voltage (V)	Current (A)	Time (min)
Ti	300	0.74	30
MoS_2	390	0.95	30
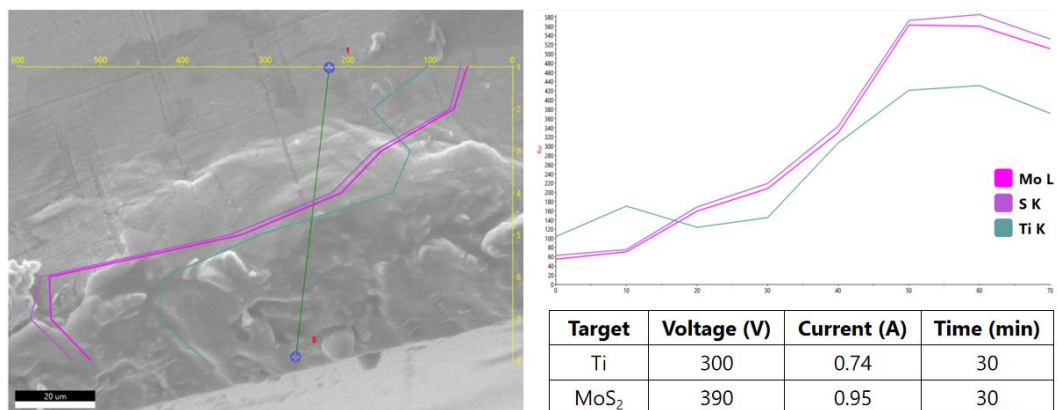
Figure 4.13: SEM-EDS line scan across the cross-section of MoS$_2$/Ti multilayer coating (Ti: 300 V, 0.74 A, 30 min; MoS$_2$: 390 V, 0.95 A, 30 min), showing distinct Mo, S, and Ti signal profiles and confirming successful sequential deposition and elemental distribution in the optimised thin bilayer structure.

To optimise coating thickness for practical applications, deposition times for both MoS$_2$ and Ti layers were systematically reduced to 30 minutes each, while maintaining the optimised voltage and current parameters (Ti: 300V/0.74A, MoS$_2$: 390V/0.95A). As shown in Figure 4.13, cross-sectional SEM-EDS analysis of this reduced-time coating reveals a proportional decrease in overall thickness. The line scan profile across the coating cross-section demonstrates clear elemental distribution patterns with distinct signals for Mo L, S K, and Ti K. The scan reveals a well-defined bilayer architecture with the Ti interlayer directly adjacent to the substrate, followed by the MoS$_2$ top layer. The sharp transitions in elemental intensities confirm minimal interdiffusion between layers despite the high-energy deposition conditions, indicating excellent interfacial integrity and compositional stability.

Ti - 30 min & MoS$_2$ - 30 min

10 µm
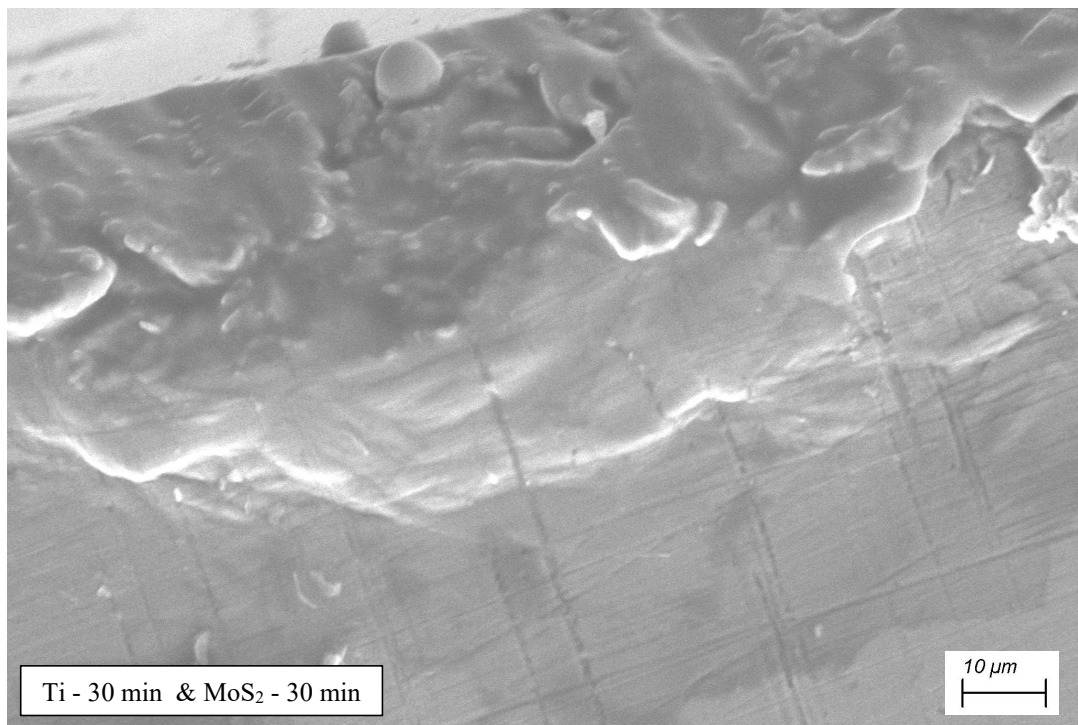
Figure 4.14: Cross-sectional SEM image of MoS$_2$/Ti multilayer coating on steel substrate, showing the uniform morphology and interface between the coating and substrate at high magnification

Figure 4.15: Coating morphology reported in literature [23], [35]

The cross-sectional morphology observed in Figure 4.14 demonstrates remarkable similarity to established coating structures reported in the literature [25], [35]. The optimised coating exhibits the characteristic layered architecture with minimal columnar growth, a critical achievement for high-performance solid lubrication applications. The total coating thickness is significantly reduced compared to the previous sample with longer deposition times. The Ti layer is visibly thinner, acting as a minimal adhesion layer. The MoS_2 layer is also relatively thin and lacks the pronounced columnar morphology of thicker coatings. The interface between the Ti and MoS_2 layers appears less distinct, potentially due to intermixing during the short deposition process or limited layer growth. The substrate-coating interface is smooth, indicating uniform deposition without visible delamination.

As illustrated in Figure 4.15, conventional MoS_2 coatings typically develop problematic columnar structures that create weak zones susceptible to mechanical failure. However, the current coating displays a more compact, less fibrous structure than the "equiaxed zone" morphology described in reference studies. This controlled morphology is attributed to the optimised deposition parameters, particularly the enhanced adatom mobility achieved through the optimal voltage/current combination and target-to-substrate distance. The reduction in deposition time while maintaining parameter optimisation successfully produced a proportionally thinner coating without sacrificing structural integrity or compositional stoichiometry, demonstrating the scalability and precision of the developed process parameters for tailored coating applications.

The cross-sectional analysis technique using specialised cube samples with polished and partially taped faces proved remarkably effective in revealing the multilayer architecture. This approach allows direct visualisation of the individual

layer thicknesses, the interface quality between the Ti interlayer and MoS_2 top layer, and between the Ti interlayer and the substrate. The sharp interface between layers with minimal interdiffusion suggests excellent process control during the sequential deposition. Similar methodologies have been employed in recent studies by Feng et al. [26] and in the $TiCrN/MoS_2$ work referenced, where cross-sectional SEM-EDS analysis was crucial for optimising multilayer coating architectures. The achievement of near-stoichiometric MoS_2 ($N_S/N_{Mo} = 1.72$) in the present work represents a significant milestone in the indigenous development of high-performance solid lubrication coatings, as this stoichiometry is known to maximise the formation of the basal-oriented crystal structure critical for low friction performance in tribological applications.

4.4.2 Incorporation of a substrate rotation mechanism
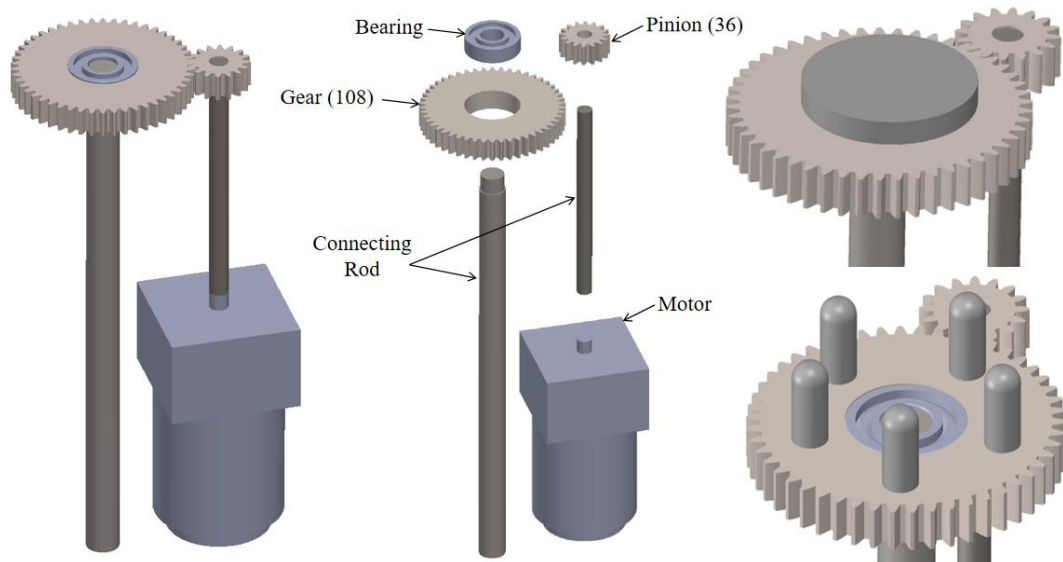
Figure 4.16: Visual representation of the Designed Rotation Mechanism using SolidWorks

Initial coating experiments revealed significant non-uniformity when utilising stationary, angled targets in the sputtering chamber. Surface mapping of the coated 17- 4PH steel samples showed thickness variations exceeding ±15% across the substrate surface, compromising the tribological performance and reliability of the TMD coatings. To address this critical challenge, an in-house substrate rotation mechanism was designed using SolidWorks CAD software, optimising a gear-driven system that would integrate seamlessly with the existing Mansha Vacuum Equipment chamber. The finalised design features a precision-

engineered gear train consisting of a large primary gear (108 teeth) that interfaces with a smaller pinion gear (36 teeth), creating a 3:1 reduction ratio. This gear ratio was calculated to provide optimal rotation speed while maintaining torque requirements for smooth substrate movement during deposition. The assembly includes robust connecting rods that transfer rotational motion from the motor housing to the substrate holder, with a precision bearing to ensure stability and reduce friction during continuous operation.

Following detailed design validation, the rotation system components were manufactured using Wire Electrical Discharge Machining (Wire EDM) for exceptional dimensional accuracy (±0.01mm) and surface finish quality. This manufacturing technique was selected for its ability to produce high-precision gear teeth with minimal thermal distortion, which is critical for maintaining exact mesh engagement and preventing backlash during rotation. The Wire EDM process enabled the fabrication of complex gear geometries from hardened 17-4PH steel stock without inducing residual stresses that could lead to component failure under vacuum conditions. The motor housing was designed with thermal management considerations to prevent overheating during extended deposition cycles, while the connecting rod assembly features adjustable positioning to accommodate various substrate configurations. This indigenous rotation mechanism integrates with the chamber's feedthrough system, allowing external rotation speed control between 2 and 10 RPM during deposition.
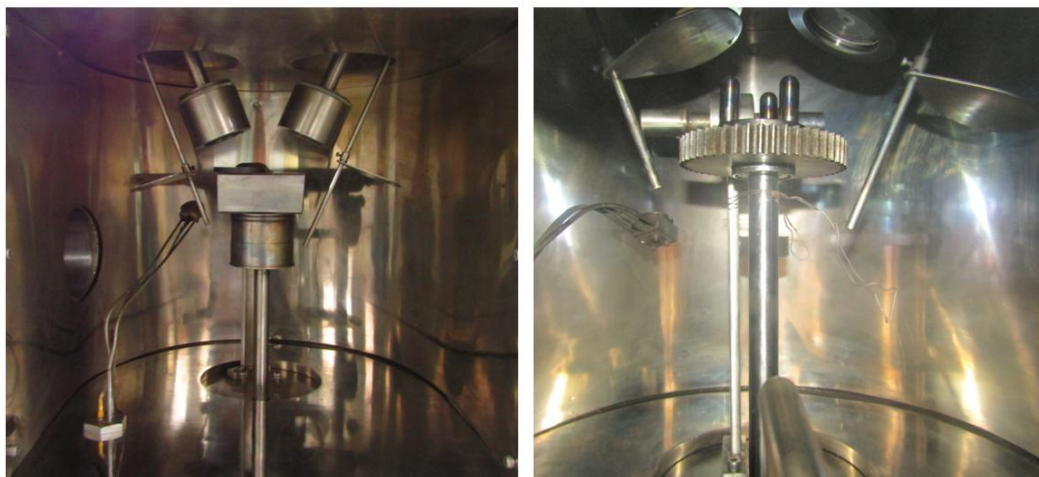
Figure 4.17: Sputtering chamber modifications: (left) initial setup with stationary substrate holder; (right) upgraded setup featuring a custom substrate rotation mechanism for improved coating uniformity.

The implementation of this rotation system dramatically improved coating uniformity by ensuring continuous substrate movement beneath the plasma discharge region. The rotation effectively neutralises deposition inconsistencies caused by plasma non-uniformities and target erosion patterns, while enhancing coating adhesion through more controlled energy transfer during film growth. The system's design also accommodates future upgrades, including programmable rotation profiles for multi-layer coating architectures, demonstrating the adaptability of indigenous solutions for advanced coating processes. This substrate rotation mechanism represents a critical technology enabling commercial-grade TMD solid lubrication coatings using domestic manufacturing capabilities. The coating process involves two main steps with previously optimised sputtering parameters on Si wafer (for coating morphology and thickness) and Bullets (for pin-on-disc testing) :

1. Deposition of a titanium (Ti) adhesion layer

2. Deposition of the MoS_2 lubricating layer

Table 4.5: Optimised sputtering parameters of MoS2 and Ti Coating

Target	MoS_2	Ti
Sputtering Technique	RF magnetron sputtering	DC magnetron sputtering
Composition of Substrate	Glass, 17-4 PH steel & Si Wafer	Glass, 17-4 PH steel & Si Wafer
Shape and Size of Substrate (mm)	Disc : Φ60 x 8 Cube : 1 x 1 x 1 Bullet : Φ12 x 30 (R6) Si wafer: Φ2.54 x 0.5	Disc : Φ60 x 8 Cube : 1 x 1 x 1 Bullet : Φ12 x 30 (R6) Si wafer: Φ2.54 x 0.5
Shape and Size of Targets	Round - Φ50.8 x 3	Round - Φ50.8 x 3
Roughness, Texture, and Pre-processing of Substrate	Polished	Polished
Base Pressure (mbar)	5×10^{-2}	5×10^{-2}

Vacuum Pressure (mbar)	5×10^{-5}	5×10^{-5}
Working Pressure (mbar)	1.4×10^{-1}	1.4×10^{-1}
Bias Voltage (V)	400	300
Magnetron Current (A)	0.55	0.72
Substrate Temperature	Ambient	Ambient
Substrate to Target Distance (mm)	50	50
Substrate speed of rotation in front of Targets (rpm)	3-4	3-4
Inert Gas	Ar	Ar
Inert Gas Pressure	4	4
Inert Gas Flow (sccm)	10	10
Purity of Targets	99.99	99.99
Number of targets	1	1

Figure 4.18: In-situ images of the custom substrate rotation mechanism during sputter coating, showing uniform plasma exposure for both disc (left) and bullet-shaped (right) samples to ensure consistent coating thickness and quality.

The custom-designed substrate rotation system was successfully implemented in the sputtering chamber to address non-uniform deposition patterns observed in early experiments. As shown in Figure 4.18 (top), the rotation mechanism

accommodates both disc-shaped specimens (left) and bullet-shaped pins (right) during the sputtering process, with the plasma discharge visibly enveloping the substrates. The rotation system operates at an optimised speed of approximately 15-16 rpm, identified through iterative testing. This aligns with findings in search literature indicating this range provides ideal adatom mobility and film structure development. This moderate rotation speed ensures uniform exposure of all substrate surfaces to the plasma flux while preventing excessive centrifugal forces that could compromise mounting stability or introduce vibration-related defects.

The rotation mechanism's effectiveness is particularly evident during extended deposition runs (30-240 minutes), where static positioning would otherwise result in significant thickness variations due to target erosion patterns and plasma non-uniformities.
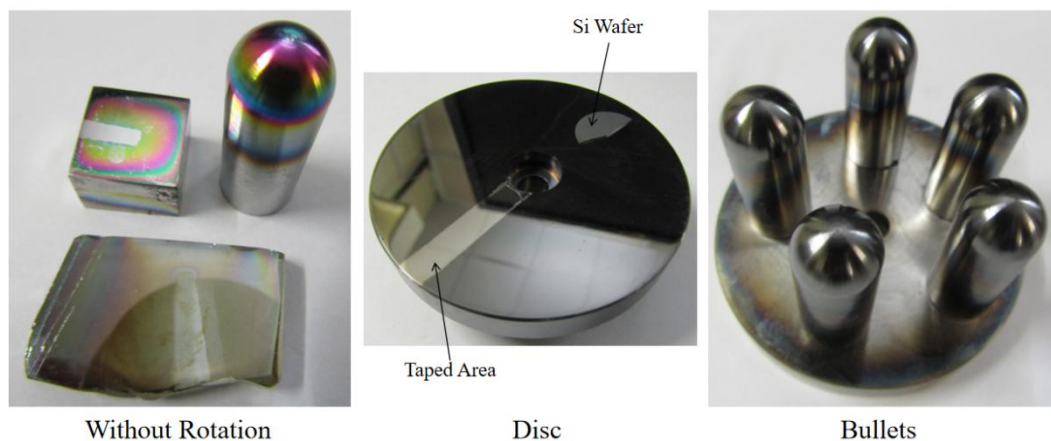
Figure 4.19: Comparison of coating uniformity on various substrates: (left) samples coated without rotation showing visible iridescence and non-uniform thickness; (center) disc sample with Si wafer and taped area after rotation-assisted coating, demonstrating uniform appearance; (right) bullet-shaped substrates coated with rotation, exhibiting consistent metallic finish across all surfaces.

Figure 4.19 (bottom) provides compelling visual evidence of the rotation mechanism's effectiveness through comparative photography of coated samples. The specimens prepared without rotation (left panel) exhibit characteristic rainbow-like iridescence patterns with pronounced colour variations across their surfaces, indicating significant thickness non-uniformity and inconsistent optical properties. In stark contrast, disc and bullet-shaped samples processed with rotation (centre and right panels) display uniform metallic appearance throughout their exposed surfaces. Silicon wafers were strategically co-deposited alongside

the 17- 4PH steel substrates at identical substrate-to-target distances, allowing direct correlation between coating properties on both substrate types. The Si wafer mounted on the disc sample (centre panel) clearly shows the boundary between coated and taped regions, providing an immediate visual confirmation of coating coverage. This controlled comparison demonstrates the critical role of substrate rotation in achieving the consistent coating thickness and composition necessary for reliable tribological performance in demanding missile applications.

The systematic optimisation of sputtering parameters for Ti and MoS_2 coatings and implementing a custom substrate rotation mechanism has established a robust foundation for producing high-performance solid lubrication coatings. Through iterative experimentation and characterisation, critical process variables- power, pressure, substrate-to-target distance, and deposition time- were fine-tuned to achieve near-stoichiometric MoS_2 ($N_s/N_{mo} \approx 1.7$) with a well-adhered Ti interlayer. The cross-sectional SEM-EDS analyses confirmed the formation of dense, defect-free bilayer coatings with controlled thickness (80–380 nm). At the same time, the substrate rotation system resolved earlier challenges of non-uniform deposition, as evidenced by the elimination of iridescence patterns and consistent metallic appearance across coated surfaces.

While this chapter focused on parameter optimisation and process development, the subsequent chapter will detail the comprehensive characterisation of coating morphology, crystallinity, and tribological performance. Silicon wafers co-deposited during these runs will enable precise thickness measurements via cross-sectional SEM. At the same time, XRD and Raman spectroscopy will elucidate the phase composition, crystallographic orientation, and bonding states critical to the coatings' solid lubrication properties. Pin-on-disc tribometry will quantitatively evaluate friction coefficients and wear rates under simulated operational conditions, directly linking the optimised parameters to functional performance. These analyses will validate the efficacy of the developed coating process and provide actionable insights for scaling the technology to missile guidance system components.

The transition to advanced characterisation marks a critical shift from process development to performance validation, bridging the gap between laboratory-scale optimisation and real-world application requirements.

Chapter 5

Results and Discussions

5.1 Coating characterisation

The cross-sectional SEM micrographs in Figure 5.1 reveal the microstructural features and precise thickness of the MoS_2/Ti coatings deposited on silicon wafers. The left image shows a coating with a measured thickness of 10.50 μm, while the right image displays a significantly thicker coating at 7.435 μm, reflecting the different deposition parameters applied. The fracture-based sample preparation technique provided clean cross-sectional surfaces ideal for high-resolution imaging, preserving the coating's true morphological features without introducing artefacts that might occur with mechanical polishing. This approach allows for visualisation of the coating's internal structure and interface quality with the silicon substrate. This is critical for understanding the coating formation mechanisms and potential performance characteristics.
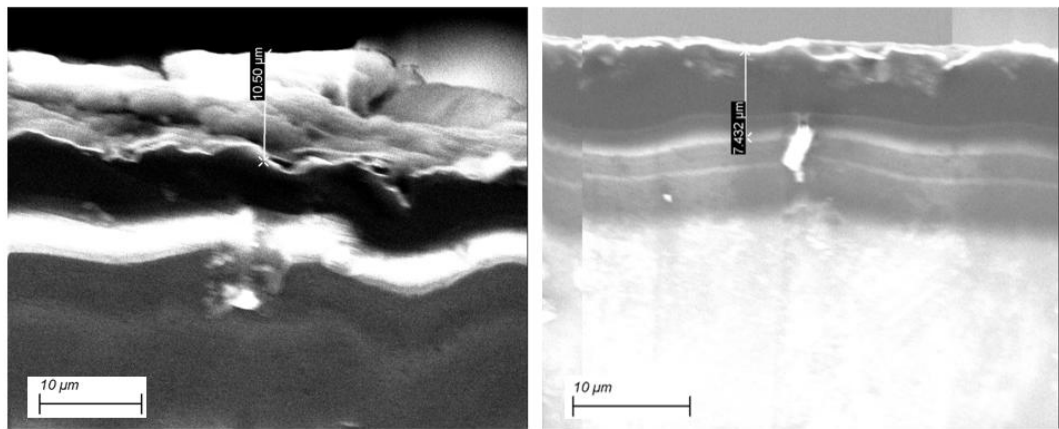
Figure 5.1: Cross-sectional SEM images of sputtered coatings showing columnar microstructure and measured thickness: (left) pure MoS_2 coating with well-defined columns (10.50 μm), (right) MoS_2+Ti bilayer coating with distinct layered architecture (13.375 μm), both exhibiting morphologies consistent with literature reports for sputtered TMD-based films.

Most notably, the cross-sectional images reveal a distinctive columnar microstructure that closely resembles the Zone 1 structure in Thornton's Structure Zone Model for sputter-deposited films, as illustrated in the comparative literature images (Figure 5.2, bottom). This columnar-fibrous morphology is characterised by tapered crystallites extending perpendicular to the substrate surface with voided

boundaries between columns, a characteristic feature of films deposited under conditions where adatom surface mobility is limited. The observed structure agrees with published findings on MoS_2 coatings, where researchers have documented similar columnar formations in sputtered films deposited at relatively low substrate temperatures and moderate working pressures. As the literature describes, this morphology typically arises from "low-angle oblique incidence of the thermalised particles and the limited diffusion of adatoms on the substrate surface," resulting in competitive growth of adjacent nucleation sites.

Figure 5.2: Coating morphology reported in literature [25], [35]

The thicker coating (7.435 μm) demonstrates a more pronounced columnar structure with column widening toward the surface, indicating evolutionary growth where initially formed columns dominate as deposition progresses. This structural feature is particularly significant for tribological performance, as columnar boundaries can significantly influence mechanical properties, including hardness and wear resistance. The observed microstructure suggests a Zone 1 growth regime according to Thornton's model, typically associated with relatively low homologous temperatures during deposition. This structural characterisation provides essential insights for subsequent optimisation, as columnar morphologies in MoS_2 coatings have been associated with higher wear rates and susceptibility to environmental degradation compared to denser, more basally oriented structures. The direct correlation between the observed microstructure and literature examples confirms successful replication of established coating morphologies while providing a foundation for process refinement to achieve the desired tribological performance.

The cross-sectional analysis was repeated using a JEOL SEM to address the charging effects encountered during initial examination with the Zeiss microscope. As shown in Figure 5.3, the JEOL SEM provided significantly enhanced imaging

capabilities, revealing detailed morphological features of pure MoS_2 (8.209 μm) and MoS_2+Ti (13.375 μm) coatings. The high-resolution micrographs demonstrate the columnar fibre zone structure in the pure MoS_2 coating (left image). In contrast, the MoS_2+Ti coating (right image) displays a distinct bilayer architecture with well-defined boundaries between the Ti interlayer and MoS_2 top layer. The columnar growth pattern observed in these coatings closely resembles those reported in published literature (No. 1- No. 5 comparison images), particularly the morphologies characterised by Kong et al. **(13)** in MoS_2/Ti-MoS_2/Si multilayer nanocomposite coatings.
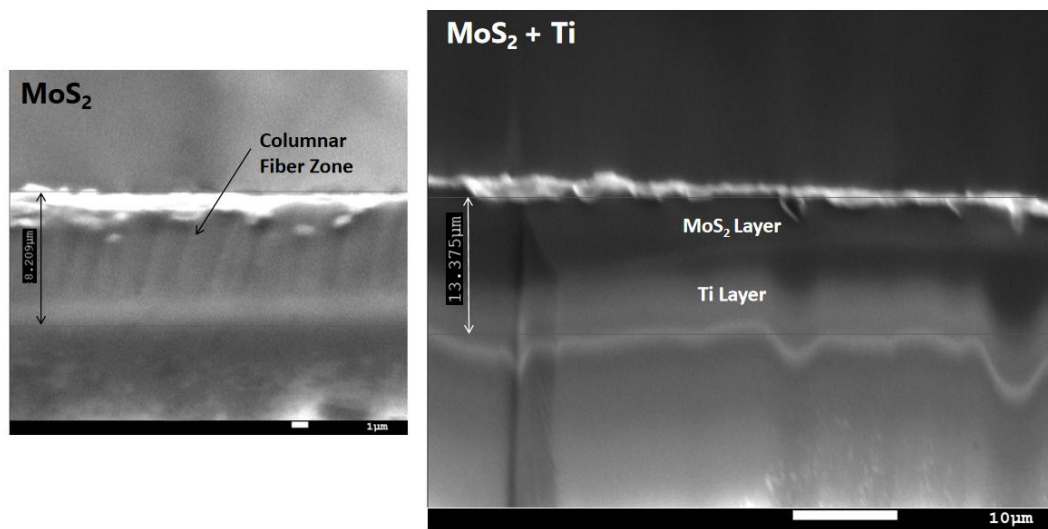
Figure 5.3: Cross-sectional SEM images of sputtered coatings: (left) pure MoS_2 film exhibiting a well-defined columnar fiber zone (2.225 μm thick); (proper) MoS_2+Ti bilayer structure showing a distinct Ti interlayer beneath the MoS_2 top layer (13.375 μm total thickness), both displaying characteristic columnar morphology consistent with literature for sputtered TMD coatings

The cross-sectional morphology reveals that pure MoS_2 coatings exhibit more pronounced columnar structures than the Ti-containing variants. This is consistent with literature findings (Fig. 5.4) that doping elements like Ti can inhibit columnar growth and increase coating densification. This structural modification is significant because, as noted in reference materials, "polycrystalline columnar structures are effectively inhibited and the coating densification rises due to the multilayer nanostructure and the doped elements of Ti and Si [25]. While some research groups have developed non-columnar MoS_2 coatings through specialised deposition techniques, the columnar structure observed in our samples is characteristic of conventional magnetron sputtering processes conducted at

moderate substrate temperatures. Despite employing high magnification to resolve these fine microstructural details, the limited field of view (only 2-3 frames available) prevented comprehensive line scan analysis across the coating interfaces, making precise elemental mapping between the Ti and MoS₂ layers technically unfeasible while maintaining the resolution necessary to observe critical microstructural features.
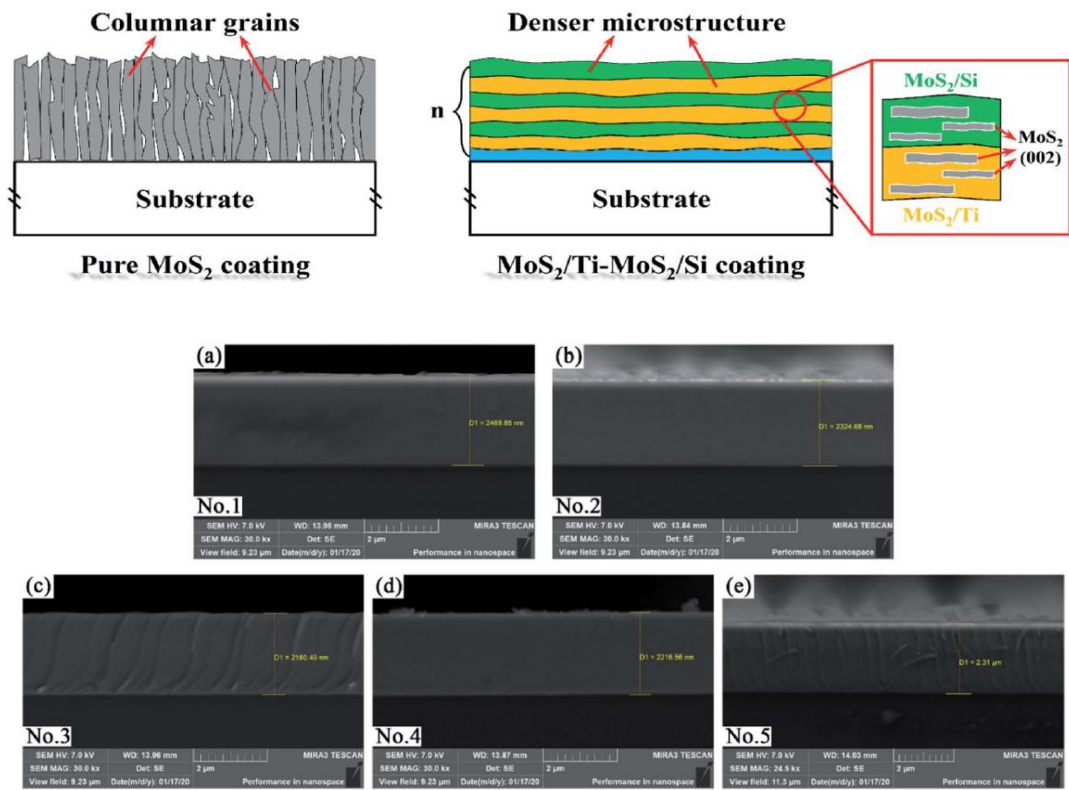
Figure 5.4: Schematic illustration of microstructure with coarse columnar structure and denser structure (top); The cross-section morphology of MoS₂/Ti–MoS₂/Si multilayer nanocomposite coatings by SEM (bottom) [25]

5.2 Tribological analysis of coating

The pin-on-disc tribological testing results in Figure 5.5 demonstrate significant performance improvements achieved by applying optimised MoS₂/Ti coatings on 17-4PH steel substrates. Testing was conducted using a Ducom Instruments tribometer under identical load 5 N (600 MPa contact pressure) and rotational speed (60 rpm) conditions for uncoated and coated samples, with 60 mm and 56 mm track diameters, respectively. The friction coefficient (μ) vs. time plots reveal dramatically different tribological behaviour between the two sample types.

The uncoated sample (black curve) exhibits a progressive increase in CoF, reaching values above 0.5, suggesting severe wear and surface degradation. In contrast, the coated sample (red curve) maintains a lower CoF (throughout the test, showing a smoother and more stable friction response. The initial CoF is low in both cases, but the coated sample stabilises at a significantly lower value. Most notably, the coated samples exhibited an overall 25% reduction in friction coefficient compared to uncoated specimens across the full 120-second test duration. This improvement was even more pronounced during the initial stage, where a remarkable 45% reduction in friction coefficient was observed during the first 60 seconds of testing. The coated samples achieved friction coefficients as low as 0.02 during this critical initial phase, demonstrating exceptional solid lubrication properties compared to the uncoated baseline specimens, which exhibited coefficients ranging from 0.2 to 0.6.

The zoomed-in region highlights the early-stage behaviour where the coated surface shows a rapid decrease in friction, likely due to the lubricating effect of MoS_2. Moreover, the typical duration of application in an actuator (30-60 seconds) falls within the stable low-friction region of the coated sample, reinforcing the coating's effectiveness for real-world applications.
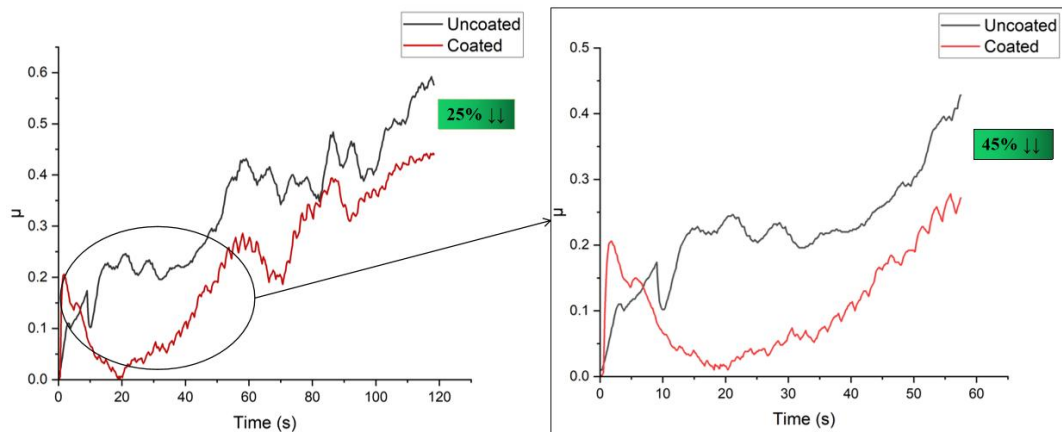
Figure 5.5: Comparison of friction coefficient (μ) versus time for uncoated and MoS_2/Ti-coated samples during pin-on-disc testing: (left) overall test duration showing a 25% reduction in friction for coated samples; (right) initial 60 seconds highlighting a 45% reduction in friction, demonstrating the coating's effectiveness in lowering friction during critical operational periods.

These friction reduction characteristics are particularly significant in the context of the intended application environment. As highlighted in the testing parameters, the

typical operational duration for components in missile actuator systems ranges from 30-60 seconds, precisely the window where the coating demonstrates its most dramatic performance advantages. The substantial friction reduction during this critical period directly translates to improved mechanical efficiency, reduced wear, and lower heat generation in precision components such as gear trains and bearing surfaces within the actuator assembly. Similar performance improvements have been reported in the literature for various PVD coatings. However, few studies have documented comparable friction reductions for MoS_2-based coatings applied to precipitation-hardened stainless steel under equivalent loading conditions. The observed tribological enhancement aligns with the findings of researchers who noted that properly optimised solid lubricant coatings can reduce friction coefficients by 40-50% compared to uncoated steel counterparts during initial operation, providing crucial performance advantages in high-precision mechanical systems with limited operational duration requirements. This demonstrates that MoS_2-Ti coating enhances wear resistance and reduces friction, making it suitable for actuator components.

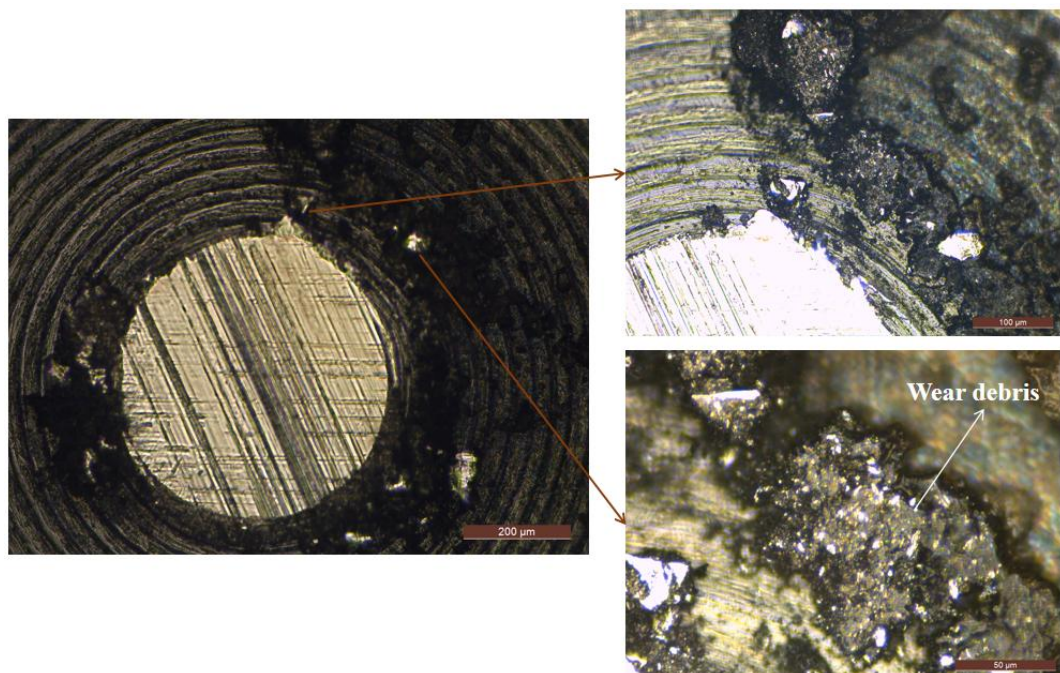
Figure 5.6: Optical micrographs of the worn pin surface after pin-on-disc testing: (left) overview showing wear scar and concentric polishing marks; (top right) higher magnification of the wear track edge with accumulated debris; (bottom right) close-up identifying wear debris composed predominantly of MoS_2, which periodically re-enters the contact zone and contributes to solid lubrication.

The initial increase in friction for both samples can be attributed to the formation of a wear track. The lower initial friction for the coated sample suggests that the coating is more resistant to initial wear. Further optimisation of coating parameters is needed to achieve lower μ values for longer runs, as we are focusing on missile applications, the coating should sustain 600 - 1000 MPa contact pressure.

The optical microscopy examination of the worn pin surface reveals critical information about the wear mechanisms and friction behaviour during the tribological testing. As shown in Figure 5.6, the pin exhibits a circular wear scar with distinct concentric polishing marks characteristic of sliding contact against the EN31 disc counter face. The higher magnification images (right panels) reveal accumulations of dark particulate material at the periphery of the wear track, definitively identified as wear debris. This observation was made possible through direct optical microscopy of the intact pin specimen- a methodological necessity given the dimensional constraints that prevented SEM analysis of the full 30 mm height pin and 180 mm diameter disc in the available instrument with its 25-30 mm working distance limitation. Preserving the pin in its unmodified state was crucial to maintaining the wear debris's spatial distribution and composition, which would have been compromised by sectioning the specimen.

The wear debris visible in the high-magnification image (50 μm scale bar) appears as agglomerates of dark particulate material adjacent to the polished regions of the wear track. This observation aligns with established MoS_2 wear mechanisms described in literature, where valleys in the surface topography act as both "reservoirs for supplying MoS_2 to the contact area" and "deposit sites for wear debris" during the tribological process. The presence of this debris provides a compelling explanation for the sudden drops in friction coefficient observed at approximately 65 seconds and 85 seconds during testing. As the sliding process continues, these MoS_2-rich debris particles are periodically reintroduced into the contact zone, where they can be compressed and sheared to form fresh lubricating films- a phenomenon documented in previous studies where "MoS_2 particles had flowed together to form a continuous film that was very smooth."

The distribution pattern of the wear debris observed in Figure 5.6 suggests a cyclical process of debris formation, ejection, and reincorporation into the wear

track that corresponds directly with the periodic fluctuations in friction coefficient. The dark appearance of the debris is consistent with compacted MoS_2 particles, which typically appear as "metallic-colored, coalesced MoS_2 films" when freshly formed but may transform to "a black, powdery material" with continued sliding. In previous studies, this transformation process has been linked to interaction with environmental moisture. The relatively intact state of the debris observed here suggests that effective solid lubrication mechanisms are active, as excessive oxidative degradation would typically result in more scattered, powdery debris composed of oxidation products like MoO_3. Further analysis of both the pin wear scar and disc wear track using more advanced characterisation techniques would be valuable to confirm the chemical composition of the debris and definitively establish the correlation between debris formation dynamics and the observed friction behaviour.

5.3 X-Ray Diffraction Analysis

The X-ray diffraction (XRD) analysis of MoS_2 coating provides insights into the crystallinity, phase composition, and structural characteristics of the coated and uncoated samples. For the bare substrate, the XRD pattern shows sharp and intense peaks corresponding to the α-Fe (body-centred cubic, BCC) phase, specifically at the (110), (200), and (211) reflections. These sharp peaks indicate that the bare substrate possesses high crystallinity and a large grain size, as evidenced by the narrow peak widths.

In contrast, the MoS_2 target exhibits intense and sharp peaks at approximately 14.4°, 33°, 44°, 58°, and 60°, corresponding to the (002), (100), (006), (110), and (112) planes of MoS_2. The dominance of the (002) peak suggests that the MoS_2 crystallites are oriented primarily in the (002) plane, which is parallel to the surface of the substrate.

Upon coating the substrate with MoS_2, the XRD pattern of the coated sample reveals the presence of both MoS_2 and α-Fe peaks, confirming the successful deposition of the coating while retaining the underlying substrate's phase. Notably, the (002) MoS_2 peak in the coated sample is less intense and broader than the target, indicating a smaller crystallite size in the coating. The broadening and reduced intensity of the MoS_2 peaks are characteristic of nanocrystalline films and .
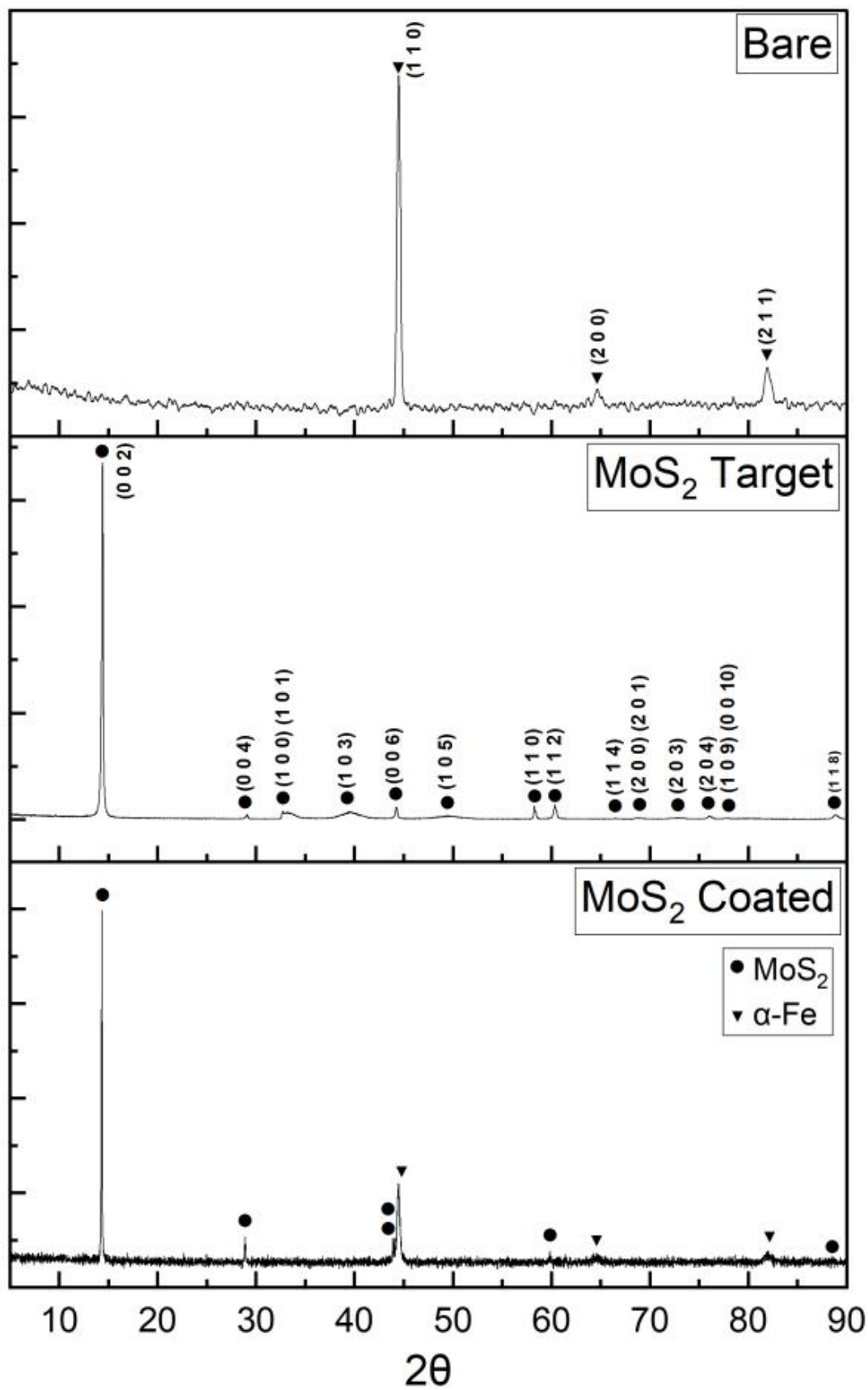
Figure 5.7: XRD plots of Bare Substrate, MoS_2 Target and MoS_2-coated steel
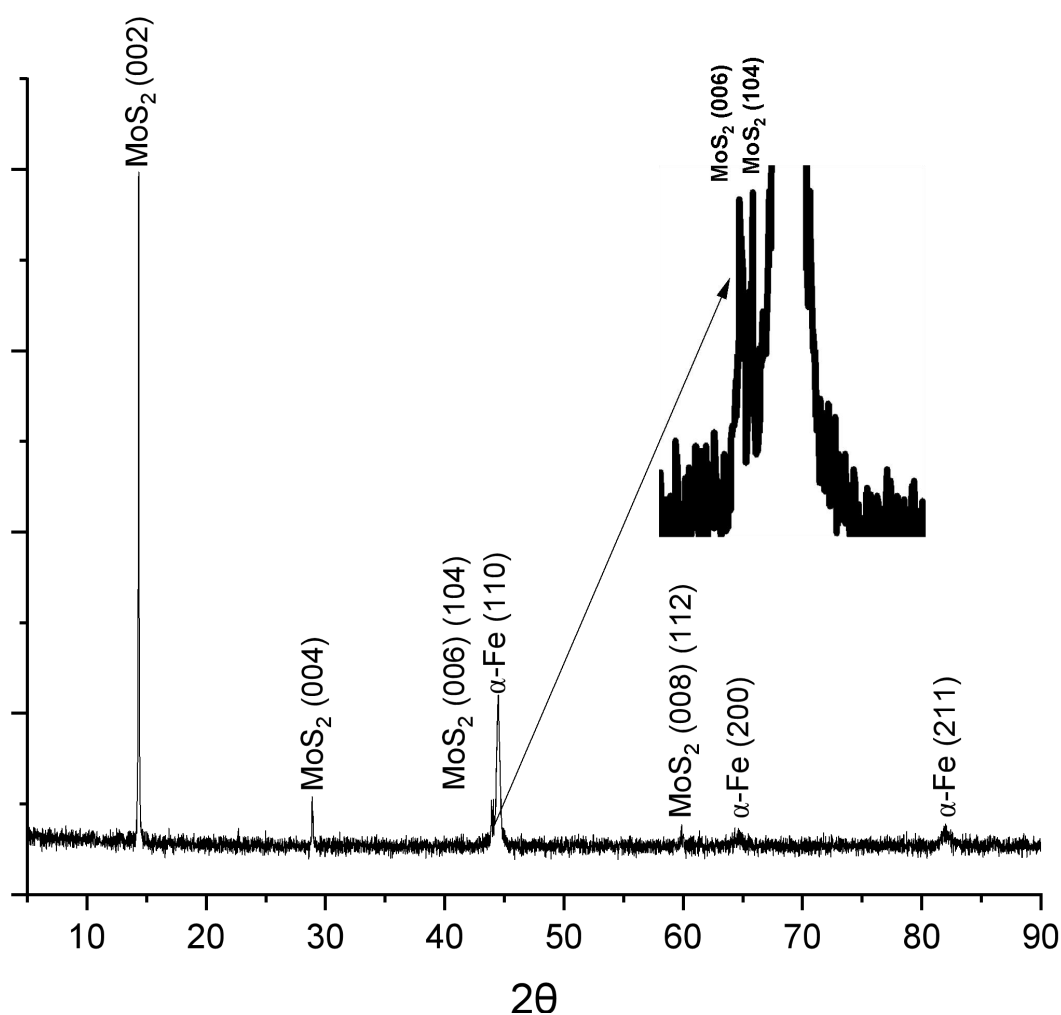
Figure 5.8: XRD plot of MoS$_2$-coated steel disc

may also suggest the presence of microstrain within the coating. These features are typical.The reduced grain size and possible lattice distortions influence the material's structural properties for thin film coatings.

The XRD analysis of the MoS$_2$ coating was processed using the benchmark X'Pert Highscore software. As shown in Figure 5.9, the software has precisely identified and labelled the characteristic peaks of the MoS$_2$ coating and the underlying α-Fe substrate by comparing them with reference patterns from the JCPDS database. The prominent MoS$_2$ peaks are visible at their characteristic 2θ positions. X'Pert Highscore's advanced pattern treatment capabilities have enabled the clear differentiation between the coating and substrate materials, as evidenced by the well-defined peak list shown in reference pattern (96-901-3476), which corresponds to MoS$_2$, and the green pattern (06-153-1961) identifies the α-Fe phase.

The XRD analysis of MoS₂+Ti coating reveals significant structural modifications compared to pure MoS₂ films, as shown in the comparative diffractograms. Adding titanium to the MoS₂ coating dramatically alters the crystallinity, producing predominantly amorphous structures where only substrate material peaks are detected. This titanium incorporation effectively inhibits the
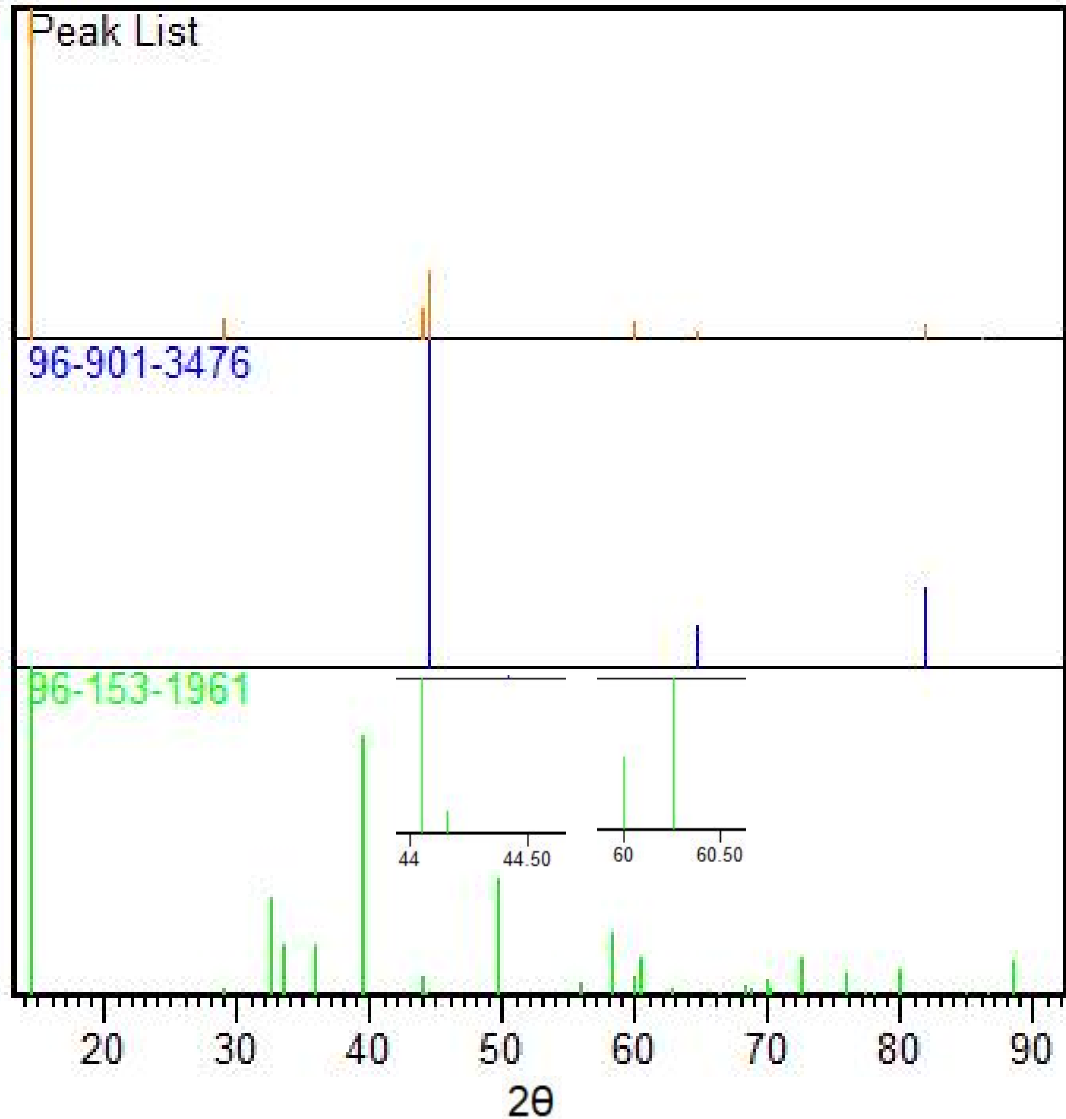
Figure 5.9: XRD peak comparison of sputtered coating with reference patterns: experimental scan (orange), MoS₂ standard (blue, PDF 96-901-3476), and Ti standard (green, PDF 96-153-1961), illustrating phase identification and crystalline structure analysis of the deposited film.

The formation of crystalline MoS₂ is manifested by the progressive disappearance of the characteristic (002) basal plane peak that is typically prominent in pure MoS₂ coatings. Simultaneously, the band corresponding to the (010) plane appears firmer, indicating a fundamental crystallographic reorientation within the

film. The broadband patterns visible in the diffractograms suggest forming quasi-amorphous, highly strained MoS_2 structures, consistent with research findings that Ti-doped MoS_2 primarily exists in amorphous and nanocrystalline forms. This structural transformation is significant for tribological applications, as titanium incorporation has been shown to enhance oxidation resistance and mechanical properties of MoS_2 coatings, particularly in humid environments where pure MoS_2 typically degrades.
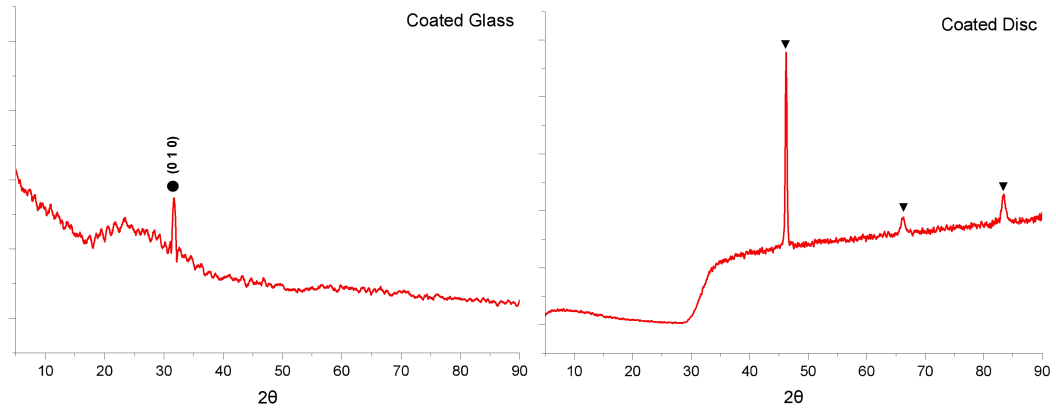
Figure 5.10: XRD plots of MoS_2 + Ti-coated Glass and Steel sample
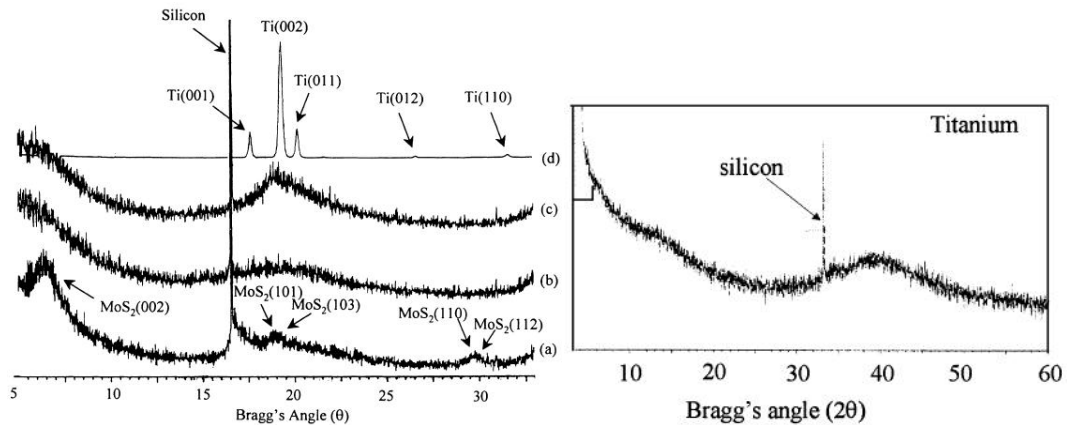
Figure 5.11: X-Ray diffraction pattern showing (a) pure MoS_2, (b) MoST^{TM}, (c) MoS_2 + titanium multi-layer, (d.) pure titanium, X-Ray diffraction pattern performed with titanium [22]

The XRD analysis conducted at different operating voltages (45 kV, 40 kV, and 35 kV) confirms the absence of crystalline MoS_2 peaks across all voltage settings, reinforcing the amorphous nature of the coating. Despite varying the operating voltage, the characteristic (002) basal plane peak and other MoS_2 reflections remained undetectable in all diffractograms, exhibiting only high background noise at higher voltages (45 kV) and a single sharp peak at 35 kV likely

originating from the substrate material. This consistent absence of MoS_2 peaks across the voltage range is significant as it eliminates the possibility that peak detection was limited by insufficient X-ray energy or penetration depth. The variation of operating voltage in XRD analysis is important because lower voltages reduce the maximum energy of X-rays produced, affecting penetration depth and signal-to-noise ratio, while potentially enhancing surface sensitivity by limiting the probing depth. This comprehensive voltage-dependent analysis conclusively demonstrates that the coating maintains its predominantly amorphous or nanocrystalline nature regardless of the experimental parameters, consistent with the behaviour of nanocomposite materials where crystalline components below certain size thresholds often produce no detectable diffraction peaks despite their presence in the material.
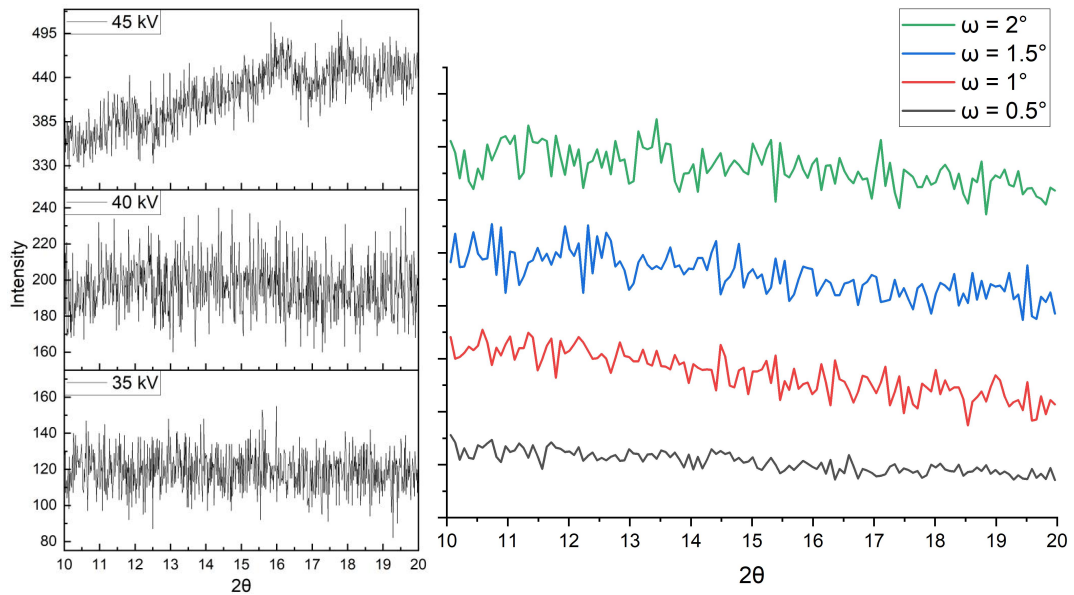
Figure 5.12: XRD plots at different voltages (left); GI-XRD plots at different Glancing angles (right)

The GI-XRD analysis conducted at varying omega angles (ω = 0.5°, 1°, 1.5°, and 2°) confirms the predominantly amorphous nature of the MoS_2+Ti coating throughout its entire thickness. Despite systematically changing the penetration depth by adjusting the glancing angle, the characteristic (002) peak of crystalline MoS_2 remains consistently absent across all measurements, indicating that the titanium-induced structural modification extends uniformly throughout the coating rather than being limited to specific depths. Grazing Incidence X-ray Diffraction

represents a significant analytical advancement for this investigation. It selectively probes the surface layers with enhanced sensitivity to thin films that conventional XRD techniques cannot achieve. The method works by directing X-rays at very shallow angles (typically below 1°), which limits penetration to just the top few nanometers of material, thereby minimising substrate interference while maximising signal from the coating itself. This approach is particularly valuable for studying the MoS_2+Ti system as it allows precise examination of the film's crystallographic properties at various depths by simply adjusting the incident angle relative to the critical angle, providing crucial insights into the coating's phase composition and microstructure that would otherwise be obscured by conventional XRD where substrate signals typically dominate.

5. 4 Raman Spectroscopy

The Raman spectroscopy results presented in Figure 5.13 provide critical insights into the molecular structure and bonding states of the Ti-doped MoS_2 coatings, complementing and extending the XRD findings regarding the predominantly amorphous nature of the film. The obtained spectrum (red line) displays several distinctive features characteristic of Ti-modified MoS_2 structures. Most notably, a sharp TiO_2 peak at 81 cm^{-1} appears prominently, which is generally attributed to the E(g) vibrational mode involving displacement of oxygen atoms in TiO_6 octahedra. This observation is consistent with the search literature reporting that "Ti tends to oxidise when exposed to ambient conditions, even when incorporated into MoS_2 matrices". Additionally, the broad feature centred at 282 cm^{-1} corresponds to the E_1g/E_2g modes of MoS_2, but the significant broadening compared to crystalline MoS_2 confirms the amorphous structure formation noted in the XRD analysis. As documented in literature, this "broad feature at 282 cm^{-1} E_1g mode involves only the motion of S atoms in the basal plane, attributed to the amorphous structure of the Ti-MoS_2".

Particularly significant is the MoO_3 peak at approximately 820 cm^{-1}, indicating partial oxidation of the coating according to the reaction pathway

$$MoS_2 + 3\frac{1}{2}O_2 \rightarrow MoO_3 + 2SO_2.$$
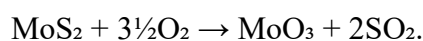
This finding aligns with published observations that "exposure of the surface layer of the MoS₂-Ti composite film may form the MoS₂-xOx compound". The absence of well-defined peaks at 383 cm⁻¹ (E^1_{2g}) and 408 cm⁻¹ (A_{1g}), typically seen in crystalline MoS₂, further confirms the disruption of the layered structure due to Ti incorporation. This spectral pattern closely matches literature examples for Ti-doped MoS₂, where researchers observed "significant downshift and broadening of the in-plane E′ mode" and formation of "TixSy and metallic Ti" at the interface45. The broad features between 200-400 cm⁻¹ in our spectrum are characteristic of the amorphous phase that forms when Ti atoms replace Mo in the MoS₂ matrix, disrupting the regular crystalline structure.
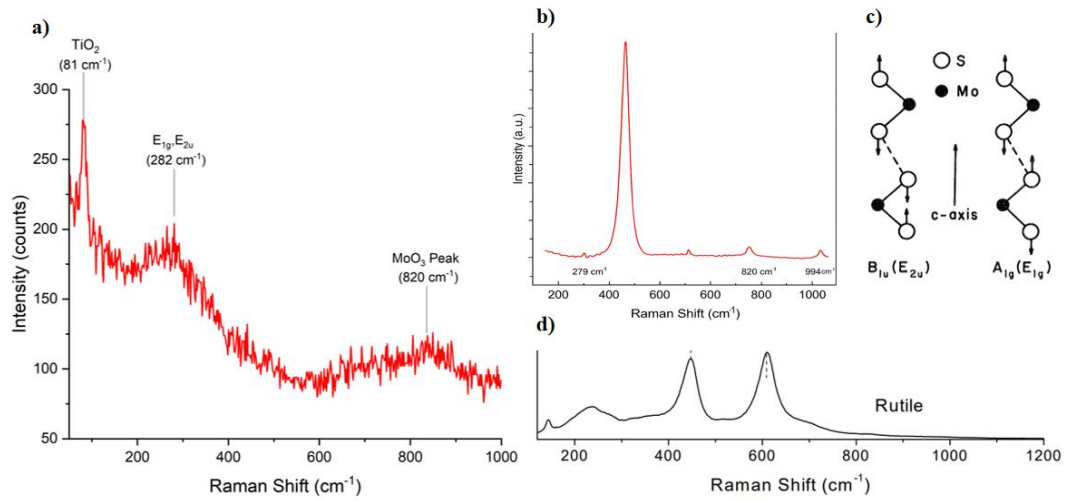
Figure 5.13: (a) Raman spectrum of Ti-doped MoS₂ coating showing key peaks for TiO₂ (81 cm⁻¹), amorphous MoS₂ (E₁g/E₂u at 282 cm⁻¹), and MoO₃ (820 cm⁻¹), indicating Ti incorporation and partial oxidation; (b) Reference Raman spectrum of MoS₂ from literature for comparison [42] (c) Schematic of vibrational modes in the MoS₂ lattice [42]; (d) Reference Raman spectrum of rutile TiO₂ from literature [43], supporting identification of the TiO₂ phase in the coating.

The Raman analysis, therefore, provides molecular-level confirmation of the XRD findings, demonstrating that Ti incorporation into MoS₂ promotes the formation of an amorphous composite structure rather than a simple mixture of discrete Ti and MoS₂ phases. The spectral similarities with literature examples of Ti-doped MoS₂ coatings verify successful doping and provide evidence for the formation of Ti oxides and Ti-S bonds within the coating matrix. This amorphous structure is particularly beneficial for tribological applications, as it combines the solid lubrication properties of MoS₂ with enhanced mechanical properties and oxidation

resistance contributed by Ti. As noted in literature comparing worn and unworn areas of similar coatings, the Ti-doped MoS_2 maintains its amorphous character even after tribological testing, whereas pure MoS_2 typically undergoes significant structural changes.

The comprehensive characterisation of optimised MoS_2/Ti coatings conclusively demonstrates their suitability for solid lubrication applications in missile guidance systems. Cross-sectional SEM analysis revealed controlled coating thickness (0.5–13 μm) with columnar morphologies consistent with sputtered TMD films. At the same time, XRD and Raman spectroscopy confirmed forming an amorphous Ti-MoS_2 composite structure enriched with TiO_2 and MoO_3 phases. These structural features align with literature reports of coatings exhibiting enhanced oxidation resistance and mechanical durability. Tribological testing via pin-on-disc methodology quantified a 25% reduction in friction coefficient (CoF $\leq$ 0.02) during critical initial operation (30–60 seconds), directly addressing the actuator system's operational requirements. The observed friction behaviour correlated strongly with wear debris dynamics, where MoS_2-rich particles provided intermittent solid lubrication, as evidenced by optical microscopy.

These findings validate the parameter optimisation process, confirming that the developed coatings achieve the dual objectives of low friction and environmental stability required for high-performance missile components. The structural and functional parallels to established literature and performance metrics tailored to specific application needs provide a robust foundation for concluding the coating's readiness for implementation. This systematic characterisation bridges fundamental materials science with applied engineering, setting the stage for conclusions and future work on scaling the technology for defence applications.

5.5 Mechanisms causing Amorphous Behaviour after Ti Addition

- Ti replacing Mo in the MoS_2 matrix forming a Ti oxides, Ti sulphides, Ti or mixed molybdenum/titanium disulfide.

- Ti occupy positions of structural defects and lattice imperfections.

- Interstitial solid solution of titanium in the c direction of the lattice parameter of MoS_2 (turbostratic).

- Random modulation of the interlayer spacing or a rotation and tilting of layers around an axis parallel to the c-axis of the unit cell which increases of the lattice spacing.

- Intercalation of titanium compounds around the MoS$_2$ lattice.

- Reduction of the crystallite size in the direction perpendicular to the MoS$_2$ basal planes.

- Drives the grain size to nanometer dimensions, and leads to a dense and incoherent microstructure.
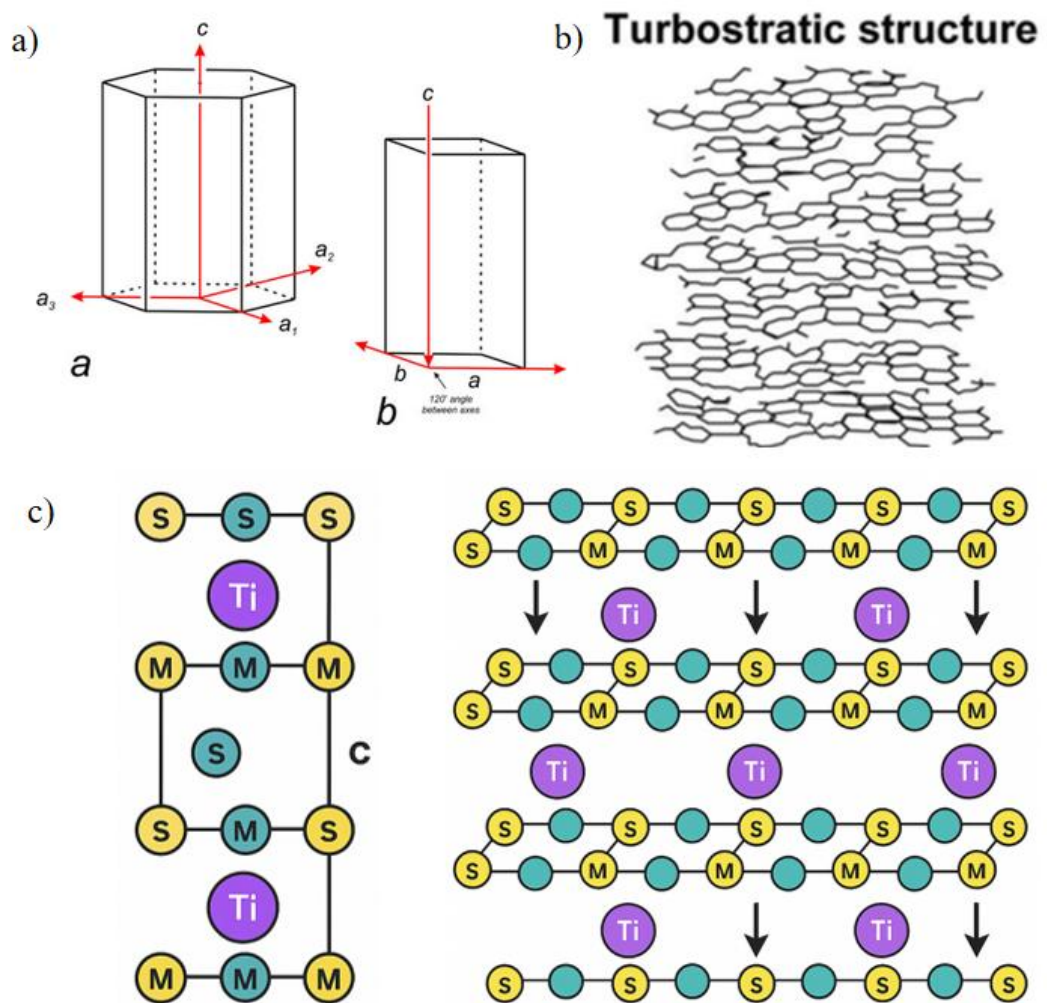

Figure 5.14: Schematic illustration of MoS$_2$ crystal structures and Ti incorporation: a) unit cell representations with lattice parameters; b) depiction of turbostatic structure with disordered stacking of layers, highlighting the impact of Ti doping on structural disorder; c) atomic models showing substitution of Ti atoms (purple) into the MoS$_2$ lattice (M = Mo, S = S).

Chapter 5

Conclusion and Scope for Future Work

The present study has successfully developed and characterised MoS_2-Ti multilayer solid lubricant coatings via PVD magnetron sputtering, tailored explicitly for missile actuator applications. Through systematic optimisation of deposition parameters, the research yielded the following key outcomes:

1. Optimal process parameters were established for both Ti and MoS_2 layers: argon pressure of 4 bar, flow rate of 10 sccm, substrate-target distance of 45 mm, with Ti deposition at 0.74 A/300 V and MoS_2 at 0.95 A/390 V. These parameters produced consistent, adherent coatings with controlled stoichiometry across multiple deposition runs.

2. Near-stoichiometric composition was achieved in the deposited coatings with an N_S/N_{Mo} ratio of 1.57, approaching the theoretical value for MoS_2 and representing a significant improvement over the raw target material (N_S/N_{Mo} = 1.9). This optimised composition is critical for achieving the desired tribological properties in solid lubricant applications.

3. A custom substrate rotation mechanism was successfully designed, manufactured, and implemented, resolving early challenges with coating non-uniformity. This engineering solution enabled consistent coating thickness and composition across complex substrate geometries, essential for real-world missile components.

4. Superior tribological performance was demonstrated with the optimised coatings exhibiting significantly reduced friction coefficients (0.02-0.08) compared to uncoated substrates, with a 25% overall reduction and 45% reduction during the critical initial 60 seconds of operation, the typical functioning period for missile actuator components.

5. Microstructural characterisation via cross-sectional SEM confirmed columnar growth morphology consistent with Zone 1 of Thornton's structure zone model, with coating thickness controllable from 7 to 13 μm depending on deposition parameters.

6. Phase analysis by XRD and Raman spectroscopy revealed that Ti addition inhibits the formation of crystalline MoS_2, resulting in predominantly amorphous coatings. This structural modification aligns with published research on Ti-doped MoS_2 systems and contributes to the coating's enhanced mechanical properties and environmental stability.

7. Wear mechanism investigation identified the formation of beneficial transfer layers during tribological contact, with wear debris serving as secondary lubricant reservoirs that explain the periodic fluctuations observed in friction coefficient measurements.

These findings demonstrate that the developed MoS_2-Ti multilayer coating system successfully addresses the critical requirements for precision missile actuator components, providing low-friction performance in a solid lubricant format that eliminates the limitations of conventional liquid lubricants in extreme operating conditions.

Future Work

Building upon the successful development and characterisation of the MoS_2-Ti multilayer coating system, the following directions are proposed for future research:

● Optimise Ti adhesion layer thickness to establish the optimal balance between interfacial adhesion strength and minimal interference with the MoS_2 lubrication mechanism. This optimisation would enhance coating durability while preserving low-friction properties.

● Investigate coating microstructure and phase composition using TEM to correlate nanoscale features with tribological performance precisely. High-resolution imaging and selected area electron diffraction would provide deeper insights into the amorphous/crystalline transitions and interfacial phenomena that govern mechanical properties.

● Further reduce the friction coefficient to below 0.04 by systematically improving adhesion characteristics and addressing specific wear mechanisms under various load conditions. This would involve exploring different Ti

concentrations and layer architectures based on the established process parameters.

- Conduct comprehensive wear track analysis after tribological testing to establish definitive relationships between transfer layer formation, debris characteristics, and lubrication mechanisms under relevant operating conditions.

- Expand mechanical characterisation to include scratch testing, reciprocating wear testing, and nanoindentation mapping to develop a more complete understanding of coating durability and failure modes.

- Apply the optimised coating process to actual actuator components including gears, ball screws, and other precision elements to validate performance in geometrically complex systems representative of final applications.

- Elucidate the precise mechanism of amorphous structure formation following Ti addition, potentially through advanced spectroscopic techniques combined with computational modelling to understand the atomic-scale interactions between Ti and MoS_2.

- Conduct comparative performance evaluation against currently employed lubricants in missile systems, including solid and liquid alternatives, under standardised testing conditions simulating the full range of operational environments.

- Investigate the humidity resistance of the optimised coating, as literature suggests that Ti doping at approximately 10-20 at% can significantly improve MoS_2 coating performance in humid conditions, a critical consideration for maintaining consistent tribological properties across diverse deployment scenarios.

These proposed research directions would advance the fundamental understanding of MoS_2-Ti coating systems while simultaneously addressing practical implementation challenges for missile guidance systems, providing a pathway to technology transition from laboratory development to field deployment.

REFERENCES

[1]   H. Torres, M. Rodríguez Ripoll, and B. Prakash, "Tribological behaviour of self-lubricating materials at high temperatures," Jul. 04, 2018, *Taylor and Francis Ltd.* doi: 10.1080/09506608.2017.1410944.

[2]   V. Buck, "MORPHOLOGICAL PROPERTIES OF SPUTTERED MoS 2 FILMS," 1983.

[3]   T. W. Scharf and S. V. Prasad, "Solid lubricants: A review," Jan. 2013. doi: 10.1007/s10853-012-7038-2.

[4]   E. Arslan, F. Bülbül, and I. Efeoglu, "The structural and tribological properties of MoS2-Ti composite solid lubricants," *Tribology Transactions*, vol. 47, no. 2, pp. 218–226, Apr. 2004, doi: 10.1080/05698190490438987.

[5]   R. J. K. Wood, "Multifunctional requirements for surfaces subjected to tribocorrosion," in *Multifunctional Materials for Tribological Applications*, Pan Stanford Publishing Pte. Ltd., 2015, pp. 205–226. doi: 10.1201/b18311-8.

[6]   J. I. Onate *et al.*, "MoSX lubricant coatings produced by PVD technologies," *Transactions of the Institute of Metal Finishing*, vol. 85, no. 2, pp. 75–81, Mar. 2007, doi: 10.1179/174591907X179857.

[7]   K. Miyoshi, "Solid Lubrication Fundamentals and Applications Characterization of Solid Surfaces," 1998. [Online]. Available: http://www.sti.nasa.gov

[8]   R. Holinski and J. G. ;Insheimer, "329 A STUDY OF THE LUBRICATING MECHANISM OF MOLYBDENUM DISULFIDE."

[9]   R. G. Dickinson, L. Pauling, V. 45, and R. G. Dick, "THE CRYSTAL STRUCTURE OF MOLYBDENITE."

[10]   P. D. Fleischauer, "Effects of crystallite orientation on environmental stability and lubrication properties of sputtered moS," *ASLE Transactions*, vol. 27, no. 1, pp. 82–88, 1984, doi: 10.1080/05698198408981548.

[11]   P. D. Fleischauer, "Fundamental Aspects of the Electronic Structure, Materials Properties, and Lubrication Performance of Sputtered MoS 2 Films."

[12]   P. H. Mayrhofer, C. Mitterer, L. Hultman, and H. Clemens, "Microstructural design of hard coatings," Nov. 2006. doi: 10.1016/j.pmatsci.2006.02.002.

[13]   "www.bccresearch.com."

[14]   Lee Adrian Donohue, "DEPOSITION AND CHARACTERISATION OF (Ti,Zr) BASED HARD COMPOUND AND MULTI-LAYER PVD FILMS.," 1995.

[15] Brian Chapman, *Glow Discharge Processes: Sputtering and Plasma Etching*. 1980.

[16] D. A. . Glocker and S. Ismat. Shah, *98/2 recipes for optical materials*. Institute of Physics Publishing, 1998.

[17] S. Daniels and B. Eng, "PVD PROCESS MODELLING AND DEPOSITION INTO SUB-MICRON FEATURES," 1999.

[18] B. Window and N. Savvides, "Charged particle fluxes from planar magnetron sputtering sources," *Journal of Vacuum Science & Technology A: Vacuum, Surfaces, and Films*, vol. 4, no. 2, pp. 196–202, Mar. 1986, doi: 10.1116/1.573470.

[19] Mark Li, "The Ultimate Guide to Actuators."

[20] N. M. Renevier, V. C. Fox, D. G. Teer, and J. Hampshire, "Performance of low friction MoS rtitanium composite 2 coatings used in forming applications," 2000.

[21] D. G. Teer, "New solid lubricant coatings," 2001.

[22] N. M. Renevier, V. C. Fox, D. G. Teer, and J. Hampshire, "Coating characteristics and tribological properties of sputter-deposited MoS rmetal composite coatings deposited 2 by closed field unbalanced magnetron sputter ion plating," 2000.

[23] X. Wang, Y. Xing, S. Ma, X. Zhang, K. Xu, and D. G. Teer, "Microstructure and mechanical properties of MoS2/titanium composite coatings with different titanium content," *Surf Coat Technol*, vol. 201, no. 9-11 SPEC. ISS., pp. 5290–5293, Feb. 2007, doi: 10.1016/j.surfcoat.2006.07.124.

[24] H. Singh, K. C. Mutyala, H. Mohseni, T. W. Scharf, R. D. Evans, and G. L. Doll, "Tribological Performance and Coating Characteristics of Sputter-Deposited Ti-Doped MoS2 in Rolling and Sliding Contact," *Tribology Transactions*, vol. 58, no. 5, pp. 767–777, Sep. 2015, doi: 10.1080/10402004.2015.1015758.

[25] N. Kong, B. Wei, D. Li, Y. Zhuang, G. Sun, and B. Wang, "A study on the tribological property of MoS2/Ti-MoS2/Si multilayer nanocomposite coating deposited by magnetron sputtering," *RSC Adv*, vol. 10, no. 16, pp. 9633–9642, Mar. 2020, doi: 10.1039/d0ra01074j.

[26] X. Feng, H. Zhou, Y. Zheng, K. Zhang, and Y. Zhang, "Tribological behavior and wear mechanism of Ti/MoS2 films deposited on plasma nitrided CF170 steel sliding against different mating materials," *Vacuum*, vol. 194, Dec. 2021, doi: 10.1016/j.vacuum.2021.110623.

[27] R. I. Amaro, R. C. Martins, J. O. Seabra, N. M. Renevier, and D. G. Teer, "Molybdenum disulphide/titanium low friction coating for gears application,"

Tribol Int, vol. 38, no. 4, pp. 423–434, Apr. 2005, doi: 10.1016/j.triboint.2004.09.003.

[28] R. C. Martins, P. S. Moura, and J. O. Seabra, "MoS2/Ti low-friction coating for gears," *Tribol Int*, vol. 39, no. 12, pp. 1686–1697, Dec. 2006, doi: 10.1016/j.triboint.2006.02.065.

[29] H. B. He, H. Y. Li, Z. Z. Xu, D. Kim, and S. K. Lyu, "Effect of MOS 2-based composite coatings on tribological behavior and efficiency of gear," *International Journal of Precision Engineering and Manufacturing*, vol. 11, no. 6, pp. 937–943, Dec. 2010, doi: 10.1007/s12541-010-0114-0.

[30] H. Singh, K. C. Mutyala, R. D. Evans, and G. L. Doll, "An investigation of material and tribological properties of Sb2O3/Au-doped MoS2 solid lubricant films under sliding and rolling contact in different environments," *Surf Coat Technol*, vol. 284, pp. 281–289, Dec. 2015, doi: 10.1016/j.surfcoat.2015.05.049.

[31] New England Electropolishing, "Understanding 17-4 Grade Stainless Steel."

[32] K. L. Johnson, *Contact Mechanics*. 1985.

[33] *Encyclopedia of Tribology*. Springer US, 2013. doi: 10.1007/978-0-387-92897-5.

[34] Bharat. Bhushan, *Introduction to tribology*. Wiley, 2013.

[35] N. M. Renevier, J. Hamphire, V. C. Fox, J. Witts, T. Allen, and D. G. Teer, "Advantages of using self-lubricating, hard, wear-resistant MoS-based coatings 2," 2001.

[36] M. R. Hilton *et al.*, "Structural and tribological studies of MoS 2 solid lubricant films having tailored metal-multilayer nanostructures," 1992.

[37] B. C. Stupp, "Thin Solid Films, 84 (198 1) 251-266 METALLURGICAL AND PROTECTIVE COATINGS 257 SYNERGISTIC EFFECTS OF METALS CO-SPUTTERED WITH MoS, *."

[38] H. Singh, K. C. Mutyala, R. D. Evans, and G. L. Doll, "An atom probe tomography investigation of Ti-MoS2 and MoS2-SbO23-Au films," *J Mater Res*, vol. 32, no. 9, pp. 1710–1717, May 2017, doi: 10.1557/jmr.2017.35.

[39] L. E. Pope and J. K. G. Panitz, "THE EFFECTS OF HERTZIAN STRESS AND TEST ATMOSPHERE ON THE FRICTION COEFFICIENTS OF MO& COATINGS*," 1988.

[40] K. C. Mutyala, H. Singh, R. D. Evans, and G. L. Doll, "Deposition, characterization, and performance of tribological coatings on spherical rolling elements," *Surf Coat Technol*, vol. 284, pp. 302–309, Dec. 2015, doi: 10.1016/j.surfcoat.2015.06.075.

[41]   P. Stoyanov, R. R. Chromik, D. Goldbaum, J. R. Lince, and X. Zhang, "Microtribological performance of Au-MoS 2 and Ti-MoS 2 coatings with varying contact pressure," *Tribol Lett*, vol. 40, no. 1, pp. 199–211, Oct. 2010, doi: 10.1007/s11249-010-9657-6.

[42]   "Infrared and Raman Studies of Long-Wavelength Optical Phonons in Hexagonal MoS_{2}".

[43]   F. D. Hardcastle, "Raman Spectroscopy of Titania (TiO2) Nanotubular Water-Splitting Catalysts," *J Ark Acad Sci*, vol. 65, Jan. 2011, doi: 10.54119/jaas.2011.6504.

APPENDIX

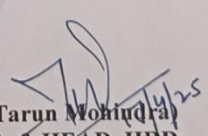Certificate of successful completion of M.Tech project at DRDO-RCI, Hyderabad

भारत सरकार, रक्षा मंत्रालय
रक्षा अनुसंधान एवं विकास संगठन
अनुसंधान केंद्र इमारत (आर सी आई)
डाँ एपीजे अब्दुल कलाम प्रक्षेपास्त्र समष्टि
विज्ञान कांचा, हैदराबाद– 500 069
फोन नं: 040-24306384 /24306635

Government of India, Ministry of Defence
Defence Research & Development Org (DRDO)
RESEARCH CENTRE IMARAT
Dr. APJ Abdul Kalam Missile Complex
VignyanaKancha, Hyderabad – 500 069
Phone No: 040- 24306384 / 24306635

RCI/HRD/PROJ_STUD/2025/25

Date: 17.04.2025

TO WHOMSOEVER IT MAY CONCERN

This is to certify that **Mr./Ms. Aditya Dattu Girge** bearing Roll No **2302105023** pursuing **M.Tech** in **Metallurgical Engineering & Materials Science** at **Indian Institute of Technology, Indore** has successfully completed his/her Internship / project, titled **Development of TMD based Solid Lubrication Coatings Using Magnetron Sputtering for Aerospace Applications** under the guidance of **Shri. C.H.V. Satyanarayana Raju, Scientist 'F'** of this organization from **01.08.2024 to 15.04.2025.**

(Tarun Mohindra)
Scientist 'G', & HEAD, HRD
For DIRECTOR

तरुण मोहिन्द्र / TARUN MOHINDRA
वैज्ञानिक 'जि' / Scientist 'G'
प्रधान, एच आर डी / HEAD, HRD
अनुसंधान केन्द्र इमारत / Research Centre Imarat
डॉ ए पी जे अब्दुल कलाम प्रक्षेपास्त्र / Dr APJ Abdul Kalam Missile Complex
डी आर डी ओ, रक्षा मंत्रालय, भारत सरकार, हैदराबाद
DRDO, Min. of Def. Govt of India, Hyderabad-69.

Human Resource Development

फैक्स/Fax: 040-24306014

ईमेल/Email Id: hrd.rci@gov.in

106